Optical Performance Monitoring in Digital Coherent Receivers

(ディジタルコヒーレント受信器を用いた光パフォーマンスモニタリング)

by

Md. Saifuddin FARUK
(モハマド サイフディン ファルク)
Student number: 37-087287

A Dissertation Submitted in Partial Fulfillment
of the Requirements for the Degree of
DOCTOR OF PHILOSOPHY

Supervised by
Professor Kazuro KIKUCHI
Department of Electrical Engineering and Information Systems,
THE UNIVERSITY OF TOKYO

01 June 2011

Abstract

Optical performance monitoring (OPM) is an important issue for proper operation of next-generation optical networks. Among various monitored parameters, the optical signal-to-noise ratio (OSNR) and fiber transmission impairments such as chromatic dispersion (CD), polarization mode dispersion (PMD), and polarization dependent loss (PDL) are paid special attention, because they serve information of the channel quality, which helps to manage the network. Several methods have been proposed for monitoring tasks, which are based on pilot tones, RF tones, asynchronous histogram, and fiber nonlinear effects. Most of them need costly devices, tap optical power from the channel, and introduce transmission overhead. On the other hand, in this research, we investigate OPM based on digital coherent receivers, which overcomes such difficulties and ensures cost-efficient, robust and reliable monitoring.

Linear channel impairments such as CD, PMD, and PDL are monitored from the transfer functions of adaptive filters. A digital coherent receiver allows polarization demultiplexing and equalization of all these impairments by using four finite-impulse-response (FIR) filters structured in a two-by-two butterfly configuration. After the filters are adapted by a suitable algorithm, we can construct a frequency-dependent two-by-two matrix with four elements, which are transfer functions of the adapted four FIR filters. The inverse of this matrix is called the monitoring matrix and can be approximated as the transfer matrix of the channel, and contains combined effects of CD, PMD and PDL. A precise algorithm is required to separate out the impairments from this matrix. We propose a simple and unified algorithm to separate out CD, differential group delay (DGD), PDL, and second-order PMD from the monitoring matrix. The components of second-order PMD, polarization-dependent chromatic dispersion (PCD) and depolarization (DEP) of principal states of polarization are obtained separately. This algorithm has an advantage that individual impairment can be estimated directly from the monitoring matrix without any matrix decomposition; thus it enables accurate estimation of the impairments, even when the transmitted signal suffers from distortion stemming from various origins. Also, no additional hardware is required for our proposed algorithm.

For filter adaptation, we use the constant-modulus algorithm (CMA), as it enables long-tap-filter adaptation efficiently even in the presence of large laser phase noise unlike the commonly used decision-directed least-mean-square (DD-LMS) algorithm. However, CMA can suffer from

the singularity problem which means both the output ports of butterfly configuration converge to the same polarization tributary. Consequently, we avoid the singularity problem by introducing the training mode in CMA. In the training mode, the LMS algorithm is used to determine in which output port of the butterfly configuration each polarization tributary appears, and after such initial training the algorithm is switched to the blind CMA to enable high-order-filter adaptation. The multi-impairment monitoring algorithm and the singularity-free operation of CMA with the training mode, which we have proposed in this thesis, are verified by dual-polarization quadrature phase-shift keying (QPSK) transmission experiments.

For such an impairment-monitoring method, the delay tap length of filters should be long enough to compensate for all the impairments. However, the computational complexity of FIR filters increases with the number of taps. The frequency-domain approach can reduce this computational cost by block-by-block processing and fast implementation of discrete Fourier transform (DFT). However, the adaptive frequency-domain equalizer (FDE) has hardly been investigated for optical communication systems. We have proposed a novel adaptive FDE based on CMA, which maintains all the advantages of the adaptive TDE based on FIR filters. Even in the block processing mode of FDE, it can work on the twofold-oversampled input sequence by introducing even and odd sub-equalizers. Therefore, when we configure this filter in the butterfly structure, we can achieve adaptive equalization together with polarization demultiplexing and adjustment of the arbitrary initial sampling phase of analog-to-digital converters (ADCs) so that the best symbol-spaced sequence is produced. The equalization performance of the proposed adaptive FDE as well as multi-impairment monitoring from the equalizer is verified by dual-polarization QPSK transmission experiments.

We have proposed a novel OSNR monitoring method. This is based on the analysis of higher-order statistical moments of adaptive-equalizer output in digital coherent receivers. After equalization and clock recovery by an adaptive equalizer, symbol-spaced signal samples and noise samples have well-defined but dissimilar statistical properties. In our proposed algorithm, we measure the second- and fourth-order moments of the adaptive-equalizer output. Then, by using the known statistics of the phase-modulated signal in the QPSK format and amplified spontaneous emission (ASE) noise, we estimate the OSNR. The proposed method is simple and accurate. We also experimentally verify this monitoring algorithm with 10-Gsymbol/s QPSK transmission experiments.

内容概観

光パフォーマンスモニタリングは次世代光ネットワークを構築するための重要な技術である．適切にネットワークを運用するためには，受信信号の光信号対雑音比(OSNR) や伝送路の波長分散(CD)，偏波モード分散(PMD)，偏波依存損失(PDL)などを観測する必要がある．これまで，パイロットトーン，RF トーン，非同期ヒストグラム，ファイバ非線形効果などに基づく観測手法が提案されている．しかし，これらの多くは高価で煩雑なシステムとなってしまうという欠点があった．一方，我々はディジタルコヒーレント受信器を用いたモニタリング技術を提案し，低コストかつ信頼できるモニタリングを可能とした．

CD，PMD，そして PDL のような線形な伝送路障害は適応フィルタの伝達関数から求めることができる．ディジタルコヒーレント受信器では，検波後にバタフライ構成の FIR フィルタを用いることで，偏波多重分離及び等化が可能である．フィルタを適切なアルゴリズムにより適応させることで，FIR フィルタの伝達関数を示す周波数依存の 2×2 の行列を構築できる．この逆伝達関数はモニタリング行列と呼ばれ，これから CD, PMD，PDL の情報を含む伝送路の伝達関数を推定することができる．我々は CD，DGD，PDL，そして 2 次 PMD を分離する簡易なアルゴリズムを提案した．2 次 PMD の構成要素である偏波依存波長分散および主偏波状態の偏波解消を独立に得ることができる．このアルゴリズムは行列分解することなくモニタリング行列から個別の伝送路障害を求めることができる．様々な伝送路障害が同時に存在していようとも，正しい推定を簡易なアルゴリズムで行うことができる．

フィルタの適応アルゴリズムとして，我々は CMA を用いた．これは DD-LMS アルゴリズムと比較して，位相雑音が存在しても安定に動作するためである．しかし，CMA はバタフライ構成の出力が同じ偏波に収束するという特異点問題を持つ．したがって，我々は CMA にトレーニングモードを導入することによってこの特異点問題を解決した．トレーニングモードでは，LMS アルゴリズムを用いることで各偏波チャネルがどのポートから出力されるかを決定する．その後，位相無依存であるブラインド

CMA に切り替えることで，高次フィルタを用いることができる．本稿で提案するモニタリングアルゴリズムの有効性は QPSK 信号の伝送実験を行うことで確認した．

伝送路障害モニタリングを正しく行うためには，フィルタタップ長は十分長くなければならない．しかし，FIR フィルタの計算コストはタップ数とともに増加する．一方で，周波数領域での処理は．ブロック処理および DFT の高速実装によって計算コストを減少させることができる．しかし，これまで周波数領域における適応等化器は光通信分野ではほとんど研究されていなかった．このような状況下で，我々は CMA に基づく新たな適応 FDE を提案した．本提案手法は，偶数次及び奇数次のサブ等化器を用いている．本手法を用いることで，偏波多重分離及び ADC のサンプリング位相の調整を行うことができる．偏波多重 QPSK 信号の伝送実験を行うことで，我々が提案する適応 FDE の性能を評価した．

我々は新しい OSNR モニタリング技術を提案した．これは適応等化器出力の高次の統計学的モーメントを解析することで行われる．適応等化器の等化及びクロック再生後信号及び雑音は異なる統計的性質を持つ．我々のアルゴリズムでは 2 次および 4 次のモーメントを測定する．その後，位相変調信号および ASE の統計的性質を用いることで OSNR を推定する．我々は本方式の有効性を 10Gsymbol/s QPSK の伝送実験で確認した．

Acknowledgement

I would like to express my profound gratitude to my supervisor, Professor **Kazuro KIKUCHI**, for his precious guidance and continuous support during my doctoral course. I am very grateful to him for giving me a lot of time and energy for discussing the technical and fundamental issues about my research.

I would like to acknowledge Assistant Professor Koji Igarashi for his fruitful discussion, suggestions and cooperation in performing high speed transmission experiments.

I also would like to thank all of my lab members especially Hatori Takeshi for his tutoring, Yojiro Mori and Chao Zhang for their fruitful discussion and cooperation in performing experiments. Thanks to Mr. Kazuhiro Katoh and Ms. Baba for their academic assistance.

I am very grateful to the Ministry of Education, Culture, Sports, Science and Technology (MEXT), Japan, for providing me the scholarship throughout three years.

I am also grateful to the authority of Dhaka University of Engineering and Technology, Gazipur, Bangladesh for granting me the leave for pursuing of PhD degree.

I also owe a lot of thanks to my parents for their never ending encouragement, love, and support throughout my life; even though they were far from me physically for last three years, they were never far from my heart. Thanks to parents-in-law for their affection and inspirations.

Last of all, but not least, I would like to thank my wife, Rashna Sharmin for her understanding, love and encouragement and also for staying beside me in case of any difficulties.

List of Figures

List of Tables

Contents

Chapter 1

Introduction

1.1 Overview

The ever growing demand of internet traffic is the main driver in the deployment of higher capacity optical networks. Such high capacity-networks are being realized by using the advancement of technology such as erbium-doped fiber amplifier (EDFA), dense wavelength-division-multiplexing (DWDM) and advanced modulation schemes. Thus, the capacity of networks has been increased well beyond several Tb/s [1]. Meanwhile, introducing optical switches, the optical networks are becoming more flexible, reconfigurable and transparent. The stable operation of such networks are quite challenging as network paths are not static and channel degrading effects can change over time. A short service disruption of high capacity networks may affect an enormous amount of data. Optical performance monitoring (OPM), which refers to the physical layer monitoring for optical signal quality, is necessary to detect and prevent error to assure an agreed quality of service (QoS) to consumers [2, 3, 4, 5].

1.1.1 Need of OPM

OPM plays an important role for physical layer fault management and signal quality measurement. Not only that, OPM can enable different network management functionalities for next generation optical networks.

Many impairments on optical signal are time-varying due to change of environment, drift on components, rapid reconfiguration of network paths etc. Also, the fiber impairments depends on several complex interaction of linear and nonlinear effects which in turns depend on signal power, data rata and modulation formats. OPM can provide the real-time information of status of the network health. It ensures fault forecasting, detection, localization, diagnosis and resilience mechanism activation. Thus, OPM enables robust and stable operation of network to minimize the downtime while maximize the network availability.

OPM is required to allow scalability of the network. With the increasing bit-rate of the network the 'window of operability' [6] of the transmission system tends to shrink. For example, with increasing bit-rate, fiber transmission impairments such as chromatic dispersion (CD), polarization-mode dispersion (PMD) etc. reduce this window. Increasing the number of WDM channels further threaten to close the window due to fiber nonlinear effects. OPM is a potential mean of either widening this window or helping to maintain the channel operation within a small window.

The future networks are going to support different applications, because it is inefficient to use separate optical networks for each applications. Such *transparent networks* are going to cover different types of traffic and data formats. The network might require transmitting different modulation formats, wide range of data rates and variable QoS. Therefore, OPM should accommodate transparency [7].

For *reconfigurable networks*, currently the routing is done based on the shortest-path calculation or on path that satisfies certain QoS constraints. However, it will be more advantageous for network controller to take into account the physical state of the links into consideration for routing algorithm. For multivariable routing table, each link and optically-transparent node has a set of parameters such as fiber length, signal degradation, amplification, channel impairments and transients to calculate the 'cost function' of routing table. Therefore, OPM is required to provide the information of channel status and parameters so that the routing tables can dynamically reflect the state of physical links. This impairment-aware routing [8] would enables significant improvement in the blocking algorithm and the wavelength assignment algorithm [9].

The future networks might allow plug-and-play operation of an optical node to an existing network. Such *self-manage networks* should intelligently monitor the state of networks to automatically diagnosis and repair network fault, route traffic and dynamically allocate resources. Therefore, OPM is essential for ensuring high quality of operation of intelligent networks [7].

Thus, OPM will be not just a feature but a necessity for the next generation optical networks. The prerequisite is OPM should communicate with the higher control layer for optical network management (ONM) which will use the monitoring information to implement several functionalities for proper operation of the networks [10].

1.1.2 Existing OPM Methods

Previously, for performance monitoring, the bit-interleaved parity (BIP) bytes in SDH/SONET layer was widely used [11]. However, WDM network are now evolving from point-to-point link to dynamically-reconfigurable all optical networks; hence, it is not possible to monitor BIP bytes until signals reach end terminals [12]. For such networks, quality of the signal becomes more vulnerable to the optical layer impairments. Thus, for proper operation and management of the network, physical layer monitoring (ie, OPM) is more important. The broad spectrum of OPM includes a plethora of parameters to be monitored which consist of signal quality such as channel power, optical signal-to-noise ratio (OSNR), BER, Q-factor etc. monitoring and signal degradation parameters such as CD, PMD, polarization-dependent loss (PDL) and nonlinearity monitoring. However, in this research, we restrict our investigation in the OSNR and the linear impairments monitoring only, which are the most important aspects of OPM.

For dispersion (CD and PMD) monitoring, several methods have been demonstrated so far. One method is to insert a subcarrier (RF tone) at the transmitter, and then measures the resulting delay of the subcarrier sidebands relative to the baseband. Finally, the CD value is monitored from this delay [13, 14, 15]. It is also possible to estimate the PMD by spectral analysis of such RF tone, because the RF power is a function of PMD [16, 17, 18]. Such method is simple and applicable to WDM system; however, it requires modification of transmitter and additional consideration to separate the CD and PMD. An alternative technique is extraction of clock component from the photodetected data and monitors its RF power [19, 20]. Though this technique does not require transmitter modification, it is bit rate and modulation format dependent. Simultaneous CD and PMD monitoring based on the RF clock-tone power is demonstrated for NRZ OOK and DPSK signals [21]. The RF power is measured at the output ports of Mach-Zehnder delay line interferometer (DLI) with a quarter bit delay. By appropriately adding and subtracting clock power at constructive and destructive port of DLI, CD and PMD can be estimated. Another promising dispersion monitoring technique is the analysis of asynchronous amplitude histogram (AAH) [22]. With a sufficient number of random samples, AAH can evenly represents the pulse amplitude distribution and several parameters can be monitored without any clock recovery. However, this technique is also modulation format dependent. The others CD and PMD monitoring methods include measurements of relative group delay between vestigial sideband (VSB) signals [23], pilot tone assisted monitoring [24],

utilization of nonlinear effects of fiber [25], using artificial neural networks (ANN) [26], measurement of degree of polarization [27], heterodyne detection and processing of IF signals [28], etc.

As for the OSNR monitoring methods, it can be broadly classified into two categories: out-of-band and in-band monitoring, depending on whether the noise power is measured outside or within the wavelength channel pass band. The traditional out-of-band monitoring technique involves measuring and interpolating noise power from adjacent channel by measuring optical spectrum [29]. Though such method is simple, out-of-band monitoring is not always reliable. Because, in a dynamically reconfigurable WDM network, the linearly interpolated ASE noise may not be the real ASE noise in the channels of interest, since in such WDM network each channel may traverse different routes and different numbers of erbium-doped fiber amplifiers (EDFAs), optical filters, OADMs/OXCs, etc. Therefore, the in-band OSNR monitoring is highly motivated. There are several methods for the in-band OSNR monitoring. One of such method is the polarization nulling method [30, 31] which makes use of the fact that the signal component is polarized while the ASE noise component is unpolarized. By using the polarization controller and polarizer, the output is adjusted to measure total power and noise power. However, generally the performance of such method degrades severely under the influence of large PMD and PDL. Another method for the in-band OSNR monitoring is to use the subcarrier in each wavelength signal. The electrical carrier-to-noise ratio (CNR) of the subcarrier is determined and the OSNR is obtained through mathematical relation with the CNR [13]. However, this technique requires transmitter modifications. Electronic technique such as asynchronous histogram method is also an attractive option for the OSNR monitoring; however, this method is modulation format dependent [32]. Other OSNR monitoring methods include optical parametric amplification based schemes [33], artificial neural network based monitoring [26], uncorrelated beat noise estimation method [34] etc.

Recently, digital signal processing (DSP) based OPM in digital coherent receivers has been investigated in several literatures [35, 36, 37, 38]. Most of them are fiber transmission impairments monitoring from adaptive FIR filters. The method is based on the analysis of transfer functions of the adaptive finite-impulse-response (FIR) filters structured in a two-by-two butterfly configuration. After the filters are adapted, a frequency dependent two-by-two matrix is formed with four elements, which are transfer functions of the adapted four FIR filters. The

inverse of this matrix is called monitoring matrix and can be approximated as the transfer matrix of the channel, and contains combined effects of CD, PMD and PDL. A precise algorithm is required to separate all impairments from this matrix. Reference [35] neglects the effect of PDL when determining CD and differential group delay (DGD) between two principal states of polarization (PSPs). Thus, the fiber transmission matrix is considered as unitary matrix. Then, the DGD is estimated by manipulating the elements of unitary matrix and sinusoidal curve fitting. However, such approach is rather complicated, because it needs some adjustment of the matrix element and sophisticated technique for curve fittings. Moreover, in presence of PDL, the transfer matrix is no longer a unitary matrix and the proposed scheme failed to monitor DGD accurately. An extension work of [35] is presented in [36] where PDL monitoring is included. However, in the proposed scheme, an OSNR monitor is needed prior to the PDL estimation.

In [37] a similar approach is followed for CD and DGD monitoring where the effect of PDL is excluded for DGD monitoring algorithm. For PDL monitoring a complicated procedure is followed which requires estimation of power ratio and loss of orthogonality between two polarization tributaries. Ref. [38] requires matrix decomposition before separating out individual impairment.

It should be noted here that none of the above mentioned works have investigated monitoring of the second-order PMD. An accurate OSNR estimation technique in digital coherent receivers has also not been investigated.

1.2 Objectives of This Research

The objectives of this research are to enable OPM in digital coherent receivers. The main motivations are as follows:

- Develop novel algorithms to enable multi-impairment monitoring from adaptive FIR filters

The new algorithm should be capable of monitoring all linear impairments, namely, CD, DGD, PDL and second-order PMD. It should be simple and efficient, and avoid any extra devices for monitoring. Also, a reliable and efficient filter adaptation algorithm is to be developed to ensure monitoring accuracy.

- Find new ways to efficiently implement long tap filters to enhance multi-impairment monitoring range

To reduce the computational complexity of conventional equalizers based on time-domain FIR filters, adaptive frequency-domain equalizer (FDE) can be employed. However, adaptive FDE has hardly been investigated for digital coherent receivers. Hence, an adaptive FDE should be developed that will be compatible to coherent communication systems. Efficient multi-impairment monitoring with large range could be enabled with such adaptive FDE.

- Develop new ideas for monitoring of OSNR in digital coherent receivers

The new OSNR monitoring technique in digital coherent receivers should be simple and accurate. It should be able to estimate in-band OSNR for any bit rate and commonly used modulation formats.

1.3 Thesis Organization

This thesis is organized in six chapters, including the current introduction chapter which contains research overview, objectives of this research and layout of this thesis dissertation.

In chapter 2, the background knowledge of digital coherent receivers, which is necessary to understand the rest of the thesis, is introduced. In Sec. 2.1, the principle of coherent detection is introduced followed by a detailed description of the phase diversity and phase and polarization diversity homodyne receiver scheme. In Sec. 2.2, the concept of digital coherent receivers is explained. Also, the description of different DSP circuits in the digital coherent receivers is reported. Section 2.3 summarized this chapter.

In chapter 3, our proposed multi-impairment monitoring technique from adaptive FIR filters is focused. Section 3.1 outlines a theoretical background related to this chapter. It includes detailed explanations of conventional adaptive equalization algorithms and the channel model for optical signal transmission, which is later used for developing the monitoring algorithm. In Sec. 3.2, we introduce our proposed equalization algorithm (CMA with the training mode) that is used throughout the thesis. Section 3.3 describes the novel multi-impairment algorithm that separates out all linear impairments from the transfer function of adapted FIR filters. In Sec. 3.4

experimental verifications of our proposed equalization and monitoring algorithms are demonstrated. Section 3.5 summarizes this chapter.

In chapter 4, a novel frequency-domain approach of adaptive equalization is introduced and muti-impairment monitoring from such adaptive FDE is demonstrated. Section 4.1 explains the theoretical background necessary to develop the adaptive FDE later in this chapter. Section 4.2 presents detailed theoretical and mathematical description of our proposed adaptive FDE. Section 4.3 compares the computational cost of the adaptive FDE with its counter part of the conventional time-domain equalizer (TDE). Section 4.4 describes the multi-impairment monitoring method from the proposed adaptive FDE. In Sec. 4.5, experimental verification is demonstrated. Both equalization and monitoring performance are shown and discussed. Section 4.6 summarizes this chapter.

In chapter 5, a new method of OSNR monitoring is discussed. Section 5.1 describes the theoretical background to understand the rest of the chapter. Section 5.2 focuses on the proposed OSNR monitoring algorithm. It is based on the second- and fourth-order statistical moments of the output signal from the adaptive equalizer. In Sec. 5.3 the experimental results regarding the proposed OSNR monitoring method is discussed. Section 5.4 summarizes the chapter.

In Chapter 6, the conclusions of this thesis are drawn and some future works are outlined.

References

1. R. Essiambre, G. Foschini, P. Winzer, and G. Kramer, "Capacity limits of fiber-optic communication systems," in *Optical Fiber Communication Conference*, OSA Technical Digest (CD) (Optical Society of America, 2009), paper OMJ5.
2. D. C. Kilper, R. Bach, D. J. Blumenthal, D. Einstein, T. Landolsi, L. Ostar, M. Preiss and A. E. Willner, "Optical performance monitoring," J. Lightwave Technol. **22**, 294-304 (2004).
3. A. E. Willner, *Optical Fiber Telecommunication V B* (Academic press, 2008), Chap.7.
4. Z. Pan, C. Yu, and A. E. Willner, "Optical performance monitoring for next generation optical communication networks," Opt. Fiber Technol. **16**, 20-45 (2010).
5. M. N. Petersen, "Performance monitoring in the next generation of optical network," in *Proceedings of Phonics in Switching* (2006).

6. F. Forghieri, R. W. Tkach, and A. R. Chraplyvy, *Optical Fiber Telecommunication IIIA* (Academic press 1997), Chapter 8.
7. A. E. Willner, "The optical network of the future: Can optical performance monitoring enable automated, intelligent and robust systems?," Opt. and Photon. News **17**, 30-35 (2006).
8. K. Guild, "Impairments-aware routing for OBS and OPS network," in *Proceedings of International Conference on Transparent Optical Networks* (2006), paper Mo.D3.3.
9. Y. Huang, J. P. Heritage, and B. Mukherjee, "Connection provisioning with transmission impairments consideration in optical WDM networks with high-speed channels," J. Lightwave Technol. **23**, 982-993 (2005).
10. L. Chen, M. Cheung, and C. Chan, "From optical performance monitoring to optical network management: Research progress and challenges," in *Proceedings of International Conference on Optical Communications and Networks* (2004).
11. ITU G.826 standards.
12. Y. C. Chung, "Optical performance monitoring techniques; current status and future challenges," in *Proceedings of European Conference on Optical Communication* (ECOC), paper We.1.D.1.
13. G. Rossi, T. E. Dimmick, and D. J. Blumenthal, "Optical performance monitoring in reconfigurable WDM optical networks using subcarrier multiplexing," J. Lightwave Technol. **18**, 1639-1648 (2000).
14. M. N. Petersen, Z. Pan, S. Lee, S. A. Havstad, and A. E. Willner, "Online chromatic dispersion monitoring and compensation using a single inband subcarrier tone," IEEE Photon. Technol. Lett. **14**, 570-572 (2002).
15. N. Lui, W.-D. Zhong, Y. J. Wen, and Z. Lee, "New transmitter configuration for subcarrier multiplexed DPSK systems and its application to CD monitoring," Opt. Express **15**, 839-944 (2007).
16. G. Ishikawa and H. Ooi, "Polarization-mode dispersion sensitivity and monitoring in 40-Gbits/s OTDM and 10 Gbits/s NRZ transmission experiments," in *Optical Fiber Communication Conference*, OSA Technical Digest (CD) (Optical Society of America, 1998), paper WC5.

17. A. E. Willner, S. M. R. Motaghian, L. S. Yan, Z. Pan, and M. Hauer, "Monitoring and control of polarization-related impairments in optical fiber systems," J. Lightwave Technol. **22**, 106-125 (2004) .
18. R. Noé, D. Sandel, M. Yoshida-Dierrolf, S. Hinz, V. Mirvoda, A. Schopflin, C. Gungener, E. Gottwald, C. Scheerer, G. Fischer, T. Weyrauch, and W. Haase, "Polarization mode dispersion compensation at 10, 20, and 40 Gb/s with various optical equalizer," J. Lightwave Technol. **17**, 1602-1616 (1999).
19. Z. Pan, Q. Yu, Y. Xie, S. A. Havstad, A. E. Willner, D. S. Starodubov, and J. Feinberg, "Real-time group-velocity dispersion monitoring and automated compensation without modification of transmitter," Opt. Commun. **230**, 145-149 (2004).
20. G. Ishikawa and H. Ooi, " Demonstration of automated dispersion equalization in 40 Gb/s OTDM transmission," in *Proceedings of European Conference on Optical Communication* (1998).
21. Y. K. Lize, L. Christen, J.-Y. Yang, P. Saghari, S. Nuccio, A. E. Willner, and R. Kashyap, "Independent and simultaneous monitoring of chromatic and polarization-mode dispersion in OOK and DPSK transmission," IEEE Photonics Technol. Lett. **19**, 3-5 (2007).
22. Z. Li and G. Li, "Chromatic dispersion and polarization-mode dispersion monitoring for RZ-DPSK signals based on asynchronous amplitude histogram evaluation," J. Lightwave Technol. **24**, 2859-2866 (2006).
23. Q. Yu, Z. Pan, L. -S. Yan, and A. E. Willner, "Chromatic dispersion monitoring technique using sideband optical filtering and clock phase-shift detection," J. Lightwave Technol. **20**, 2267-2271 (2002).
24. H. Ji, K. Park, J. Lee, H. Chung, E. Son, K. Han, S. Jun, and Y. Chung, "Optical performance monitoring techniques based on pilot tones for WDM network applications," J. Opt. Netw. **3**, 510-533 (2004).
25. S. Widelandy, M. Fishteyn, and B. Zhu, "Optical performance monitoring using nonlinear detection," J. Lightwave Technol. **22**, 784-793 (2004).
26. X. Wu, J. A. Jargon, R. A. Skoog, L. Paraschis, and A. E. Willner, "Applications of artificial neutral networks in optical performance monitoring," J. Lightwave Technol. **27**, 3580-3589 (2009).

27. S. Lanne, W. Idler, J. P. Thiery, and J. P. Hamaide, "Fully automatic PMD compensation at 40Gbits/s," IEE Electron. Lett. **38**, 40-41 (2001).
28. B. Fu and R. Hui, "Fiber chromatic dispersion and polarization mode dispersion monitoring using coherent detection," IEEE Photon. Technol. Lett. **17**, 1561- 1563 (2005).
29. H. Suzuki and N. Takachio, "*Optical signal quality monitor built into WDM linear repeaters using semiconductor arrayed waveguide grating filter monolithically integrated with eight photodiodes," Electron. Lett. **35**, 836-837 (1999).*
30. *J. H. Lee and Y. C. Chung, "Improved OSNR monitoring technique based on polarization-nulling method," Electron. Lett. **37**, 972-973(2001).*
31. *J. H. Lee, H. Y. Choi, S. K. Shin, and Y.C. Chung, "A review of the polarization-nulling technique for monitoring optical-signal-to-noise ratio in dynamic WDM networks,"* J. Lightwave Technol. **24**, 4126-4171 (2006).
32. B. Kozicki, O. Takuya, and T. Hidehiko, "Optical performance monitoring of phase-modulated signals using asynchronous amplitude histogram analysis," J. Lightwave Technol. **26**, 1353-1361 (2008).
33. T. Ng, J. L. Blows, M. Rochette, J. A. Bolger, I. Littler, and B. Eggleton, "In-band OSNR and chromatic dispersion monitoring using a fiber optical parametric amplifier," Opt. Express, **15**, 5542-5552 (2005).
34. W. Chen, R. S. Tucker, X. Yi, W. Shieh, and J. S. Evans, "Optical signal-to-noise ratio monitoring using uncorrelated beat noise," IEEE Photon. Technol. Lett. **17**, 2484-2486 (2005).
35. F. N. Hauske, J. C. Geyer, M. Kuschnerov, K. Piyawanno, T. Duthel, C. R. S. Fludger, D. van den Borne, E.-D. Schmidt, B. Spinnler, H. de Waardt, and B. Lankl, "Optical performance monitoring from FIR filter co-efficients in coherent receivers," in *Optical Fiber Communication Conference*, OSA Technical Digest (CD) (Optical Society of America, 2008), paper OThW2.
36. F. N. Hauske, M. Kuschnerov, B. Spinnler, and B. Lankl, "Optical performance monitoring in digital coherent receivers," J. Lightwave Technol. **27**, 3623-2631(2009).

37. J. C. Geyer, F. N. Hauske, C. R. S. Fludger, T. Duthel, C. Schulien, M. Kuschnerov, K. Piyawanno, D. van den Borne, E.-D. Schmidt, B. Spinnler, B. Lankl, and B. Schmauss, "Channel parameter estimation for polarization diverse coherent receives," IEEE Photon. Technol. Lett. **20**, 776-778 (2008).
38. J. C. Geyer, C. R. S. Fludger, T. Duthel, C. Schulien, and B. Schmauss, "Performance monitoring using coherent receiver," in *Optical Fiber Communication Conference*, OSA Technical Digest (CD) (Optical Society of America, 2009), paper OThH5.

Chapter 2

Background of Digital Coherent Receivers

The employment of coherent receivers in optical communication systems became popular in 1980s [1]. The main drive of such research was for improving receiver sensitivity over intensity modulation/direct detection (IM/DD) system due to scarcity of efficient optical amplifier. With a sufficient local oscillator (LO) power, the shot-noise limited receiver sensitivity was achieved. However, the advent of Erbium doped fiber amplifier (EDFA), the shot-noise limited receiver sensitivity of the coherent receiver became less important as the signal-to-noise ratio (SNR) of the signal transmitted through the amplifier chain is determined from accumulated amplified spontaneous emission (ASE) noise rather than the shot noise. Even in the unrepeated transmission, the EDFA can be used as pre-amplifier, thus eliminating the need of coherent receivers for its better sensitivity. For this reason, the further research and development activities regarding coherent communication systems have been interrupted for about 20 years.

Nowadays, the employment of higher-order modulation formats is becoming a necessity for its higher spectral efficiency to meet ever increasing bandwidth demand. In fact, such complex modulation format can be employed with coherent receivers, because such receivers can retrieve whole complex field of the received lightwave. Thus, research of coherent systems again comes in center of attention. The alternative of the coherent detection, the delay detection [2] is not so attractive, because beyond QPSK such scheme can hardly be realized due to higher complexity.

The main obstacles for practical implementation of traditional coherent receivers are phase and polarization tracking. Due to the fiber birefringence, the output state of polarization (SOP) in the fiber fluctuates without matching the SOP of LO. Phase locking is also necessary. Dynamic control of SOP requires bulky and costly devices and use of optical phase lock loop (OPLL) for phase tracking is not practically feasible due to high complexity and stringent requirements for laser linewidth.

On the other hand, phase and polarization diversity homodyne detection followed by digital signal processing (DSP) eliminates such obstacles of SOP and phase tracking [3, 4, and ref. therein]. Such a DSP-based coherent optical receiver is generally termed as a digital coherent

receiver. The recent deployment in DSP integration makes it practically viable. Any kind of multilevel modulation can be employed with such receivers [5, 6, 7, 8, 9, 10]. More importantly, all of fiber transmission impairments can be compensated for in electric domain [11, 12, 13, 14, 15]; thus a dispersion compensation fiber (DCF) and an optical polarization mode dispersion (PMD) compensator can be eliminated from the link.

Note that, due to the requirements of high speed ADCs and DSP circuits, most of the experimental demonstrations based on digital coherent receivers have been done offline. However, several demonstrations of real-time operation of such receivers have also been reported by using either application-specific integrated circuit (ASIC) [16, 17, 18] or field-programmable gate array (FPGA) [19, 20, 21, 22].

This chapter provides the background theory of such DSP-based coherent optical receivers which will be necessary to understand the rest of the thesis. Section 2.2 provides the principle of coherent detection and Sec. 2.3 provides the concept of digital coherent receivers and a brief description of DSP functions in such receivers. Section 2.4 summarizes this chapter.

2.1 Principle of Coherent Detection

2.1.1 Coherent Detection

The fundamental concept of coherent detection is to mix the electric field of modulated signal light and continuous-wave local oscillator (LO). Let the optical signal from the transmitter be expressed as

$$E_s(t) = A_s(t)\exp(j\omega_s t), \tag{2.1}$$

where $A_s(t)$ is the complex amplitude and ω_s is angular frequency. Similarly, the electric field of LO is given as

$$E_{LO}(t) = A_{Lo}(t)\exp(j\omega_{LO} t), \tag{2.2}$$

where $A_{LO}(t)$ is the complex amplitude and ω_{LO} is angular frequency of the LO. Note that the complex amplitude A_s and A_{LO} is related to their power of optical field P_s and P_{LO}, respectively as $P_s = |A_s|^2/2$ and $P_{LO} = |A_{LO}|^2/2$.

Generally, a balanced detection is used in coherent detection to suppress the DC components and maximize signal photo-current. Such a scheme is shown in Fig. 2.1 where a 3-dB coupler is

used to add a 180° phase shift to either signal field or LO field. Considering LO and signal are copolarized, the electric fields incident on the upper and lower photodiodes are expressed as

$$E_1(t) = \frac{1}{\sqrt{2}}\left\{E_s(t) + E_{LO}(t)\right\}, \tag{2.3}$$

$$E_2(t) = \frac{1}{\sqrt{2}}\left\{E_s(t) - E_{LO}(t)\right\}. \tag{2.4}$$

Considering a PSK modulated signal, the signal phase, $\theta_{sig}(t)$ is given as $\theta_{sig}(t) = \theta_s(t) + \theta_{sn}(t)$, where θ_s is the phase modulation and θ_{sn} is the phase noise. We also define the total phase noise θ_n as $\theta_n(t) = \theta_{sn}(t) - \theta_{LO}(t)$, θ_{LO} being the phase of LO. With these notations, the photo-currents can be written as

$$\begin{aligned} I_1(t) &= R\left[\mathrm{Re}\left\{E_1(t)\right\}\right]^{ms} \\ &= \frac{R}{2}\left[P_S(t) + P_{LO} + 2\sqrt{P_s(t)P_{LO}}\cos\left\{\omega_{IF}t + \theta_s(t) + \theta_n(t)\right\}\right], \end{aligned} \tag{2.5}$$

$$\begin{aligned} I_2(t) &= R\left[\mathrm{Re}\left\{E_2(t)\right\}\right]^{ms} \\ &= \frac{R}{2}\left[P_S(t) + P_{LO} - 2\sqrt{P_s(t)P_{LO}}\cos\left\{\omega_{IF}t + \theta_s(t) + \theta_n(t)\right\}\right], \end{aligned} \tag{2.6}$$

where 'ms' denotes the mean square with respect to optical frequencies, 'Re' is the real part and ω_{IF} is the IF given by $\omega_{IF} = \omega_s - \omega_{LO}$, respectively. The responsitivity of the photodiodes R is given as

$$R = \frac{e\eta}{\hbar\omega_s}, \tag{2.7}$$

where $\hbar$ stands for Plank's constant, e is the charge of electron, and η is the quantum efficiency of the photo-diode.

The balanced detector output can be found from Eq. (2.5) and (2.6) as

$$I(t) = I_1(t) - I_2(t) = 2R\sqrt{P_s(t)P_{LO}}\cos\left\{\omega_{IF}t + \theta_s(t) + \theta_n(t)\right\}. \tag{2.8}$$

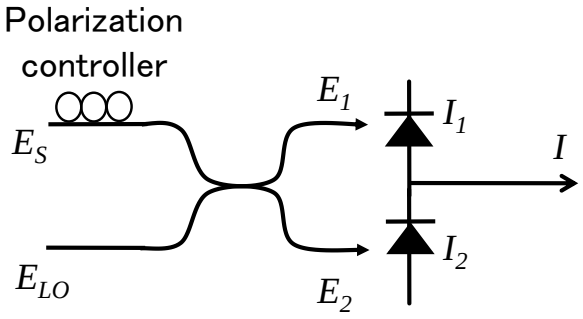

Fig. 2.1: Configuration of coherent receiver that measures beat between the signal and LO

Depending on the value of ω_{IF}, coherent detection can be classified as either heterodyne or homodyne detection. In case of heterodyne detection, $|\omega_{IF}| >> \omega_b/2$, where ω_b is modulation bandwidth of the optical carrier determined by the bit rate. As shown in Eq. (2.8) the electric field of the signal light is down-converted to an IF signal that includes both amplitude and phase information. We can determine the complex amplitude on $\exp(j\omega_{IF}t)$ from Eq. (2.8) as

$$I_C(t) = 2R\sqrt{P_s(t)P_{LO}}\exp j\left\{\theta_s(t) + \theta_n(t)\right\}. \tag{2.9}$$

As shown in Eq. (2.9), $I_C(t)$ is equivalent to $A_s(t)$ except the incremental phase noise stemming from LO. There are several methods to demodulate $I_c(t)$ such as envelope (non-coherent) detection, differential (delay) detection and synchronous (coherent) detection.

On the other hand, in case of homodyne detection, $\omega_{IF}=0$. The photocurrent can be written from Eq. (2.7) as

$$I(t) = 2R\sqrt{P_s(t)P_{LO}}\cos\left\{\theta_s(t) + \theta_n(t)\right\}. \tag{2.10}$$

As shown in Eq. (2.10), in order to decode the symbol correctly, the LO phase must track with the transmitter phase noise so that θ_n can be zero. Such function can be realized by an OPLL; however, such loop is not simple and adds complexity to the homodyne receiver. Moreover, Eq. (2.10) gives only the cosine component (in-phase component with respect to the LO phase) and

the sine component (the quadrature component) cannot be detected. Therefore, this type of homodyne receiver cannot extract the complex amplitude of the signal.

2.1.2 Phase Diversity Homodyne Receiver

Preparing another LO, whose phase is shifted by 90°, in the homodyne receiver, we can extract both sine and cosine components. This function can be achieved by introducing a 90° optical hybrid. As shown in Fig. 2.2, by using a 90° hybrid, we can obtain four outputs E_1, E_2, E_3, and E_4 from two inputs E_s and E_{LO} as

$$E_1(t) = \frac{1}{2}\left\{E_s(t) + E_{LO}(t)\right\}, \tag{2.11}$$

$$E_2(t) = \frac{1}{2}\left\{E_s(t) - E_{LO}(t)\right\}, \tag{2.12}$$

$$E_3(t) = \frac{1}{2}\left\{E_s(t) + jE_{LO}(t)\right\}, \tag{2.13}$$

$$E_4(t) = \frac{1}{2}\left\{E_s(t) - jE_{LO}(t)\right\}. \tag{2.14}$$

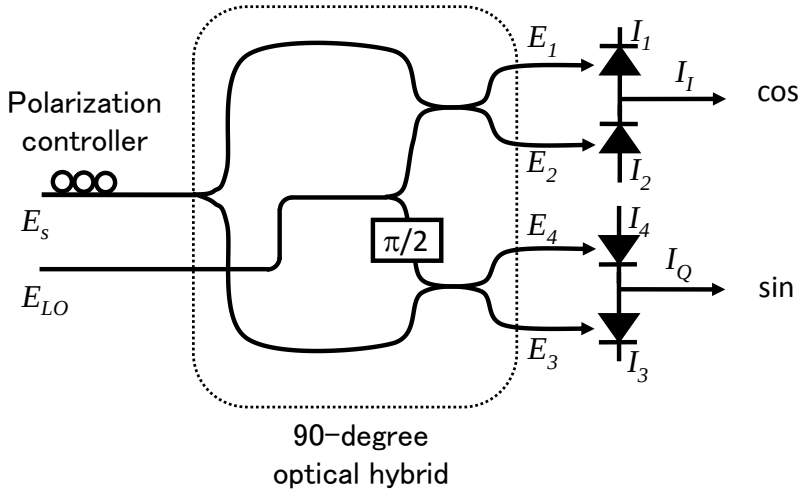

Fig. 2.2: Configuration of phase diversity homodyne receiver

Correspondingly, the photo-currents from balanced photodetectors are given as

$$I_I(t) = I_{I1}(t) - I_{I2}(t) = R\sqrt{P_s(t)P_{LO}}\cos\left\{\theta_s(t) + \theta_n(t)\right\}, \tag{2.15}$$

$$I_Q(t) = I_{Q1}(t) - I_{Q2}(t) = R\sqrt{P_s(t)P_{LO}}\sin\{\theta_s(t) + \theta_n(t)\}. \quad (2.16)$$

From Eqs. (2.15) and (2.16), we can obtain the complex amplitude as

$$I_C(t) = I_I(t) + jI_Q(t) = R\sqrt{P_s(t)P_{LO}}\exp\{\theta_s(t) + \theta_n(t)\}, \quad (2.17)$$

which is equivalent to the complex amplitude of the optical signal except for the phase noise increase.

This type of receiver is commonly termed as "phase diversity homodyne receiver" [23] because the signal amplitude can be determined independently from the measured sine and cosine components. It is also termed as "intradyne receiver" [24] because the optical complex amplitude is restored in the baseband without frequency and phase locking.

The complex amplitude $I_C(t)$ given by Eq. (2.17) can be demodulated by using the similar techniques used for heterodyne detection- envelope (non-coherent) detection, differential (delay) detection and synchronous (coherent) detection. Note that, we can avoid OPLL used in synchronous detection, if we estimate the phase noise through DSP on the homodyne detected signal given by Eq. (2.17). This is the basic idea of 'digital coherent receiver' which will be discussed later in this chapter.

Both the phase diversity homodyne receiver and the heterodyne receiver can restore full information on the optical complex amplitude; however, the homodyne receiver is best suited for digital coherent receivers because it generates the baseband signal directly, whereas the heterodyne receiver deals with a rather high intermediate frequency.

2.1.3 Homodyne Receiver Employing Phase and Polarization Diversities

The state of polarization of the incoming signal plays no role on in direct detection receiver. The photo-current of such receiver depends only on the number of incident photons. On the other hand, in case of the coherent receiver, the receiver sensitivity is dependent on SOP of the incoming signal. In practical systems, it is unlikely that SOP of the incoming signal will be always aligned to that of LO. This is because SOP of incoming signal changes with the random variation of fiber birefringence, while that of LO is determined by the laser and remains fixed. The polarization-diversity receiver architecture can solve this polarization mismatch problem [25].

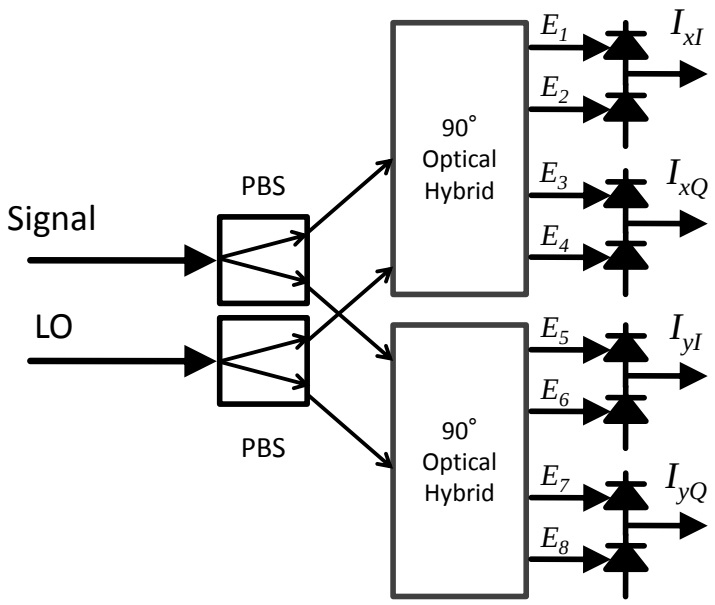

Fig. 2.3: Schematic of homodyne receiver employing phase and polarization diversity

The homodyne receiver that employs both phase and polarization diversities is shown in Fig. 2.3. The incoming signal having an arbitrary SOP is first separated into two linear polarization components by a polarization beam splitter (PBS). Let the *x*- and *y*- polarization components after the PBS are given as

$$\begin{bmatrix} E_{sx}(t) \\ E_{sy}(t) \end{bmatrix} = \begin{bmatrix} \sqrt{\alpha} A_s(t) \exp(j\delta) \\ \sqrt{1-\alpha} A_s(t) \end{bmatrix} \exp(j\omega_s t), \tag{2.18}$$

where α is power splitting ratio of two polarization components and δ is the phase difference between them. These parameters are time-varying and depend on the fiber birefringence. On the other hand, *x*- and *y*-polarization components of LO can be written as

$$\begin{bmatrix} E_{LOx}(t) \\ E_{LOy}(t) \end{bmatrix} = \frac{1}{\sqrt{2}} \begin{bmatrix} A_{LO}(t) \\ A_{LO}(t) \end{bmatrix} \exp(j\omega_{LO} t). \tag{2.19}$$

Two 90° optical hybrids in Fig. 2.3 generate eight electric fields $E_{1,2,\ldots,8}$ at the double balanced photodiodes PD_1-PD_4 as

$$E_{1,2}(t) = \frac{1}{2}\left(E_{sx}(t) \pm \frac{1}{\sqrt{2}} E_{LO}(t) \right), \tag{2.20}$$

$$E_{3,4}(t)=\frac{1}{2}\left(E_{sx}(t)\pm\frac{j}{\sqrt{2}}E_{LO}(t)\right), \tag{2.21}$$

$$E_{5,6}(t)=\frac{1}{2}\left(E_{sy}(t)\pm\frac{1}{\sqrt{2}}E_{LO}(t)\right), \tag{2.22}$$

$$E_{7,8}(t)=\frac{1}{2}\left(E_{sy}(t)\pm\frac{j}{\sqrt{2}}E_{LO}(t)\right), \tag{2.23}$$

where $E_{LO}=E_{LO,x}=E_{LO,y}$. Correspondingly, the photo-currents from PD_1 to PD_4 are given as

$$I_{xI}(t)=R\sqrt{\frac{\alpha P_s(t)P_{LO}}{2}}\cos\left\{\theta_s(t)+\theta_n(t)+\delta\right\}, \tag{2.24}$$

$$I_{xQ}(t)=R\sqrt{\frac{\alpha P_s(t)P_{LO}}{2}}\sin\left\{\theta_s(t)+\theta_n(t)+\delta\right\}, \tag{2.25}$$

$$I_{yI}(t)=R\sqrt{\frac{(1-\alpha)P_s(t)P_{LO}}{2}}\cos\left\{\theta_s(t)+\theta_n(t)+\delta\right\}, \tag{2.26}$$

$$I_{yQ}(t)=R\sqrt{\frac{(1-\alpha)P_s(t)P_{LO}}{2}}\sin\left\{\theta_s(t)+\theta_n(t)+\delta\right\}. \tag{2.27}$$

We can measure complex amplitudes of the two polarization components by using Eqs. (2.24)-(2.27) as

$$I_{xC}(t)=I_{xI}(t)+jI_{xQ}(t), \tag{2.28}$$

$$I_{yC}(t)=I_{xI}(t)+jI_{xQ}(t), \tag{2.29}$$

from which the complex amplitude can be constructed in a polarization-independent manner. This can be done with no notable penalty by the maximal-ratio combiner method [26, 27].

2.2 Concept of Digital Coherent Receivers

2.2.1 Basic Concept of Digital Coherent Receiver

The basic concept of digital coherent receivers is depicted in Fig. 2.4. First, the incoming signal is linearly detected by a phase and polarization diversity coherent optical receiver. With such

scheme, both the complex amplitude and SOP of the signal are detected. Then, the complex amplitude is converted to digital data by analog-to-digital converters (ADCs) and processed by the DSP. The progress in speed, performance and reliability of integrated circuits makes the DSP circuit practically feasible to recover the complex amplitude from homodyne-detected baseband signals.

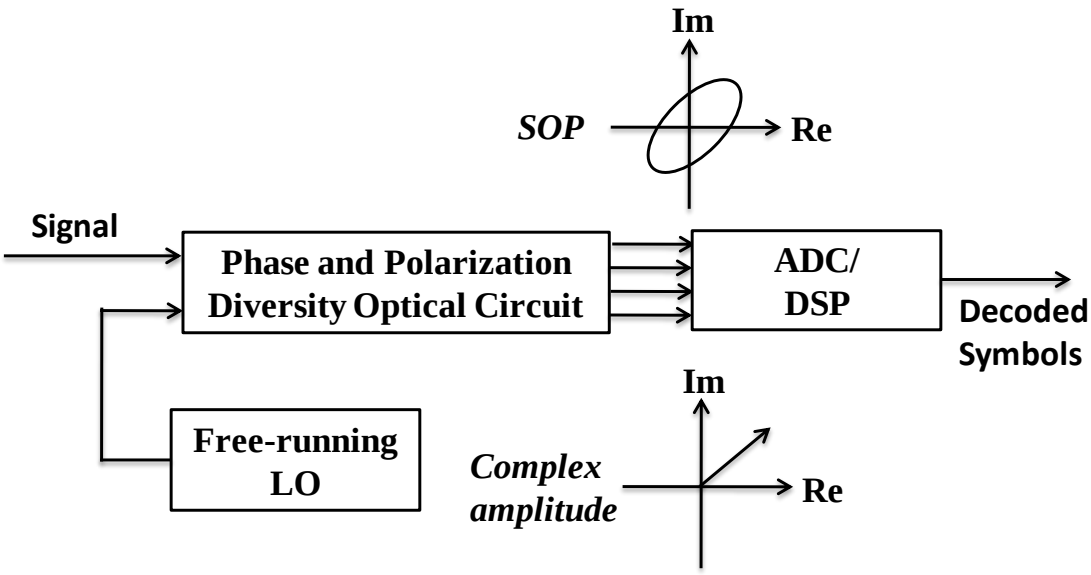

Fig. 2.4: Concept of digital coherent receiver

The combination of the optical IQ modulator and the IQ demodulator realizes the linear optical communication system. At the transmitter, a vector in the complex plain is defined using two voltages driving the IQ modulator. This vector is then mapped on the phasor of the optical carrier through the IQ modulator and such complex signal is completely restored by the digital coherent receiver. This is exactly the linear system, where IQ information is preserved even with the E/O or O/E conversion process.

2.2.2 Digital Signal Processing

Considering the dual-polarization transmission system, to recover the information from the modulated signals, the DSP circuits must perform the following operations:

- Sampling and digitizing the analog signal by ADCs,
- Compensation for static channel impairments,

- Polarization demultiplexing,
- Clock-recovery,
- Equalization of time-varying linear impairments,
- Estimation of carrier phase and IF offset,
- Decoding.

Throughout this thesis, the above operations are achieved using the functional blocks shown in Fig. 2.5.

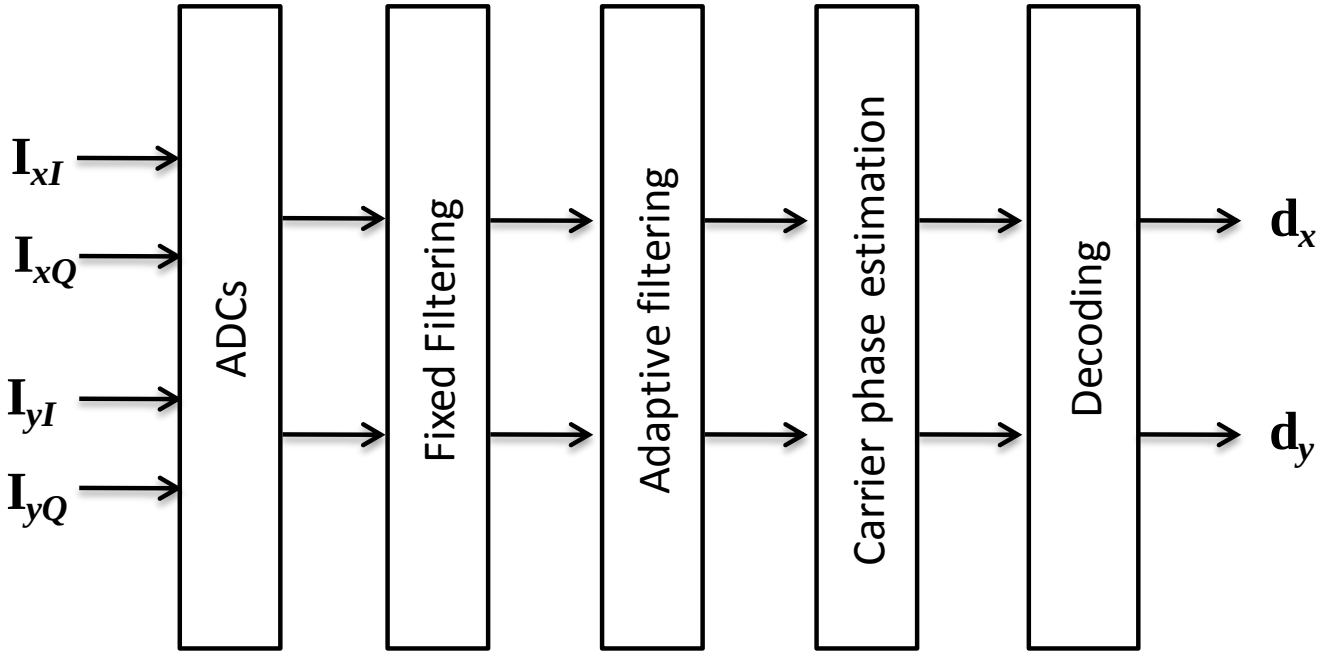

Fig. 2.5: Functional blocks in a DSP core of digital coherent receivers

Sampling and digitizing

After coherent detection of the incoming signal by a phase and polarization diversity receiver, four ADCs convert *I* and *Q* data of two polarization tributaries. In order to recover the signal information, the sampling frequency of the ADCs should be at least equal to the symbol rate of the system, provided that the ADCs are synchronized by any clock recovery technique. In systems that do not use a clock recovery stage before the analog-to-digital conversion, the sampling frequency of the ADCs is generally double the symbol rate. With a two-fold oversampled sequence, an adaptive filter can essentially perform clock recovery [28]. Moreover, such oversampling reduces the aliasing effect [29]. Dual-polarization QPSK modulation format

is considered for the candidate of future 100-Gbits/s Ethernet standard and recent advancement of the ADC speed allows two-fold oversampling even for such systems [30].

Fixed Filtering

A fixed filter is used for equalization of linear static-channel impairments, mainly CD compensation. The CD is one of the most impairing phenomena that affect a signal transmitted through an optical fiber. For digital coherent receivers, CD can be compensated by either in the optical domain by DCFs or in the digital domain by using digital filters. However, the latter one is more suitable because system installation can be made more cost-effective and also tolerant to fiber nonlinear effects [31,32].

Since CD varies very slowly in a fiber link, the CD equalizer is generally implemented by a fixed filter prior to an adaptive filter. Usually, two types of equalizers are investigated for the CD compensation: time-domain equalizer (TDE) [33, 34] or frequency-domain equalizer (FDE) [35]. The choice between TDE and FDE mainly depends on the maximum dispersion in the channel and the resulting filter length [36]. Generally, complexity of a FDE grows much slower with the amount of CD; therefore, FDE is suitable for long-haul transmission where accumulated dispersion is very large.

For both the approaches, the knowledge of accumulated dispersion value is necessary. The CD transfer function can be expressed, in the case of the second order approximation, as [37]:

$$H_{CD}(\omega) = \exp(-j\frac{D\lambda^2 L}{4\pi c}\omega^2), \tag{2.30}$$

where λ is the carrier wavelength, D is dispersion parameter, L is fiber link length, and c is the speed of light. Thus, the dispersion compensating filter can be designed as an all-pass filter with the transfer function

$$H_{f,CD}(\omega) = \frac{1}{H_{CD}(\omega)}. \tag{2.31}$$

Another approach to find the filter transfer function is to estimate the CD at the start up by using some adaptive [38] or non-adaptive algorithms [39] and then to use the estimated value for fixed filtering.

For TDE implementation, a finite-impulse-response (FIR) filter can be used with a tapped delay line as shown in Fig. 2.6. If we assume that the number of taps is large, then the discrete impulse response of the filter can be approximated as the continuous time impulse response. Savory [33] has obtained a simple closed form solution for the tap weights that also provides an upper bound on the number of taps required for a given value of dispersion. The form of the tap weights are as follows:

$$h_k = \sqrt{\frac{jcT^2}{D\lambda^2 L}} \exp\left(-j\frac{\pi c T^2}{D\lambda^2 L}k^2\right); -\left\lfloor \frac{N}{2} \right\rfloor \le k \le \left\lfloor \frac{N}{2} \right\rfloor \text{ and } N=2\times\left\lfloor \frac{|D|\lambda^2 L}{2cT^2} \right\rfloor + 1, \qquad (2.32)$$

where h_k is the taps weight, k is a sub-index indicating the number of the tap, and T is the sampling time interval $T = 1/fs$. The operator $\lfloor x \rfloor$ means the largest integer not exceeding x.

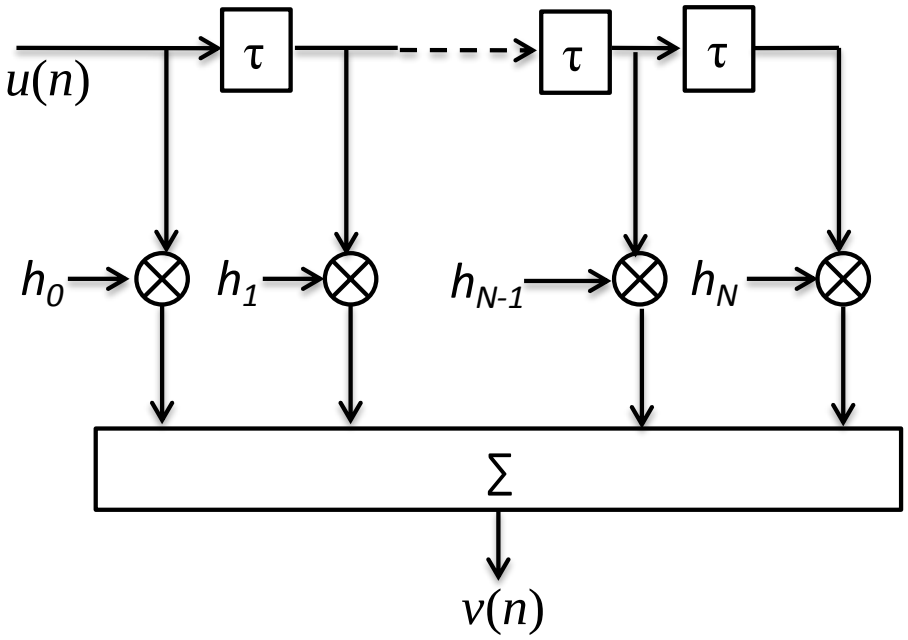

Fig. 2.6: Structure of FIR filter. τ denotes the delay time.

Note that, the infinite-impulse-response (IIR) filter can also be used, where the required numbers of taps are less than those of FIR filters [40]. However, the inherent feedback loop makes this approach almost impossible to implement in high speed applications with parallelized processing.

In case of FDE implementation, the input signal is transformed in the frequency domain, multiplied by filter transfer function as in Eq. (2.31) and then transformed back into the time

domain as shown in Fig. 2.7. Such multiplication in the frequency domain relates to the circular convolution in the time domain; however, we can extract the linearly-convoluted terms from the circularly-convoluted output by using the overlap-save method [41, 42]. Demonstration of such approach can be found in [35].

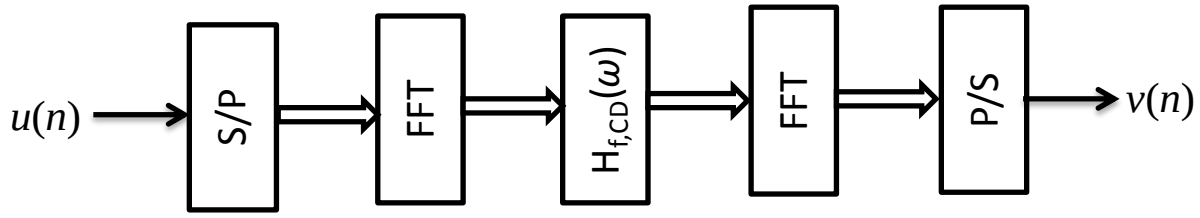

Fig. 2.7: Schematics of frequency-domain fixed equalizer

Adaptive Filtering

In contrast to CD which can be considered as a constant impairment, the polarization related effects are time-varying; thus, polarization state manipulation and PMD compensation should be done adaptively. The problem of compensation for polarization rotation digitally was investigated first by Betti [43] and later demonstrated by utilizing the formalism of the multiple input multiple output (MIMO) system [44, 45]. This is a case of 2x2 MIMO and four filters are connected in the two-by-two butterfly configuration for such purpose as shown in Fig. 2.8.

When the inputs $u_{x,y}$(n) are two-fold oversampled, update of filter tap coefficients $\mathbf{h_p}$(m) is done per every two samples, where $p = xx, xy, yx$ *or* yy and the symbol-spaced sample index m is related to n as $n=2m$ or $2m+1$. The filter outputs are downsampled by a factor of two to retain symbol-spaced output, $v_{x,y}$(m). With such a scenario, apart from equalization of linear impairments, the adaptive filter can perform the polarization demultiplexing [46, 47, 48] and clock recovery [28, 49] simultaneously.

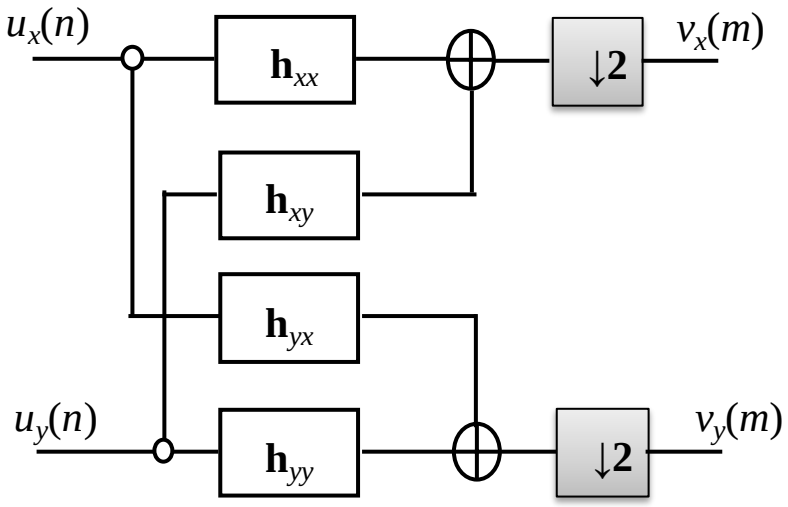

Fig. 2.8: Schematic of two-by-two butterfly structured adaptive FIR filter

Let the polarization-multiplexed signal $\mathbf{U}_{\text{in}}=[u_{in,x}(\text{n})\ u_{in,y}(\text{n})]^{\text{T}}$ is launched on a fiber for transmission, where $u_{in,x}(\text{n})$ and $u_{in,y}(\text{n})$ represent complex amplitudes of the signal electric field in the *x*- and *y*- polarization tributary, respectively. After transmission through fiber, the polarization of the light wave is usually not preserved. In absence of polarization-dependent loss, the output electrical fields at the receiver $u_x(\text{n})$ and $u_y(\text{n})$ can be related to the input electrical fields by

$$\begin{bmatrix} u_x(n) \\ u_y(n) \end{bmatrix} = \mathbf{J} \begin{bmatrix} u_{in,x}(n) \\ u_{in,y}(n) \end{bmatrix} \tag{2.33}$$

where **J** is the unitary matrix representing fiber birefringence. The polarization of light wave in fiber generally drifts with time. However, the rate of this polarization drift is usually slower than the data rate. Therefore, demultiplexing of two polarization tributaries can be done by using four adaptive filters which correspond to four elements of the matrix $\mathbf{J}^{-1}$. The adaptive control of the matrix elements can be done by using decision-directed least-mean-square (DD-LMS) algorithm [50], provided that a training sequence is available. The constant-modulus algorithm (CMA) [51] is also a popular choice for such purpose as it can operate on the blind mode. Details of the filter adaptation algorithms will be discussed in chapter 3.

Usually the received sequence is sampled by free-running analog-to-digital converters (ADCs) operated at the rate twice the symbol rate (*i.e.*, twofold oversampling) because such oversampling significantly reduces the aliasing effect. In this case, the clock recovery can be

performed as follows: First, data sampled by AD converters are interpolated in the time domain. Then, the clock is extracted from the up-sampled data through DFT, and it re-samples the data so as to keep one sample within one symbol interval. The re-sampled data are sent to the DSP circuit for further signal processing including adaptive FIR filters with one-symbol-spaced delay taps. However, we can simplify the DSP circuits by removing such clock-recovery scheme as adaptive FIR filters can also do the same functionality as far as clock frequencies are synchronized between the transmitter and the receiver. This is because during the filter-tap adaptation process, the sampled waveform is continuously time-shifted so that sampling instance for the symbol-spaced sequence comes to the best position in symbol duration. Such function is essentially the clock-recovery process.

Carrier Phase Estimation

The digital phase estimation can use feed-forward (FF) techniques [52, 53] or closed loop concepts [54]. Again, the estimation can be aided by pilot sequences or non-data-aided. The main approach used in modern coherent receivers is based on non-data-aided FF techniques. In this section, only *M*-th power algorithm [55] is discussed which is a popular choice for *M*-ary PSK modulated signals.

Since the linewidth of semiconductor distributed feedback (DFB) lasers varies much more slowly than the phase modulation, it is possible to obtain an accurate phase estimate by averaging the carrier phase over many symbol intervals.

The phase of the complex amplitude obtained from Eq. (2.17) contains both the phase modulation $\theta_s(m)$ and the phase noise $\theta_n(m)$. The procedure to estimate $\theta_n(m)$ is shown in Fig. 2.9. We take the *M*-th power of $v(m)$, because the phase modulation is removed from $v^4(m)$ in the *M*-ary PSK modulation format. Averaging $v^4(m)$ over $2k+1$ samples constitutes a phase estimate as

$$\theta_e(m) = \arg\left(\sum_{n=-k}^{k} v(m+n)^M \right) / M. \tag{2.34}$$

The phase modulation $\theta_s(m)$ is determined by subtracting $\theta(m)$ from the measured phase of $\theta_e(m)$. The phase modulation is then discriminated among *M* symbols.

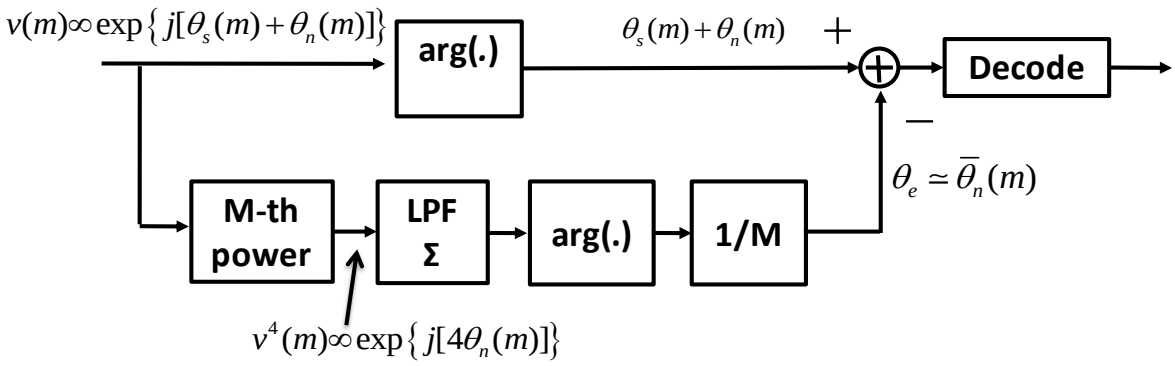

Fig. 2.9: Block diagram of *M*-th power carrier phase recovery scheme

The phase of the symbol thus obtained has the ambiguity of $2\pi/M$, because we cannot know the absolute phase. However, we can avoid the phase-ambiguity problem if the data are differentially precoded, although the bit error rate is doubled by error multiplication.

The phase estimate $\theta_e(m)$ ranges between $-\pi/M$ and $+\pi/M$. Therefore, if $|\theta_e(m)|$ exceeds π/M, the phase jump of $2\pi/M$ occurs as shown in Fig. 2.10. To cope with this problem, the correction for the phase jump is done as follows:

$$\theta_e(m) \leftarrow \theta_e(m) + \frac{2\pi}{M} f\{\theta_e(m) - \theta_e(m-1)\}, \tag{2.35}$$

where $f(x)$ is defined as

$$f(x) = \begin{cases} +1 & \text{for } x < -\pi/M \\ 0 & \text{for } x \le +\pi/M \\ -1 & \text{for } x > +\pi/M \end{cases} \tag{2.36}$$

This adjustment ensures that the phase estimate follows the trajectory of the physical phase and cycle slips are avoided [53].

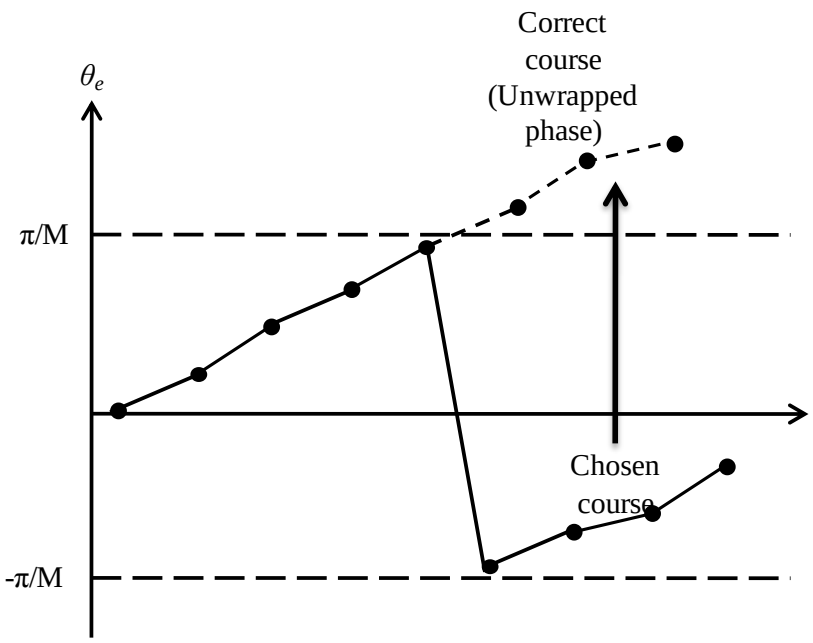

Fig. 2.10: Phase jump and its correction during phase estimation process

As modulation formats move beyond QPSK to high-order QAM, the requirements on the laser linewidth become increasingly stringent [56]. Using conventional wireless approaches such as decision-directed phase locked loops can increase the tolerance range significantly for 16-QAM [6, 54, 57]. Also some other hardware efficient carrier-recovery schemes have been proposed with similar performance [58].

2.3 Chapter Summary

The background of digital coherent optical receivers is reviewed. First, the principle of coherent receivers is discussed. Then, the detailed description of the phase and polarization diversity homodyne receiver with digital signal processing is presented. Finally, explanations of different DSP algorithms used in this thesis are reviewed.

References

1. T. Okoshi and K. Kikuchi, *Coherent Optical Fiber Communications* (Boston, Kluwer Academic Publishers, 1988).
2. J. M. Kahn and K.-P. Ho, "Spectral efficiency limits and modulation/detection techniques for DWDM systems," IEEE J. Sel. Top. Quantum Electron. **10**, 259–272, (2004).
3. K. Kikuchi, *Optical Fiber Telecommunication V B* (Academic press, 2008), Chap. 3.

4. K. Kikuchi, *High Spectral Density Optical Communication Technology*, (Springer, 2010), Chap. 2.
5. M. Seimeitz, *Higher-Order Modulation for Optical Fiber Transmission* (Springer series in opt. science, 2009), Chap. 2, 3.
6. Y. Mori, C. Zhang, K. Igarashi, K., and K. Kikuchi, "Unrepeated 200-km transmission of 40-Gbit/s 16-QAM signals using digital coherent receiver," Opt. Express **17**, 1435-1441 (2009).
7. Y. Mori, C. Zhang, M. Usui, K. Igarashi, K. Katoh, and K. Kikuchi, "200-km transmission of 100-Gbit/s 32-QAM dual-polarization signals using a digital coherent receiver," in *proceedings of European Conference on Optical Communication* (2009), paper 8.4.6.
8. M. Yoshida, H. Goto, K. Kasai, and M. Nakazawa, "64 and 128 coherent QAM optical transmission over 150 km using frequency-stabilized laser and heterodyne PLL detection," Opt. Express **16**, 829-840 (2008).
9. M. Nakazawa, S. Okamoto, T. Omiya, K. Kasai, and M. Yoshida, "256 QAM (64 Gbit/s) coherent optical transmission over 160 km with an optical bandwidth of 5.4 GHz," in *Optical Fiber Communication Conference*, OSA Technical Digest (CD) (Optical Society of America, 2010), paper OMJ5.
10. X. Zhou and J. Yu, "Multi-level, multi-dimensional coding for high-speed and high spectral-efficiency optical transmission," J. Lightwave Technol. **27**, 3641–3653 (2009).
11. M. G. Taylor, "Coherent detection method using DSP for demodulation of signal and subsequent equalization of propagation impairments" IEEE Photon. Technol. Lett. **16**, 674 - 676 (2004).
12. S. J. Savory, A. D. Stewart, S. Wood, G. Gavioli, M. G. Taylor, R. I. Killey, and P. Bayvel, "Digital equalisation of 40Gbit/s per wavelength transmission over 2480km of standard fibre without optical dispersion compensation," in *Proc. European Conference on Optical Communication* (2006), paper Th2.5.5.
13. C. R. S. Fludger, T. Duthel, T. Wuth, and C. Schulien, "Uncompensated transmission of 86Gbit/s polarization multiplexed RZ-QPSK over 100km of NDSF employing coherent equalisation," in *Proc. European Conference on Optical Communication* (2006), paper Th4.3.3.

14. C. R. S. Fludger, T. Duthel, D. van den Borne, C. Schulien, E-D. Schmidt, T. Wuth, E. de Man, G. D. Khoe, and H. de Waardt, "10 x 111 Gbit/s, 50 GHz Spaced, POLMUX-RZ-DQPSK transmission over 2375 km employing coherent equalisation," in *Optical Fiber Communication Conference*, OSA Technical Digest (CD) (Optical Society of America, 2007), paper PDP22.
15. E. M. Ip and J. M. Kahn, "Fiber impairment compensation using coherent detection and digital signal processing," J. Lightwave Technol. **28,** 502-519 (2010).
16. H. Sun, K.-T. Wu, and K. Roberts, "Real-time measurements of a 40 Gb/s coherent system," Opt. Express **16**, 873-879 (2008).
17. L. E. Nelson, S. L. Woodward, S. Foo, X. Zhou, M. D. Feuer, D. Hanson, D. McGhan, H. Sun, M. Moyer, M. O. Sullivan, and P. D. Magill, "Performance of a 46-Gbps dual-polarization QPSK transceiver with real-time coherent equalization over high PMD fiber," J. Lightwave Technol. **27**, 158-167 (2009).
18. K. Roberts, M. O'Sullivan, K. Wu, H. Sun, A. Awadalla, D. J. Krause, and C. Laperle, "Performance of dual-polarization QPSK for optical transport system," J. Lightwave Technol. **27**, 3546-3559 (2009).
19. T. Pfau, S. Hoffmann, R. Peveling, S. Bhandare, S. K. Ibrahim, O.Adamczyk, M. Porrmann, R. Noé, and Y. Achiam, "First real-time data recovery for synchronous QPSK transmission with standard DFB lasers," IEEE Photon. Technol. Lett. **18**, 1907–1909 (2006).
20. A. Leven, N. Kaneda, A. Klein, U.-V. Koc, Y.-K. Chen, and Y.-K., "Real-time implementation of 4.4 Gbit/s QPSK intradyne receiver using field programmable gate array," Electron. Lett. **42**, 1421–1422 (2006).
21. A. Leven, N. Kaneda, and S. Corteselli, "Real-time implementation of digital signal processing for coherent optical digital communication systems," IEEE J. Sel. Topics Quantum Electron. **16**, 1227-1234 (2010).
22. T. Pfau, N. Kaneda, S. Corteselli, A. Leven, and Y. Chen, "Real-time FPGA-based intradyne coherent receiver for 40 Gbit/s polarization-multiplexed 16-QAM," in *Optical Fiber Communication Conference*, OSA Technical Digest (CD) (Optical Society of America, 2011), paper OTuN4.

23. H. Hodgikinson, R. A. Harmon, and D. W. Smith, "Demodulation of optical DPSK using in-phase and quadrature detection," Electron Lett. **21**, 867–868 (1985).
24. F. Derr, "Optical QPSK transmission system with novel digital receiver concept," Electron Lett. **23**, 2177–2179 (1991).
25. B. Glance, "Polarization independent coherent optical receiver," J. Lightwave Technol. **LT-5,** 274–276 (1987).
26. S. Stein and J. Jones, *Modern Communication Principle*, (McGraw-Hill: New York, 1965).
27. S. Stukamoto, Y. Ishikawa, and K. Kikuchi, "Optical homodyne receiver comprising phase and polarization diversities with digital signal processing," in *Proceedings of European Conference on Optical Communication (2006)*, paper Mo4.2.1.
28. K. Kikuchi, "Clock recovering characteristics of adaptive finite-impulse-response filters in digital coherent optical receivers," Opt. Express **19,** 5611-5619 (2011).
29. G. Bosco, A. Carena, V. Curri, P. Poggiolini, and F. Forghieri, "Performance limits of Nyquist-WDM and CO-OFDM in high-speed PM-QPSK systems," IEEE Photon. Technol. Lett. **22**, 1129–1131 (2010).
30. I. Dedic, "56 GS/s ADC: enabling 100GbE," in *Optical Fiber Communication Conference*, OSA Technical Digest (CD) (Optical Society of America, 2010), paper OThT6.
31. V. Curri, P. Poggiolini, A. Carena, and F. Forghieri, "Dispersion compensation and mitigation of nonlinear effects in 111-Gb/s WDM coherent PM-QPSK systems," IEEE Photon. Technol. Lett. **20**, 1473-1475 (2008).
32. C. Xie, "WDM coherent PDM-QPSK systems with and without inline optical dispersion compensation," Opt. Express **17**, 4815-4823 (2009).
33. Seb J. Savory, "Digital filters for coherent optical receivers," Opt. Express **16**, 804-817 (2008).
34. S. Tsukamoto, K. Katoh, and K. Kikuchi, "Unrepeated transmission of 20-Gb/s optical quadrature phase-shift-keying signal over 200-km standard single-mode fiber based on digital processing of homodyne-detected signal for group-velocity dispersion compensation," IEEE Photon. Technol. Lett. **18**, 1016–1018, (2006).

35. R. Kudo, T. Kobayashi, K. Ishihara, Y. Takatori, A. Sano, and Y. Miyamoto, "Coherent optical single carrier transmission using overlap frequency domain equalization for long-haul optical systems," J. Lightwave Technol. **27**, 3721-3718 (2009).
36. M. Kuschnerov, F. N. Hauske, K. Piyawanno, B. Spinnler, M. S. Alfiad, A. Napoli, and B. Lankl, "DSP for coherent single-carrier receivers," J. Lightwave Technol. **27**, 3614–3622, (2009).
37. G. P. Agrawal, *Fiber-optic Communication Systems*, 3rd ed. (Wiley, New York, 2002).
38. M. Kuschnerov, F. N. Hauske, K. Piyawanno, B. Spinnler, A. Napoli, and B. Lankl, "Adaptive chromatic dispersion equalization for non-dispersion managed coherent systems," in *Optical Fiber Communication Conference*, OSA Technical Digest (Optical Society of America, 2009), paper OMT1.
39. F. N. Hauske, Z. Zhang, C. Li, C. Xie, and Q. Xiong, "Precise, robust and least complexity CD estimation," in *Optical Fiber Communication Conference*, OSA Technical Digest (CD) (Optical Society of America, 2011), paper JWA032.
40. G. Goldfarb and G. Li, "Chromatic dispersion compensation using digital IIR filtering with coherent detection," IEEE Photon. Technol. Lett. **19**, 969-971 (2007).
41. J. J. Shynk, "Frequency-domain and multirate adaptive filtering," IEEE Signal Process. Mag. **9**, 14-37 (1992).
42. S. Haykin, *Adaptive Filter Theory*, 3rd ed., (Prentice Hall, 2001).
43. S. Betti, F. Curti, G. De Marchis, and E. Iannone, "A novel multilevel coherent optical system: four quadrature signaling," J. Lightwave Technol. **9**, 514-523 (1991).
44. Y. Han and G. Li, "Coherent optical communication using polarization multiple-input-multiple-output," Opt. Express **13**, 7527-7534 (2005).
45. Seb J. Savory, G. Gavioli, R. I. Killey, and P. Bayvel, "Electronic compensation of chromatic dispersion using a digital coherent receiver," Opt. Express **15**, 2120-2126 (2007).

46. K. Kikuchi, "Polarization-demultiplexing algorithm in the digital coherent receiver," in 2008 Technical Digest of *IEEE/LEOS Summer Topical Meeting* (IEEE/LEOS, 2008), paper MC2.2.
47. K. Kikuchi, "Performance analyses of polarization demultiplexing based on constant-modulus algorithm in digital coherent optical receivers," Opt. Express **19**, 9868-9880 (2011).
48. R. Noé, T. Pfau, M. El-Darawy, and S. Hoffmann, "Electronic polarization control algorithms for coherent optical transmission", IEEE J. Sel. Topics Quantum Electron. **16**, 1993-1200 (2010).
49. G. Ungerboeck, "Fractional tap-spacing equalizer and consequences for clock recovery in data modems," IEEE Trans. Commun. **24**, 856–864 (1976).
50. S. U. H. Qureshi, "Adaptive equalization," Proc. IEEE **73**, 1349–1387 (1985).
51. D. N. Godard, "Self-recovering equalization and carrier tracking in two-dimensional data communication systems," IEEE Trans. Commun. **28**, 1867–1875 (1980).
52. R. Noé, "Phase noise tolerant synchronous QPSK receiver concept with digital I&Q baseband processing," in *Proceedings of Opto-Electronics and Communications Conference* (2004), paper 16C2–5.
53. K. Kikuchi, "Phase-diversity homodyne detection of multilevel optical modulation of with digital carrier phase estimation," IEEE J. Sel. Topics Quantum Electron. **12**, 563-570 (2006).
54. P. J.Winzer, A. H. Gnauck, C. R. Doerr, M. Magarini, and L. L. Buhl, "Spectrally efficient long-haul optical networking using 112-Gb/s polarization-multiplexed 16-QAM," J. Lightwave Technol. **28**, 547-556 (2010).
55. D. -S. Ly-Gagnon, S. Tsukamoto, K. Katoh, and K. Kikuchi, "Coherent detection of optical quadrature phase-shift keying signals with carrier phase estimation," J. Lightwave Technol. **24**, 12-21 (2006).
56. S. Zhang, P. Kam, C. Yu, and J. Chen, "Laser linewidth tolerance of decision-aided maximum likelihood phase estimation in coherent optical *M*-ary PSK and QAM systems," IEEE Photon. Technol. Lett. **21**, 1075–1077 (2009).

57. I. Fatadin, D. Ives, and S. J. Savory, "Blind equalization and carrier phase recovery in a 16-QAM optical coherent system," J. Lightwave Technol. **27**, 3042–3049 (2009).
58. T. Pfau, S. Hoffmann, and R. Noé, "Hardware-efficient coherent digital receiver concept with feedforward carrier recovery for *M* -QAM constellations," J. Lightwave. Technol. **27**, 989–999 (2009).

Chapter 3

Multi-Impairment Monitoring from Adaptive FIR Filters

The digital coherent receiver enables equalization of all deterministic linear impairments by using four finite-impulse-response (FIR) filters structured in a two-by-two butterfly configuration. After the filters are adapted by a suitable algorithm, we can construct a frequency-dependent two-by-two matrix with four elements, which correspond to transfer functions of the adapted four FIR filters. This matrix is nothing but the inverse transfer matrix of the channel and contains combined effects of chromatic dispersion (CD), polarization mode dispersion (PMD) and polarization dependent loss (PDL). The challenge is to develop a precise algorithm for sorting out the individual impairment from this monitoring matrix. We propose a novel and unified algorithm to monitor CD, first- and second- order PMD and PDL from this monitoring matrix. As of second-order PMD, its two components, polarization dependent chromatic dispersion (PCD) and depolarization (DEP) of two principle states of polarization (PSPs), are estimated separately.

This chapter is organized as follows: Sec. 3.1 gives the theoretical background that is necessary to understand the rest of the chapter. Section 3.2 introduces the proposed novel equalization algorithm. Section 3.3 describes the proposed multi-impairment algorithm from the monitoring matrix. Section 3.4 illustrates the experimental verification of both equalization and monitoring algorithms and finally Sec. 3.5 summarizes this chapter.

In the rest of the chapter, vectors and matrices are in boldface letters; superscripts $(\bullet)^*$, $(\bullet)^T$, $(\bullet)^{-1}$, and $(\bullet)^\dagger$ denote complex conjugate, transpose, inverse, and Hermitian transpose, respectively; subscript $(\bullet)_\omega$ is the numerical differentiation with respect to the angular frequency ω; and functions DFT $(\bullet)$, arg $(\bullet)$, and det $(\bullet)$ denote discrete Fourier transform, argument, and determinant, respectively.

3.1 Theoretical Background

3.1.1 Adaptive Equalization Algorithms

Though several algorithms have been investigated for filter adaptation in digital coherent receivers, gradient-decent-based algorithms such as the least-mean-square (LMS) algorithm [1,

2] and the constant-modulus algorithm (CMA) [3, 4] are most popular. In the following, these two algorithms are described.

Let the filter input vectors be given as

$$\mathbf{u}_x(m) = \left[u_x(m) \quad u_x(m-1) \quad \cdots \quad u_x(m-N)\right]^T, \tag{3.1}$$

$$\mathbf{u}_y(m) = \left[u_y(m) \quad u_y(m-1) \quad \cdots \quad u_y(m-N)\right]^T, \tag{3.2}$$

where u_x(m) and u_y(m) denote the m-th sample of the received complex amplitude of the electric field from the x- and y- port of the homodyne receiver comprising phase and polarization diversities, and N is the number of delay taps. The tap coefficient vector is given as

$$\mathbf{h}_p(m) = \left[h_{p,0}(m) \quad h_{p,1}(m) \quad \cdots \quad h_{p,N}(m)\right]^T, \tag{3.3}$$

where, $p = xx, xy, yx$ *or* yy. Then, the outputs from two ports of butterfly configuration are given by

$$v_x(m) = \mathbf{h}_{xx}^T(m)\mathbf{u}_x(m) + \mathbf{h}_{xy}^T(m)\mathbf{u}_y(m), \tag{3.4}$$

$$v_y(m) = \mathbf{h}_{yx}^T(m)\mathbf{u}_x(m) + \mathbf{h}_{yy}^T(m)\mathbf{u}_y(m). \tag{3.5}$$

As derived in *appendix A1*, for the LMS algorithm, the tap weights are updated with a step size parameter μ as

$$\mathbf{h}_{xx}(m+1) = \mathbf{h}_{xx}(m) + \mu e_x(m)\mathbf{u}_x^*(m), \tag{3.6}$$

$$\mathbf{h}_{xy}(m+1) = \mathbf{h}_{xy}(m) + \mu e_x(m)\mathbf{u}_y^*(m), \tag{3.7}$$

$$\mathbf{h}_{yx}(m+1) = \mathbf{h}_{yx}(m) + \mu e_y(m)\mathbf{u}_x^*(m), \tag{3.6}$$

$$\mathbf{h}_{yy}(m+1) = \mathbf{h}_{yy}(m) + \mu e_y(m)\mathbf{u}_y^*(m), \tag{3.7}$$

The error signals, $e_{x,y}(m)$, are given as

$$e_x(m) = d_x(m) - v_x(m), \tag{3.10}$$

$$e_y(m) = d_y(m) - v_y(m), \tag{3.11}$$

where $d_{x,y}(m)$ are the desired symbol which may either the training symbol in the training mode or the decoded symbol in the decision-directed mode.

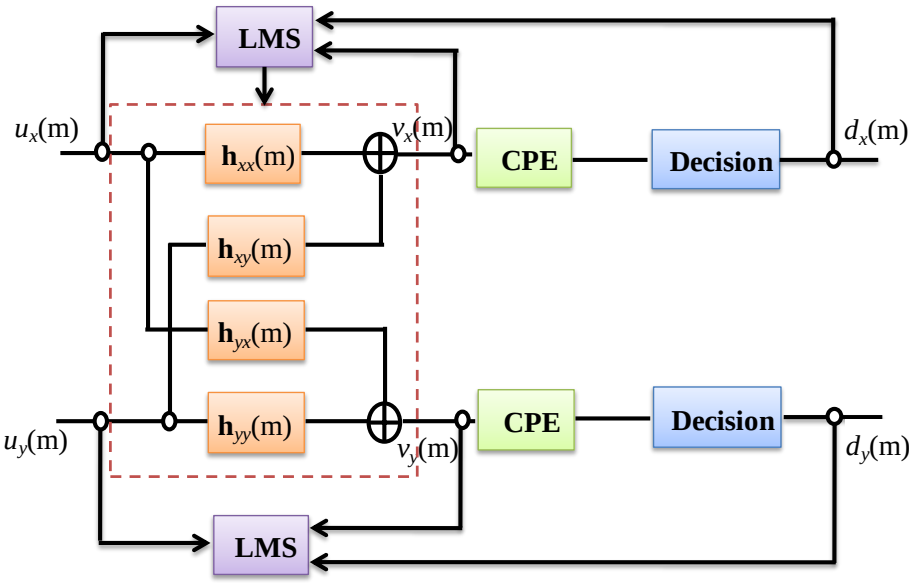

Fig. 3.1: Butterfly structured FIR filters adapted by DD-LMS algorithm

However, in the decision-directed mode, it is necessary to ensure a perfect carrier phase estimation and IF estimation before decision; otherwise, the performance of decision-directed LMS (DD-LMS) can be degraded, especially when numbers of delay taps are large.

On the other hand, such situation can be avoided by using the CMA. In case of the CMA, as shown in *Appendix A2*, the filter tap coefficients are updated as:

$$\mathbf{h}_{xx}(m+1) = \mathbf{h}_{xx}(m) + \mu e_x(m) v_x(m) \mathbf{u}_x^*(m), \tag{3.12}$$

$$\mathbf{h}_{xy}(m+1) = \mathbf{h}_{xy}(m) + \mu e_x(m) v_x(m) \mathbf{u}_y^*(m), \tag{3.13}$$

$$\mathbf{h}_{yx}(m+1) = \mathbf{h}_{yx}(m) + \mu e_y(m) v_y(m) \mathbf{u}_x^*(m), \tag{3.14}$$

$$\mathbf{h}_{yy}(m+1) = \mathbf{h}_{yy}(m) + \mu e_y(m) v_y(m) \mathbf{u}_y^*(m), \tag{3.15}$$

The error signals, $e_{x,y}(m)$, are given as

$$e_x(m) = R_2^2 - |v_x(m)|^2, \tag{3.16}$$

$$e_y(m) = R_2^2 - |v_y(m)|^2, \tag{3.17}$$

where $R_2 = \frac{E\{|d(m)|^4\}}{E\{|d(m)|^2\}}$. Thus, R_2 is generally assumed as 1 for the *M*-ary PSK modulation format. As shown by Eqs. (3.16) and (3.17), CMA cost functions $|e_{x,y}(n)|^2$ are independent of the signal phase. Therefore, unlike DD-LMS, the performance of CMA is inherently independent of the carrier recovery or IF estimation circuits.

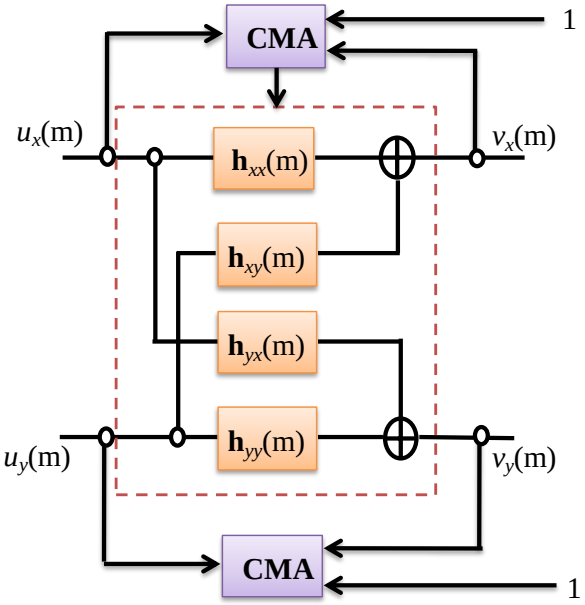

Fig. 3.2: Fig. 3.1: Butterfly structure for FIR filters adapted by the CMA

Note that the CMA is also applicable for non-constant modulus modulation formats such as high-order QAM; however, modifications in Eqs. (3.16) and (3.17) can enhance the performance of CMA for the high-order QAM formats [5, 6, 7]. Such modified CMA is derived from the radius-directed adaptive algorithm proposed for wireless communication [8, 9], in which the error signal, for example in case of 16-QAM, can be calculated as:

1. When $|v_{x,y}(m)|^2 < 0.6$, $e_{x,y}(m) = \left\{0.2 - |v_{x,y}(m)|^2\right\}$.

2. For $0.6 \le |v_{x,y}(m)|^2 \le 1.8$, $e_{x,y}(m) = \left\{1.0 - |v_{x,y}(m)|^2\right\}$.

3. And when $|v_{x,y}(m)|^2 > 1.8$, $e_{x,y}(m) = \left\{1.0 - |v_{x,y}(m)|^2\right\}$.

We consider that the signal power is normalized to one on each polarization.

3.1.2 Singularity Problem of CMA

When we apply the conventional CMA, initial tap coefficients of four filters are set to zeros except for the center tap of each filter which is chosen from the four elements of a two-by-two arbitrary unitary matrix $\mathbf{h_0}$ give as

$$\mathbf{h_0} = \begin{bmatrix} \sqrt{\alpha_0} e^{j\delta_0} & -\sqrt{1-\alpha_0} \\ \sqrt{1-\alpha_0} & \sqrt{\alpha_0} e^{-j\delta_0} \end{bmatrix}. \tag{3.18}$$

In this Eq. (3.18), $0 \le \alpha_0 \le 1$ and $-\pi \le \delta_0 < \pi$. Assume that the unitary matrix $\mathbf{T}$ is the Jones matrix of the fiber for transmission expressing its birefringence property, which can be written as

$$\mathbf{T} = \begin{bmatrix} \sqrt{\alpha} e^{j\delta} & -\sqrt{1-\alpha} \\ \sqrt{1-\alpha} & \sqrt{\alpha} e^{-j\delta} \end{bmatrix}, \tag{3.19}$$

where α denotes the power splitting ratio between two polarization modes and δ the phase difference between them. Then, the initial outputs of two ports of the filters are given as $[v_{x0}, v_{y0}]^T = \mathbf{h_0 T}\ [u_{in,x}\ u_{in,y}]^T$, where $[u_{in,x}\ u_{in,y}]^T$ is the transmitted signal. Since $\mathbf{T}$ and $\mathbf{h_0}$ are unitary, v_{x0} and v_{y0} are orthogonal to each other in the Stokes space. Let v_{x0} and v_{y0} be located in A_0 and B_0 points on the Stokes space. The Stokes parameter S_1 of A_0 is positive in Fig. 3.3(a) while negative in Fig. 3.3(b). B_0 is located at the antipodal point of A_0. Thus, when $S_1>0$ for A_0 as shown in Fig. 3.3(a), A_0 moves towards A (linear x polarization) and B_0 towards B (linear y polarization). On the other hand, when $S_1<0$ for A_0 as shown in Fig 3.3(b), A_0 moves towards B and B_0 towards A. That means though polarization demultiplexing is performed, the corresponding output ports of the butterfly structure have been interchanged.

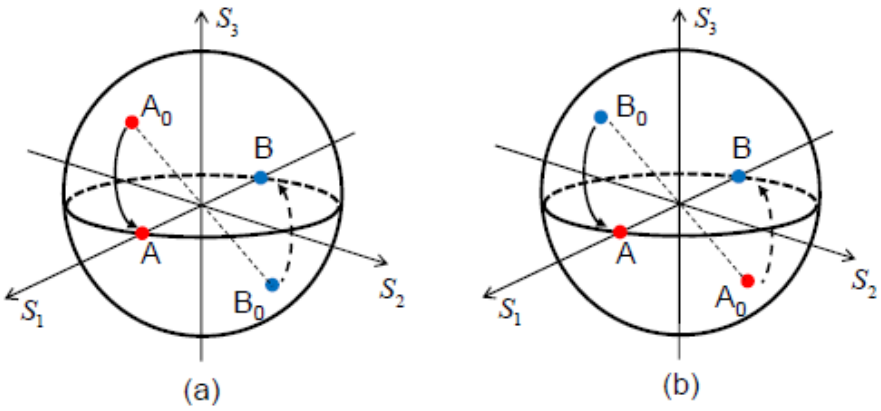

Fig. 3.3: Trajectories of polarization vectors v_{x0} and v_{y0} on the Poincare sphere. (a): $S_1>0$ for A_0 and (b): $S_1<0$ for A_0. After ref. [10].

However, in presence of PDL, the fiber transfer function is no longer a unitary matrix and it is possible to have the same sign of S_1 for both A_0 and B_0. In such case, outputs from both ports converge to same polarization tributary. This situation is termed as the *singularity problem* because the matrix $\mathbf{h_0T}$ becomes a singular matrix. For example, as shown by the polarization trajectories in Fig. 3.4, with -3dB PDL and $\mathbf{h_0}$ is given as

$$\mathbf{h_0} = \begin{bmatrix} 1 & 0 \\ 0 & 1 \end{bmatrix}, \tag{3.20}$$

the S_1 values for both v_{x0} and v_{y0} are positive sign; therefore, both output tributaries converge to *x*-polarization channel and causing the singularity problem.

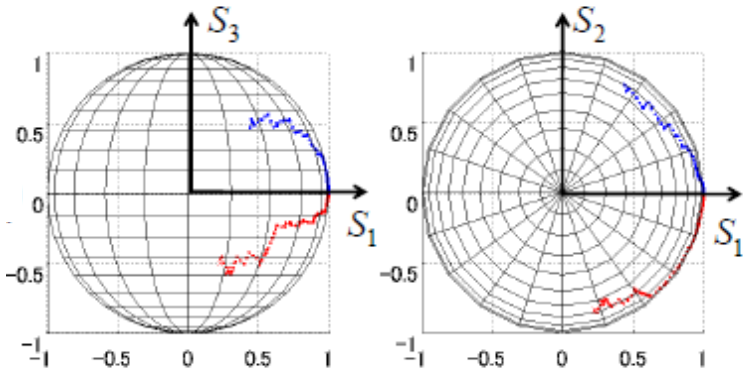

Fig. 3.4: Trajectories of polarization vectors when PDL=-3 dB and $\mathbf{h_0}$ is given as Eq. (3.20). Red and blue colors corresponds to *x*- and *y*- polarization channel. After ref. [10].

3.1.3 Channel Model

Considering a modest channel power to operate in the linear region or weakly nonlinear region, we can model the transfer function of a fiber as a concatenation of CD, PMD and PDL elements, given as $D(\omega)$, $\mathbf{U}(\omega)$ and $\mathbf{K}$, respectively, and the Jones matrix $\mathbf{T}$ including the birefringence of the fiber as

$$\mathbf{H}_{fiber}(\omega) = D(\omega)\mathbf{U}(\omega)\mathbf{KT}. \tag{3.21}$$

In Eq. (3.21), the scalar function $D(\omega)$ is the CD element expressed as

$$D(\omega) = e^{-j\omega^2\beta_2 L/2}, \tag{3.22}$$

where β_2 is the group velocity dispersion (GVD) parameter, ω the angular frequency of the carrier, and L the fiber link length.

The transfer matrix $\mathbf{U}(\omega)$ represents the PMD element. The first-order PMD element $\mathbf{U}(\omega)$ has the form of a unitary matrix given as

$$\mathbf{U}(\omega) = \mathbf{R}_1^{-1} \begin{bmatrix} e^{j\omega\Delta\tau/2} & 0 \\ 0 & e^{-j\omega\Delta\tau/2} \end{bmatrix} \mathbf{R}_1, \tag{3.23}$$

where $\Delta\tau$ is the DGD between two orthogonal principal states of polarization (PSP) and $\mathbf{R_1}$ is a unitary matrix converting two PSP into the *x*- and *y*-polarization.

Although individual PDL elements may randomly distributed over the transmission system, the global PDL can be represented by a single Hermitian matrix **K** [11] as

$$\mathbf{K} = \mathbf{R}_2^{-1} \begin{bmatrix} \sqrt{\Gamma_{\max}} & 0 \\ 0 & \sqrt{\Gamma_{\min}} \end{bmatrix} \mathbf{R}_2, \tag{3.24}$$

where Γ_{max} and Γ_{min} are the maximum and minimum values of the transmission coefficient, respectively, and $\mathbf{R_2}$ is a unitary matrix converting the eigen modes for PDL into the *x*- and *y*-polarization. Finally, **T** is a two-by-two unitary matrix, whose matrix elements are angular-frequency independent as shown in Eq. (3.19).

3.2 CMA with Training Mode

In this work, we use the CMA for filter adaptation. However, as mentioned in the previous section, CMA may suffer from the singularity problem. To cope with this problem several methods have been proposed [10, 12, 13, 14]. In [10], [12] and [13], tap coefficients controlling one tributary are set according to those of the other by assuming that states of polarization (SOP) of two tributaries are orthogonal to each other. However, such orthogonality is not always assured, especially in the presence of high PDL. Moreover, such techniques do not ensure that each polarization tributary will converge to the desire output ports of the butterfly configuration. In [14], a two-stage CMA equalizer has been proposed for singularity-free operation; however, it induces additional complexity of the equalizer. As an alternative of CMA, the independent component analysis (ICA) algorithm has also been investigated for polarization demultiplexing [15, 16, 17]. However, such schemes have much higher computational complexity.

On the other hand, in this work, we propose CMA with the training mode to avoid the singularity problem. In the training mode, the LMS algorithm is used for updating tap coefficients as shown in Eqs. (3.6) - (3.9). The error signals $e_{x,y}(n)$ in Eqs. (3.10) and (3.11) are

calculated using the training signal. After the training mode, the algorithm is switched to the CMA instead of by the commonly used DD-LMS; thus, tap coefficients are updated by Eqs. (3.12) - (3.15) in the blind mode and the error signals are calculated as Eqs. (3.16) and (3.17).

In the proposed method, initial tap coefficients for the CMA are determined by using the training mode such that the output from the *x*-port of the filter corresponds to the *x*-polarization tributary and that from the *y*-port to the *y*-polarization tributary; therefore, we can avoid the singularity problem. On the other hand, switching to CMA, we can apply any high-order FIR filters for equalization because the CMA is inherently phase insensitive.

3.3 Monitoring Algorithm

In dual-polarization transmission systems, the transmitter sends complex amplitudes of both *x*- and *y*-polarized electric fields. While propagating through the fiber, the complex amplitudes suffer from effects of CD, PMD, PDL and birefringence. Then, the complex amplitudes are detected by a phase- and polarization-diverse homodyne receiver that preserves both the amplitude and phase information of the transmitted signal. Next, polarization demultiplexing and equalization can be done in the digital domain by using four complex-valued multi-tap FIR filters arranged in a two-by-two butterfly configuration.

In this point, we consider that the filter delay tap length is long enough compared to the impulse response of the channel. Therefore, after the equalization algorithm is converged, the monitoring matrix $\mathbf{M}(\omega)$ can be constructed by using the discrete Fourier transforms (DFT) of filter-tap coefficients of the four FIR filters in the butterfly configuration as

$$\mathbf{M}(\omega) \approx \mathbf{H}_{fiber}(\omega) = \left\{ \mathrm{DFT} \begin{bmatrix} \mathbf{h}_{xx}(m) & \mathbf{h}_{xy}(m) \\ \mathbf{h}_{yx}(m) & \mathbf{h}_{yy}(m) \end{bmatrix} \right\}^{-1}. \tag{3.25}$$

The matrix $\mathbf{M}(\omega)$ preserves the information of all of the linear impairments. In the following, we propose a simple algorithm, which can separate out CD, DGD, PDL, and second-order PMD, that is, PCD and DEP, through straightforward algebraic manipulations of this monitoring matrix. With such an algorithm, multi-impairment monitoring is finally enabled by the adaptive FIR filters.

While deriving equations in this section, we use the general property of the matrix inversion $(\mathbf{AB})^{-1} = \mathbf{B}^{-1}\mathbf{A}^{-1}$, the property of a unitary matrix $\mathbf{U}^{-1} = \mathbf{U}^{\dagger}$, and the property of a Hermitian matrix $\mathbf{K} = \mathbf{K}^{\dagger}$ without notice.

3.3.1 CD Monitoring

The determinant of the matrix **M**(ω) can be expressed as

$$\det\{\mathbf{M}(\omega)\} = D^2(\omega)\det\{\mathbf{U}(\omega)\}\det(\mathbf{K})\det(\mathbf{T}). \tag{3.26}$$

Since $\det(\mathbf{U}) = 1,\ \det(\mathbf{T}) = 1,$ and $\det(\mathbf{K}) = \sqrt{\Gamma_{\max}\Gamma_{\min}}$, Eq. (3.25) becomes

$$\det\{\mathbf{M}(\omega)\} = D^2(\omega)\sqrt{\Gamma_{max}\Gamma_{min}}. \tag{3.27}$$

Since $\sqrt{\Gamma_{\max}\Gamma_{\min}}$ is a real number, Eqs. (3.22) and (3.27) confirm that the CD value can be estimated by using a quadratic fitting on the unwrapped phase of $\det\{\mathbf{M}(\omega)\}$.

3.3.2 PMD Monitoring

Conventionally, the fiber PMD is characterized by a frequency-dependent PMD vector $\vec{\tau}$ in the three-dimensional Stokes space and can be written as

$$\vec{\tau} = \Delta\tau\,\hat{p}, \tag{3.28}$$

where the unit vector $\hat{p}$ points the direction of the slower PSP.

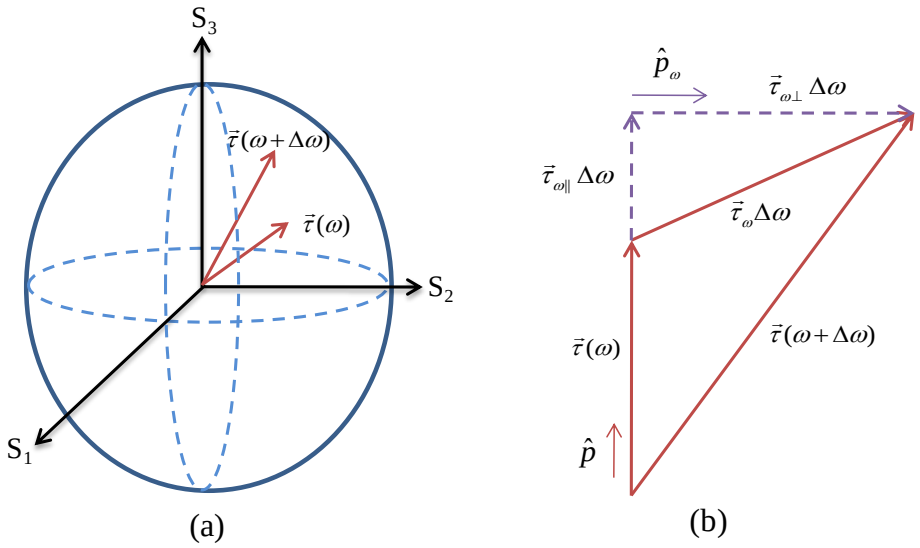

Fig. 3.5: Definition of second-order PMD vector. (a): Two PMD vectors at angular frequencies ω and $\omega+\Delta\omega$ are shown in the Stokes space. (b): Corresponding second-order PMD vector with its perpendicular and parallel components. This is given as the derivative of the first-order PMD vector with respect to the angular frequency ω.

Figure 3.5 (a) shows two PMD vectors $\vec{\tau}(\omega)$ and $\vec{\tau}(\omega+\Delta\omega)$ in the three-dimensional Stokes space, where $\Delta\omega$ is a small change in the angular frequency, usually given as the DFT angular-frequency resolution. Then, the second-order PMD vector $\vec{\tau}_{\omega}$ can be defined as the derivative of $\vec{\tau}$ with respect to ω as shown in Fig. 3.5 (b). The second-order PMD vector can be resolved into two components as

$$\vec{\tau}_{\omega} = \frac{d\vec{\tau}}{d\omega} = \Delta\tau_{\omega}\hat{p} + \Delta\tau\hat{p}_{\omega} : \tag{3.29}$$

One is the DEP component $\vec{\tau}_{\omega\perp} = \Delta\tau\hat{p}_{\omega}$, indicating that the pointing direction of the PMD vector varies with ω. The other is the PCD component $\vec{\tau}_{\omega\parallel} = \Delta\tau_{\omega}\hat{p}$, which represents the change in DGD with ω. As shown in Fig. 3.5(b), the DEP component is perpendicular to $\vec{\tau}(\omega)$, while the PCD component is parallel to $\vec{\tau}(\omega)$.

Consider the matrix $\mathbf{M}(\omega+\Delta\omega)\mathbf{M}^{-1}(\omega)$. Equation (3.26) yields

$$\begin{aligned}\mathbf{M}(\omega+\Delta\omega)\mathbf{M}^{-1}(\omega) &= D(\omega+\Delta\omega)\mathbf{U}(\omega+\Delta\omega)\mathbf{KT}\{D(\omega)\mathbf{U}(\omega)\mathbf{KT}\}^{-1} \\ &= D(\omega+\Delta\omega)D^{*}(\omega)\mathbf{U}(\omega+\Delta\omega)\mathbf{KT}(\mathbf{KT})^{-1}\mathbf{U}^{-1}(\omega) \\ &= c\mathbf{U}(\omega+\Delta\omega)\mathbf{U}^{\dagger}(\omega),\end{aligned} \tag{3.30}$$

where the scalar term $D(\omega+\Delta\omega)D(\omega)^{*}$ is expressed as *c*. Substituting the explicit form of ***U***(ω) given by Eq. (3.23) into Eq. (3.30), we have

$$\begin{aligned}\mathbf{M}(\omega+\Delta\omega)\mathbf{M}^{-1}(\omega) &= c\mathbf{R}_1^{-1}\begin{bmatrix} e^{j(\omega+\Delta\omega)\Delta\tau/2} & 0 \\ 0 & e^{-j(\omega+\Delta\omega)\Delta\tau/2}\end{bmatrix}\mathbf{R}_1\mathbf{R}_1^{-1}\begin{bmatrix} e^{-j\omega\Delta\tau/2} & 0 \\ 0 & e^{j\omega\Delta\tau/2}\end{bmatrix}\mathbf{R}_1 \\ &= c\mathbf{R}_1^{-1}\begin{bmatrix} e^{j\Delta\omega\Delta\tau/2} & 0 \\ 0 & e^{-j\Delta\omega\Delta\tau/2}\end{bmatrix}\mathbf{R}_1.\end{aligned} \tag{3.31}$$

Equation (3.31) shows that eigen values of the matrix $\mathbf{M}(\omega+\Delta\omega)\mathbf{M}^{-1}(\omega)$, $\rho_{1,2}$, are associated with DGD while corresponding eigen vectors, $|t_{1,2}\rangle$, locate the PSPs. The estimation of eigen values and eigen vectors from this matrix enables DGD and second-order PMD monitoring in the following manner.

DGD Monitoring

From Eq. (3.31), it is evident that DGD at ω can be estimated as

$$\Delta\tau = \left|\frac{\arg(\rho_1/\rho_2)}{\Delta\omega}\right|. \tag{3.32}$$

The condition $\Delta\tau\Delta\omega < \pi$ is necessary for avoiding ambiguities that arise from the multi-valued argument function. This condition is generally assured for a wide range of DGD monitoring. For example, for 10-Gsymbol/s transmission, if we use 21-tap *T*/2-spaced equalizer, DGD up to 500-ps can be estimated correctly by using Eq. (3.32). The increased number of taps extends this range further.

Second-order PMD Monitoring

Two DGD values at frequencies $\omega+\Delta\omega$ and ω enable the calculation of PCD by using the following equation:

$$\left|\vec{\tau}_{\omega\|}\right| = \frac{\Delta\tau(\omega+\Delta\omega)-\Delta\tau(\omega)}{\Delta\omega}. \tag{3.33}$$

Let the eigen vector $|t_1\rangle = [s_x, s_y]$ relate to the slower PSP. Then, the corresponding Stokes vector **S** can be calculated as

$$\mathbf{S} = [s_x s_x^* - s_y s_y^*,\ s_x s_y^* + s_x^* s_y,\ j(s_x s_y^* - s_x^* s_y)], \tag{3.34}$$

and the unit vector $\hat{p}$ can be found as $\hat{p} = \mathbf{S}/|\mathbf{S}|$. Thus, unit vectors $\hat{p}(\omega+\Delta\omega)$ and $\hat{p}(\omega)$ enable the estimation of $|\hat{p}_\omega|$ as

$$\left|\hat{p}_\omega\right| = \frac{1}{2}\cdot\frac{\cos^{-1}\{\hat{p}(\omega+\Delta\omega)\cdot\hat{p}(\omega)\}}{\Delta\omega}. \tag{3.35}$$

Eqs. (3.32) and (3.35) yield DEP as

$$\left|\vec{\tau}_{\omega\perp}\right| = \Delta\tau\left|\hat{p}_\omega\right|. \tag{3.36}$$

Finally, the magnitude of the total second-order PMD is determined from

$$\left|\vec{\tau}_\omega\right| = \sqrt{\left|\tau_{\omega\|}\right|^2 + \left|\tau_{\omega\perp}\right|^2}. \tag{3.37}$$

3.3.3 PDL Monitoring

The matrix $\mathbf{M}^{\dagger}(\omega)\mathbf{M}(\omega)$ can be expressed from Eq. (3.25) as

$$\begin{aligned}\mathbf{M}^{\dagger}(\omega)\mathbf{M}(\omega) &= \{D(\omega)\mathbf{U}(\omega)\mathbf{KT}\}^{\dagger}\{D(\omega)\mathbf{U}(\omega)\mathbf{KT}\} \\ &= D^{*}(\omega)D(\omega)\{\mathbf{KT}\}^{\dagger}\mathbf{U}(\omega)^{\dagger}\mathbf{U}(\omega)\{\mathbf{KT}\} \\ &= \mathbf{T}^{\dagger}\mathbf{K}^{\dagger}\mathbf{KT}. \end{aligned} \tag{3.38}$$

Hence, Eq. (3.38) can be rewritten by using Eq. (3.23) as

$$\mathbf{M}^{\dagger}(\omega)\mathbf{M}(\omega) = (\mathbf{TR}_2)^{-1}\begin{bmatrix}\Gamma_{\max} & 0 \\ 0 & \Gamma_{\min}\end{bmatrix}(\mathbf{TR}_2). \tag{3.39}$$

Equation (3.39) shows that eigen values of the matrix $\mathbf{M}^{\dagger}(\omega)\mathbf{M}(\omega)$, $\alpha_{1,2}$, can give PDL in dB as

$$PDL_{dB} = 10\log_{10}\left(\frac{\alpha_1}{\alpha_2}\right). \tag{3.40}$$

3.4 Experimental Verification

3.4.1 Experimental Setup

In order to validate the proposed algorithms, we conducted experiments employing a coherent optical receiver as shown in Fig. 3.6. The transmitter laser was a distributed-feedback laser diode (DFB-LD) having a center wavelength of 1552 nm and a 3-dB linewidth of 150 kHz. The laser for LO had the same characteristics. A NRZ-QPSK signal was generated using a $LiNbO_3$ optical IQ modulator (IQM) from two streams of precoded data from an arbitrary waveform generator (AWG) with 2^9-1 pseudo-random binary sequences (PRBS). Apart from second-order monitoring case, the transmission rate was 40Gbit/s. The dual-polarization signal was then produced in the split-delay-combine manner by using a polarization beam splitter (PBS) and a polarization beam combiner (PBC). The delay length was long enough so that the signals in two polarization tributaries were uncorrelated. The PDL was generated by attenuating one polarization tributary with a variable optical attenuator (VOA). Then, the signal passed through a PMD emulator (PMDE). A commercially available PMDE consisted of three programmable DGD sections separated by polarization controllers as shown in Fig. 3.7 was capable of generating all-order PMD with tunable statistics. A standard single-mode fiber (SMF)

accumulated CD. After the transmitted signal was pre-amplified by an erbium-doped fiber amplifier (EDFA), it was incident on a phase and polarization diverse coherent optical receiver. The received power was controlled by VOA in such a manner that the polarization tributary suffered more from PDL had a BER about 3×10^{-4}. Outputs of the receiver were sampled and digitized at twice the symbol rate with analog-to-digital converters (ADCs), and stored for offline digital signal processing.

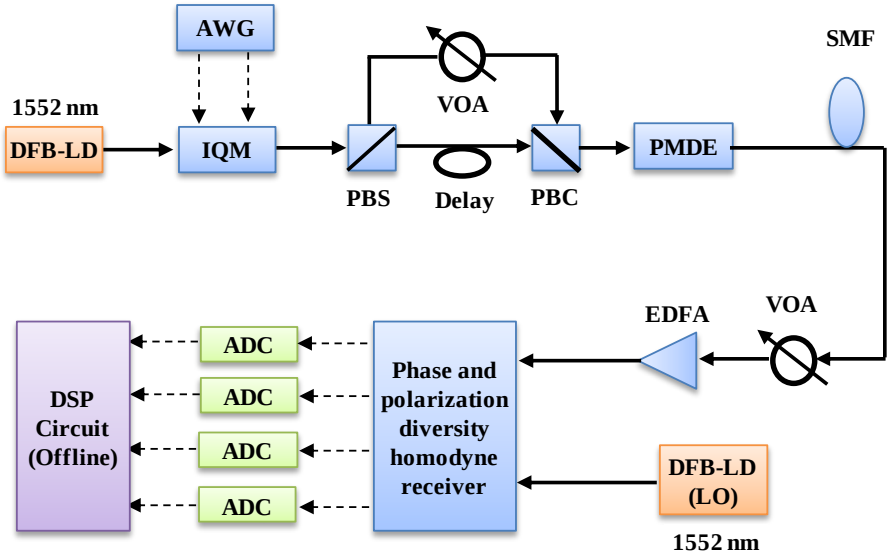

Fig. 3.6: Schematics of the dual-polarization QPSK transmission system for verifications of the proposed impairment-monitoring algorithm.

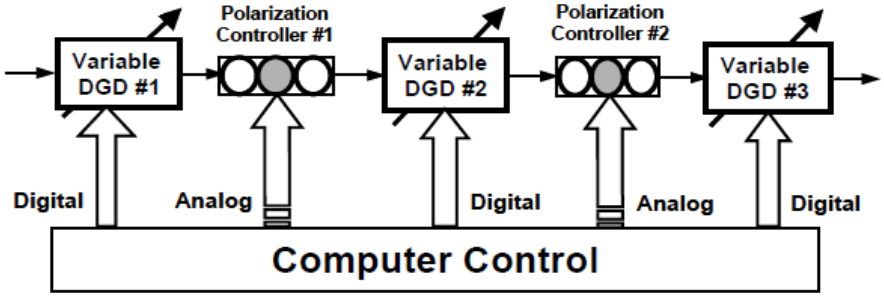

Fig. 3.7: Schematic of all-order PMDE used in the experiment

3.4.2 Results Regarding Singularity Problem

In order to examine the convergence property of the proposed CMA with the training mode, the signals are polarization-demultiplexed and equalized by using four butterfly-structured FIR filters with tap spacing of half-symbol duration. Tap coefficients are adapted by the CMA. The

delay tap length is 21 and the step size is 2^{-9}. Then, carrier recovery is done by the 4-th power algorithm and decoded for BER estimation.

To test the convergence behavior, we need to sweep the state of polarization (SOP) of the incoming signal on the whole Poincaré sphere. Since the convergence property of the algorithm depends on the matrix $\mathbf{h_0T}$, we can sweep either (α_0, δ_0) in Eq. (3.18) or (α, δ) in Eq. (3.19) to examine it. For experimental simplicity, instead of sweeping α and δ in the optical domain, we vary α_0 and δ_0 in the digital domain.

The effect of two-dimensional sweeping of (α_0, δ_0) is shown in Fig. 3.8 in the presence of 20-ps mean DGD and 1,600-ps/nm CD at different PDL values. The region where two outputs converge to the same tributary is marked with the black color, while the white color denotes the region where polarization demultiplexing is done properly. It is found that with increased PDL, the dark region increases for the conventional CMA, whereas there is no dark region for the proposed method, suggesting proper polarization demultiplexing on the entire Poincaré sphere.

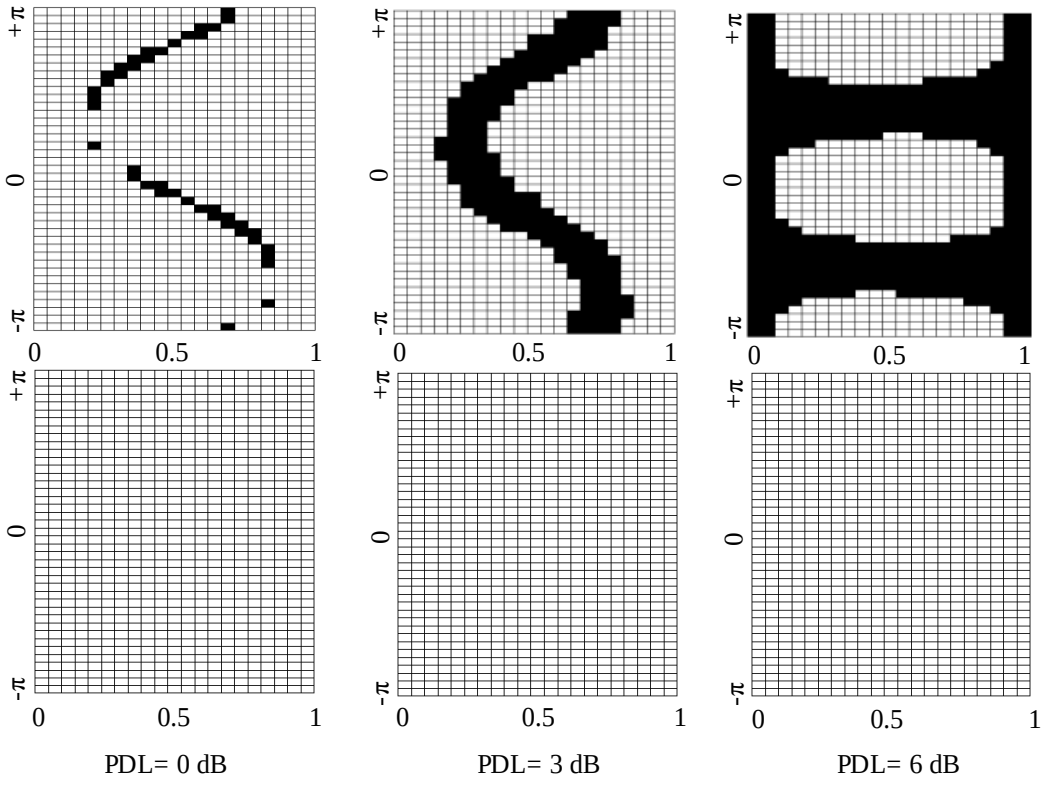

Fig. 3.8: Accuracy of polarization demultiplexing of the conventional CMA (upper) and the proposed method (lower) for different PDL. The horizontal axis represents α_0 and the vertical one does δ_0. In the dark region, the singularity problem occurs.

We also measure the probability of proper polarization demultiplexing for the conventional CMA and the proposed method which is represented as a function of PDL in Fig. 3.9. The proposed method always performs proper polarization demultiplexing, while the probability for the CMA decreases severely with increased PDL.

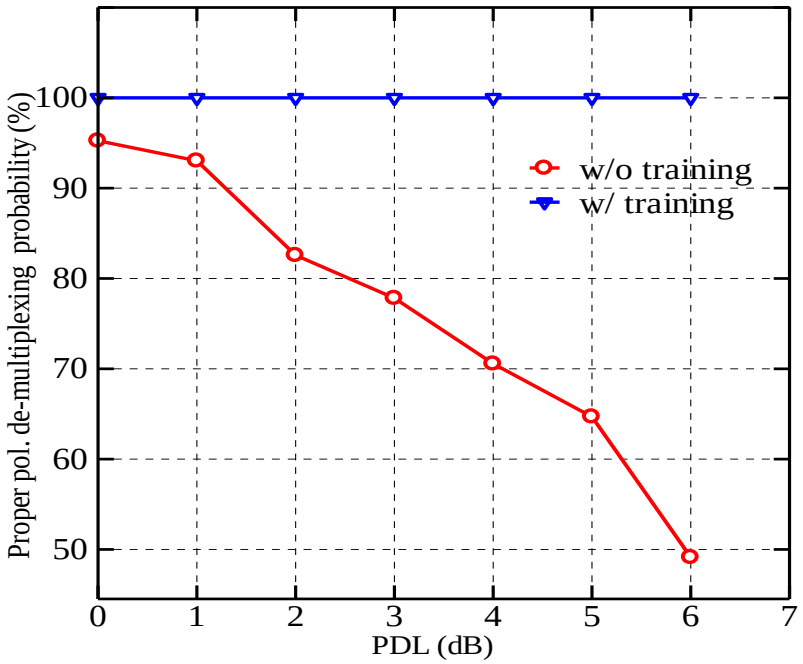

Fig. 3.9: Probability of proper polarization demultiplexing for the conventional CMA and the proposed method measured as a function of PDL.

3.4.3 Results Regarding Monitoring

For multi-impairments monitoring, we first use a T/2-spaced butterfly structured CMA equalizer which simultaneously performs clock-recovery, polarization demultiplexing and equalization. The delay tap length is 61 and the step size parameter is 2^{-10}. Then the tap coefficients are used to form the monitoring matrix, from which each impairment is monitored by using the proposed algorithm. Prior to form the monitoring matrix, we average the filter tap coefficients over several iterations after the convergence to reduce the effect of noise. Moreover, though the spectrum of the transfer function of a *T/2*-spaced filter covers the range from *-B* to *+B* (*B* is the symbol rate), the parameter estimation is concentrated to several center taps only where low-pass electrical filters in the transmitter and the receiver have the linear phase response.

First, to prove the effectiveness of the algorithm for monitoring of CD, DGD and PDL, we

conduct the 40-Gbit/s dual-polarization unrepeated QPSK transmission experiments with the setup shown in Fig. 3.6. Only one DGD section of the PMDE is used to generate a fixed DGD value and also the amount of PDL is set to a constant value.

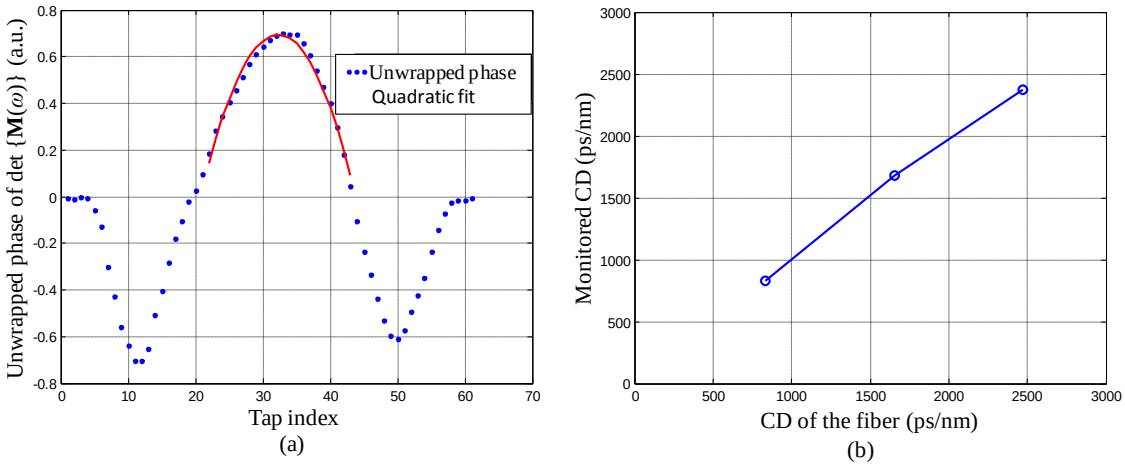

Fig. 3.10: Monitoring results of CD. (a): Estimated unwrapped phase of CD of 1600 ps/nm with 20-ps DGD and 3-dB PDL. (b): CD monitoring result with 20-ps DGD and 3-dB PDL.

Fig. 3.10(a) shows the estimation of the unwrapped phase of det{**M**(ω)}. The CD value then can be estimated using quadratic fitting on this phase. The CD estimation result for 50-km, 100-km and 150-km fiber in presence of 20-ps DGD and 3-dB PDL is shown in Fig. 3.10(b) and the result is in good agreement with values measured by a standard CD measuring instrument that uses the modulation phase shift method.

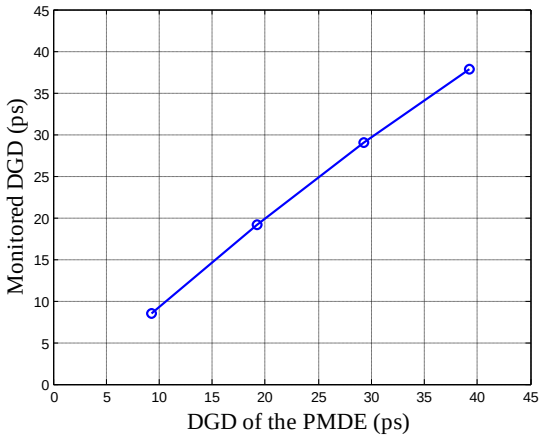

Fig 3.11: DGD monitoring result with 1600-ps/nm CD and 3-dB PDL.

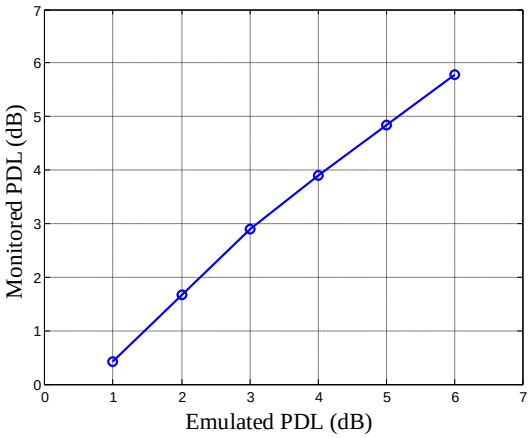

Fig 3.12: PDL monitoring result with 1600-ps/nm CD and 20-ps DGD.

DGD monitoring is done within only 2-ps error up to 40-ps estimation as shown in Fig. 3.11 with 1600-ps/nm CD and 3-dB PDL. Fig. 3.12 shows that PDL estimation results in presence of 1600-ps/nm CD and 20-ps DGD and the estimation is done with a good accuracy up to PDL of 6 dB.

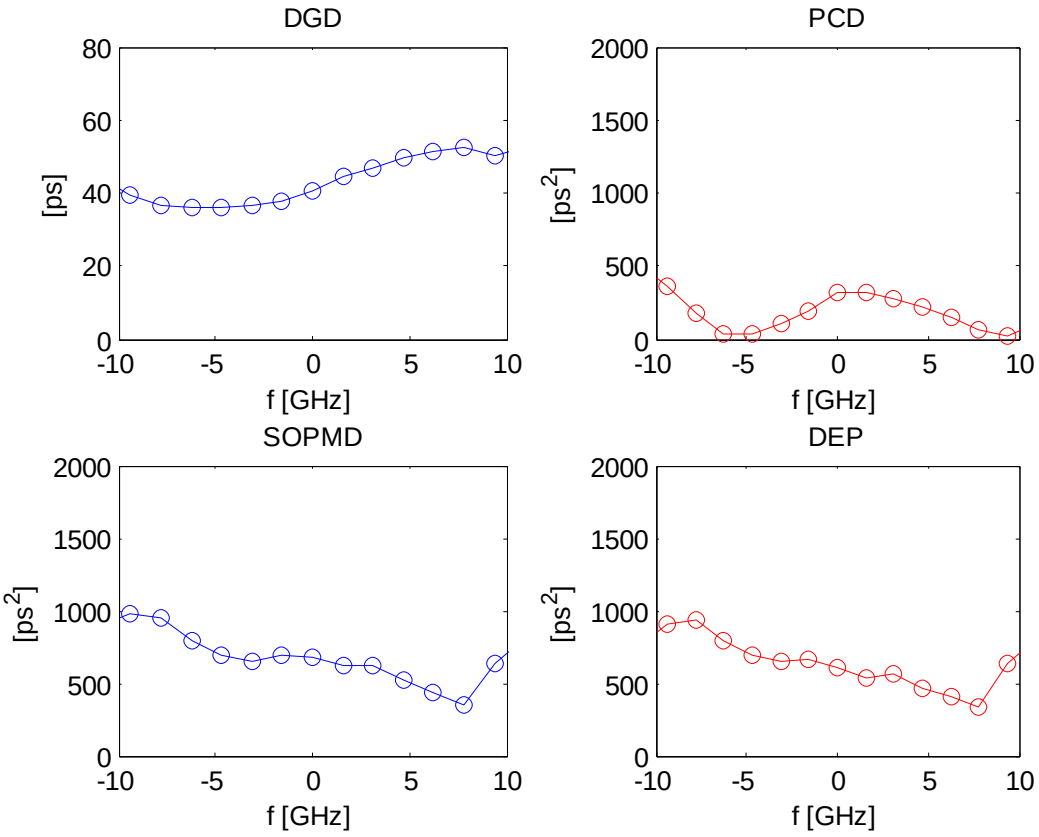

Fig. 3.13: Estimation example of DGD, SOPMD, PCD and DEP from a random sample.

Generation of a fixed and known value of second-order PMD is not available in our PMDE; hence, to verify the second-order PMD monitoring algorithm, the statistical behavior of second-order PMD is estimated and compared with the theoretical model as shown in Table 3.1. The model assumes a constant DGD value and randomly fluctuating birefringence along the fiber. In this experiment, we transmit a 100-Gbit/s dual-polarization QPSK signal through PMDE, which is set to generate a Maxwellian-distributed DGD with the mean value of 35 ps and a corresponding second-order PMD with a refresh rate of 10 ms, while CD and PDL were set to zero. For second-order PMD monitoring case, the filter delay tap length is 33 while the step size is 2^{-10}.

Fig. 3.13 shows an example of the estimation of DGD, second-order PMD and its components for an arbitrary sample. We restrict our estimation to several taps around the center tap for the same reason stated before.

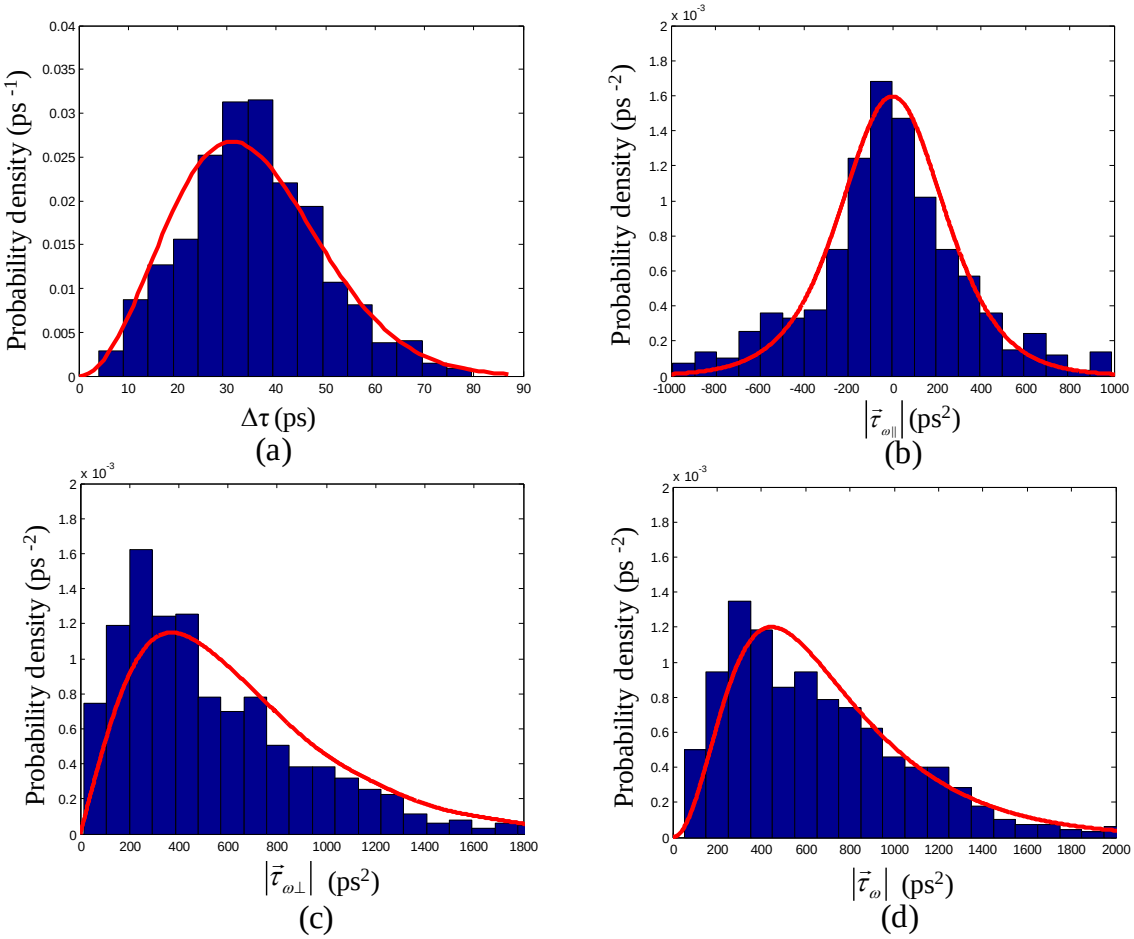

Fig. 3.14: Probability densities of the first- and second-order PMD. (a): DGD $\Delta\tau$, (b): PCD $|\vec{\tau}_{\omega\parallel}|$, (c): DEP $|\vec{\tau}_{\omega\perp}|$, and (d): the magnitude of second-order PMD $|\vec{\tau}_{\omega}|$. Bars show those estimated from monitored values and solid curves are theoretical ones.

We estimate $\Delta\tau$, $|\vec{\tau}_{\omega}|$, $|\vec{\tau}_{\omega\parallel}|$, and $|\vec{\tau}_{\omega\perp}|$ from 700 different experimental data repeatedly taken in three seconds using the proposed algorithm. Estimated probability densities of all of the four parameters are shown by bars in Figs. 3.14 (a)-3.14(d). On the other hand, solid curves in these figures represent theoretical probability densities calculated from the measured mean DGD value based on the theoretical model as shown in Table1.

For all the cases, the measured probability density well matches with the theoretical one. The estimated mean DGD $\Delta\tau$ of 36 ps is very close to the set value of 35 ps, whereas the measured mean second-order PMD value $|\vec{\tau}_\omega|$ is 606 ps^2, which is about 20% less than the theoretical value determined from the estimated mean DGD of 36 ps.

The discrepancy between the estimated second-order PMD and the theoretical prediction may stem from the inadequate number of statistical samples. In addition, three DGD sections in our PMDE may be insufficient to generate the second-order PMD similar to that of the real fiber, which is usually emulated by more than several hundreds of the birefringence section [22].

Table 3.1: Statistical Relations of PMD

Statistic of	**Mean value**	**Density**	**Reference**
DGD ($\Delta\tau$)	$\bar{\tau}$	$p_{\Delta\tau}(x)=\frac{8}{\pi^2\bar{\tau}}\left(\frac{2x}{\bar{\tau}}\right)^2 e^{-(2x/\bar{\tau})^2/\pi}$	[18]
Second-order PMD ($\|\vec{\tau}_\omega\|$)	$2G\bar{\tau}^2/\pi$	$p_{\|\vec{\tau}_\omega\|}(x)=\frac{8}{\pi\bar{\tau}^2}\frac{4x}{\bar{\tau}^2}\tanh\left(\frac{4x}{\bar{\tau}^2}\right)\mathrm{sech}\left(\frac{4x}{\bar{\tau}^2}\right)$	[19]
PCD ($\|\vec{\tau}_{\omega\parallel}\|$)	0	$p_{\|\vec{\tau}_{\omega\parallel}\|}(x)=\frac{2}{\bar{\tau}^2}\mathrm{sech}^2\left(\frac{4x}{\bar{\tau}^2}\right)$	[20]
DEP ($\|\vec{\tau}_{\omega\perp}\|$)	-	$p_{\|\vec{\tau}_{\omega\perp}\|}(x)=x\left(\frac{8}{\pi\bar{\tau}^2}\right)^2\int_0^\infty J_0\left(\frac{8\alpha x}{\pi\bar{\tau}^2}\right)\mathrm{sech}\,\alpha\left(\alpha\tanh\alpha\right)^{1/2}d\alpha$	[21]

$\bar{\tau}$ =mean DGD, J_0=Bessel function of zero-th order, G= Catalan's constant

3.5 Chapter Summary

We have proposed a straightforward algorithm that enables monitoring of linear impairments of a transmission system, such as CD, first- and second- order PMD and PDL, from the equalizer adapted by the CMA. The singularity problem inherent in the CMA is handled by introducing the training mode. We have verified the proposed algorithms with dual-polarization QPSK transmission experiments. Multi-impairment monitoring demonstrated here has the advantage that it can be realized in an efficient way with just a small additional complexity in the DSP circuit of the digital coherent receiver.

References

1. S. Haykin, *Adaptive Filter Theory*, 3rd ed. (Prentice Hall, 2001).
2. J. G. Proakis, Digital Communication, 4th ed. (McGraw-Hill international ed., 2001)
3. D. N. Godard, "Self-recovering equalization and carrier tracking in two-dimensional data communication systems," IEEE Trans. Commun . **COM-28**, 1867–1875 (1980).
4. Seb J. Savory, "Digital filters for coherent optical receivers," Opt. Express **16**, 804-817 (2008)
5. P. J. Winzer and A. H. Gnauck, "112-Gb/s polarization-multiplexed 16-QAM on a 25-GHz WDM grid", in *Proceedings of European Conference on Optical Communication (2008),* paper Th.3.E.5.
6. P. Winzer, A. Gnauck , C. Doerr , M. Magarini, and L. Buhl, "Spectrally efficient long-haul optical networking using 112-Gb/s polarization-multiplexed 16-QAM", J. Lightwave Technol. **28**, 547-556 (2010).
7. R. Noé, T. Pfau, M. El-Darawy, and S. Hoffmann, "Electronic polarization control algorithms for coherent optical transmission", IEEE J. Sel. Topics Quantum Electron. **16**, 1993-1200 (2010).
8. W. Sethares, G. Rey, and J. Johnson C.R., "Approaches to blind equalization of signals with multiple modulus", in *Proceedings of International Conference on Acoustic, Speech, and Signal Processing (1989),* **2**, pp. 972-975.
9. M. Ready and R. Gooch, "Blind equalization based on radius directed adaptation", in *Proceedings of International Conference on Acoustic, Speech, and Signal Processing (1990),* **3**, pp. 1699-1702.
10. K. Kikuchi, "Performance analyses of polarization demultiplexing based on constant-modulus algorithm in digital coherent optical receivers," Opt. Express **19**, 9868-9880 (2011).
11. K. Kikuchi, "Polarization-demultiplexing algorithm in the digital coherent receiver," in *2008 Technical Digest of IEEE/LEOS Summer Topical Meeting (IEEE/LEOS, 2008)*, paper MC2.2.
12. Y. Fukada, "Probability density function of polarization dependent loss (PDL) in optical transmission system composed of passive devices and connecting fibers," J. Lightwave Technol. **20**, 953- (2002).

13. L. Liu, Z. Tao, W. Yan, S. Oda, T. Hoshida, and J. C. Rasmussen, “Initial tap setup of constant modulus algorithm for polarization de-multiplexing in optical coherent receivers,” in *Optical Fiber Communication Conference*, OSA Technical Digest (Optical Society of America, 2009), paper OMT2.
14. C. Xie and S. Chandrasekhar, “Two-stage constant modulus algorithm equalizer for singularity free operation and optical performance monitoring in optical coherent receiver,” in *Optical Fiber Communication Conference*, OSA Technical Digest (Optical Society of America, 2010), paper OMK3.
15. H. Zhang , Z. Tao , L. Liu , S. Oda , T. Hoshida, and J. C. Rasmussen "Polarization demultiplexing based on independent component analysis in optical coherent receivers", in *Proceedings of European Conference on Optical Communication (2008),* Paper Mo.3.D.5.
16. X. Xie, F. Yaman, X. Zhou, and G. Li, "Polarization demultiplexing by independent component analysis," Photon. Technol. Lett. **22**, 805-807 (2010).
17. P. Johannisson, H. Wymeersch, M. Sjödin, A. Serdar Tan, E. Agrell, P. A. Andrekson, and M. Karlsson, "Convergence comparison of the CMA and ICA for blind polarization demultiplexing," J. Opt. Commun. Netw. **3**, 493-501 (2011).
18. C. D. Poole, J. H. Winters, and J. A. Nagel, "Dynamical equation for polarization dispersion," *Opt. Lett.* **16**, 372–374 (1991).
19. G. J. Foschini and C. D. Poole, “Statistical theory of polarization dispersion in single mode fibers,” J. Lightwave Technol. **9**, 1439-1456 (1991).
20. G. J. Foschini, L. E. Nelson, R. M. Jopson, and H. Kogelnik, “Probability densities of second-order polarization mode dispersion including polarization dependent chromatic fiber dispersion,” IEEE Photon. Technol. Lett. **12**, 293-295 (2000).
21. G. J. Foschini, L. E. Nelson, R. M. Jopson and H. Kogelnik, “Statistics of second-order PMD depolarization,” J. Lightwave Technol. **19**, 1882-1886 (2001).
22. L. Yan, X. T. Yao, M. C. Hauer, and A. E. Willner, “Practical solutions to polarization-mode-dispersion emulation and compensation,” J. Lightwave Technol. **24**, 3992-4005 (2006).

Chapter 4

Multi-Impairment Monitoring from Adaptive FDE

One of the key requirements for the multi-impairment monitoring described in the previous chapter is that the finite-impulse-response (FIR) filter delay tap length should be long enough to compensate for all of the linear impairments. However, the computational complexity of FIR filter increases with number of taps and makes it impractical to implement in application-specific integrated circuit (ASIC) or field-programmable gate array (FPGA) [1, 2]. The frequency-domain approach can reduce the computational cost by block-by-block processing and fast implementation of discrete Fourier transform (DFT) [3, 4, 5, 6]. Though adaptive frequency-domain equalizer (FDE) has been investigated for wireless communication systems [7, 8, 9, 10], its applicability to optical communication systems is hardly been demonstrated. Recently several efforts have been made for FDE in optical communication systems; however, they employ either the fixed FDE [11, 12, 13] or need a training sequence for channel estimation [14, 15] which reduces spectral efficiency. Therefore, in this work, we first develop a novel adaptive FDE suitable for digital coherent receivers. Then, we investigate its equalization characteristics and finally, use the FDE tap coefficients for multi-impairment monitoring.

This chapter starts with the background theory related to rest of the chapter. In Sec. 4.2, the proposed novel adaptive FDE is described. In Sec. 4.3, computational complexity of adaptive FDE and time-domain equalizer (TDE) is compared. Section 4.4 explores the multi-impairment monitoring technique from such adaptive FDE. In Sec. 4.5, the experimental verifications of both equalization and monitoring capabilities of the adaptive FDE are presented and finally Sec. 4.6 summarizes the chapter.

Throughout the remainder, time- and frequency-domain variables are denoted by lower- and upper-case characters, respectively, while boldface characters denote vectors. Furthermore, the symbol $*$ represents convolution and $\otimes$ element-by-element multiplication; $\mathbf{O}_{\mathrm{L}}$ is a column vector with L zeros; superscripts $(\bullet)^{e}$ and $(\bullet)^{o}$ correspond to even and odd sub-equalizer parameters, respectively; and conj(•) and $E(\bullet)$ are the conjugate and mathematical expectation operator.

4.1. Background Theory

4.1.1 Linear and Circular Convolution

The linear convolution of two discrete sequences **u**(m) and **h**(m) is given as

$$\mathbf{u}(m) * \mathbf{h}(m) = \sum_{k=-\infty}^{+\infty} \mathbf{u}(k)\mathbf{h}(m-k) = \sum_{k=-\infty}^{+\infty} \mathbf{h}(k)\mathbf{u}(m-k). \tag{4.1}$$

On the other hand, the circular convolution is defined as [16]

$$\mathbf{u}(m) \odot \mathbf{h}(m) = \sum_{k=0}^{N-1} \mathbf{u}(k)\mathbf{h}[(m-k) \bmod N], \tag{4.2}$$

where 'mod' is the modulo operator and N is the period of the periodic signal **u**(m).

For example, let **u**(m)=[2, 1, 2, 2] and **h**(m) =[2, 1, 0.5].

Then, by using Eqs. (4.1) and (4.2), we get

$\mathbf{u}(m) * \mathbf{h}(m) = [4, 4, 6, 6.5, 3, 1]$,

$\mathbf{u}(m) \odot \mathbf{h}(m) = [7, 5, 6, 6.5\ ]$.

The results are shown graphically in Fig. 4.1.

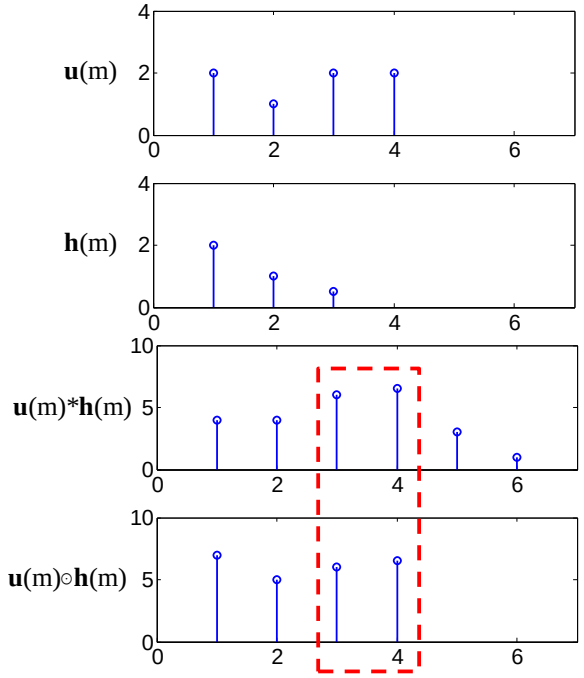

Fig. 4.1: Example of linear and circular convolution

Note that as marked by the dotted line in Fig.4.1, the last part of circularity-convoluted terms is the same as corresponding linearly-convoluted terms.

4.1.2 Efficient Linear Convolution

The filtering of a sequence **u**(m) through a FIR filter of length *N* having the coefficient vector **h**(m) involves linear convolution of **u**(m) and **h**(m). As shown in Eq. (4.1), this process requires *N* multiplications and *N-1* additions for every symbol output. However, when *N* is large, we can obtain linear convolution with a reduced number of multiplications and additions in the frequency domain.

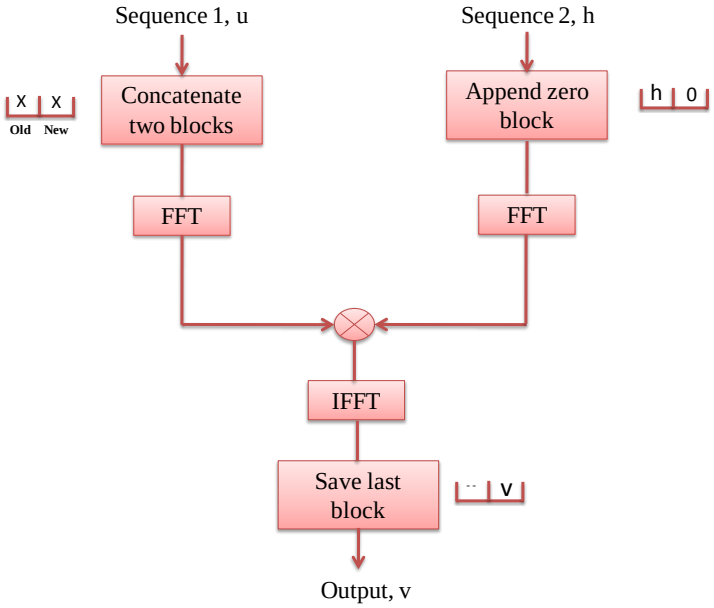

Fig. 4.2: Schematics of overlap-save algorithm

From the properties of DFT, we know that the circular convolution of **h**(m) and **u**(m) can be found by transforming both vectors in the frequency domain by DFT, performing an element-by-element multiplication and transforming the result back in the time domain by inverse DFT (IDFT). This process can be efficiently implemented by the fast Fourier transform (FFT) and the inverse FFT (IFFT) algorithms. Examining the circular convolution example as in Fig. 4.1, it is noted that we can extract the linear convoluted terms from the circular convoluted result.

The commonly used techniques to evaluate linear convolution in the frequency domain are the overlap-save and the overlap-add methods [8]. However, the overlap-add method suffers from more computational complexity compared to the overlap-save method, and hence it will not be pursued further in this work.

For the overlap-save method, as shown in Fig. 4.2, each data block consists of last *N* data points in the previous block followed by the *N* new data points to form a data sequence of *2N*

(this is referred to as 50% overlap). The impulse response of an FIR filter is appended with N zeros and $2N$-point FFT is done.

If the block index k is related to the sample index m as $m=kL+i$ (i=1, 2, 3...), then we can construct the frequency-domain input and the tap-weight vector as

$$\mathbf{U}(k) = FFT\{u(kN-N)\cdots u(kN+N-1)\}, \tag{4.3}$$

$$\mathbf{H}(k) = FFT\{h^T(k), 0, 0\cdots 0\}^T. \tag{4.4}$$

The element-by-element multiplication of $\mathbf{U}(k)$ and $\mathbf{H}(k)$ yields

$$\mathbf{V}(k) = \mathbf{U}(k) \otimes \mathbf{H}(k) \tag{4.5}$$

According to the overlap-save method, N output samples $\mathbf{v}(k) = [v(kN), \cdots v(kN+N-1)]$ from a linear convolution which is calculated as

$$\mathbf{v}(k) = \text{last } N \text{ components of } IFFT\{\mathbf{V}(k)\}. \tag{4.6}$$

4.1.3 Gradient Decent Based Adaptive FDE

Employing the overlap-save method, we can construct the frequency-domain adaptive filter by calculating the gradient vector in the time domain. Such a scheme is shown in Fig. 4.3. If we use the LMS algorithm the error vector can be estimated from the output vector in Eq. (4.6) as

$$\mathbf{e}(k) = \mathbf{d}(k) - \mathbf{v}(k). \tag{4.7}$$

In Eq. (4.7), **d**(k) is the desired symbol block, which may either training signals in the training mode or decoded symbols in the decision-directed mode.

On the other hand, if we use the CMA, the error vector is computed as

$$\mathbf{e}(k) = \left\{R_2^2 - \mathbf{v}(k) \otimes conj(\mathbf{v}(k))\right\} \mathbf{v}(k), \tag{4.8}$$

where, $R_2 = \dfrac{E\{|d(m)|^4\}}{E\{|d(m)|^2\}}$.

Then, the time-domain error vector is transformed to the frequency domain as

$$\mathbf{E}(k) = FFT[\mathbf{O_L}; \mathbf{e}(k)]^T \tag{4.9}$$

After that, the gradient vector in the time domain is computed as

$$\nabla(k) = \text{first } N \text{ components of } IFFT\{\mathbf{U}(k) \otimes \mathbf{H}(k)\}. \tag{4.10}$$

Finally, we need to transform the gradient vector into the frequency domain and add it to **H**(k) in order to generate updated weight **H**(k+1). Since **h**(k) is followed by *N* zeros as in Eq. (4.4), the gradient in Eq. (4.10) must be similarly augmented. Thus, the update equation is given as

$$\mathbf{H}(k+1) = \mathbf{H(k)} + \mu FFT[\nabla^T(k); \mathbf{O}_L]^T. \tag{4.11}$$

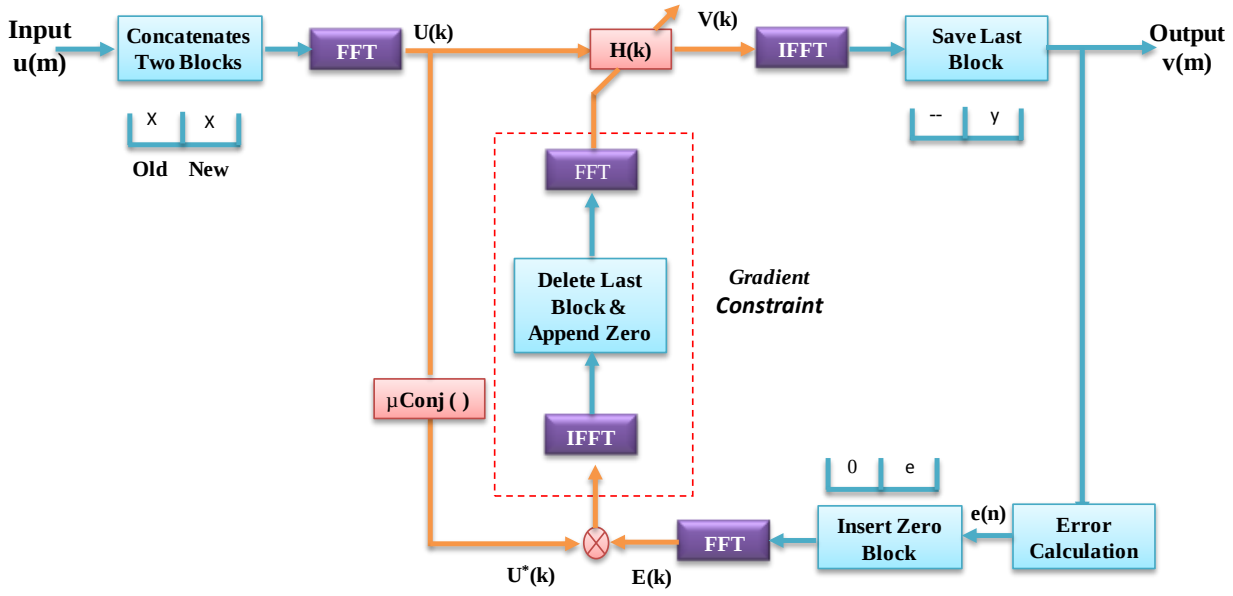

Fig. 4.3: Adaptive FDE using over-save algorithm and gradient decent based updating

Note that, Eqs. (4.10) and (4.11) place a constraint on the gradient vector, as shown by dotted box in Fig. 4.4 and each gradient constraint requires an additional FFT and IFFT; however, it ensures that frequency-domain tap weights are equivalent to the time-domain counterparts. Removing the gradient constraint can reduce the complexity of the equalizer as far as the input sequence satisfies some specific conditions; however, by using such unconstraint FDE algorithm [17], tap-weight vectors do not converge to the Wiener solution as the number of block iterations approaches infinity [18]. Hence, unconstraint FDE is not always reliable.

4.2 Proposal of a Novel Adaptive FDE

The adaptive FDE shown in Fig. 4.3 can operate on the symbol-spaced input sequence only. In such a case, we can construct the gradient vector from each output block, whose length is equal to that of the filter-tap coefficient vector. On the other hand, if we use the twofold-oversampled input sequence and down-sample the output sequence from each output block, we have an

insufficient number of symbol-spaced output samples to construct the gradient vector. However, we need an adaptive FDE that can work on the two-fold oversampled input sequences. The reason behind this is that such oversampling reduces aliasing effects significantly [19] and also the adaptive filter can have the functionality of clock recovery [20].

To overcome the limitation of adaptive FDE shown in Fig. 4.3, we propose a novel adaptive FDE by splitting it into even and odd sub-equalizers where each sub-equalizer operates on symbol-spaced sequences. Thus, the proposed FDE can work on twofold-oversampled input sequences. In the following, we will discuss the adaptive FDE algorithm for the butterfly-structured equalizer configuration.

4.2.1 Equivalence of Half-Symbol-Spaced FIR Filter with Even and Odd Sub-equalizers

We define input ports of the two-by-two butterfly-structured FIR filters as *x* and *y* ports, whereas their output ports as *X* and *Y* ports. The symbol duration is *T*, the delay spacing is *T*/2, and the delay-tap length of each filter is *N*. When $u_x(n)$ and $u_y(n)$ are *n*-th input sequences for *x* and *y* ports, respectively, which are twofold oversampled, the output from the *X* port can be expressed as

$$v_x(n) = \sum_{i=0}^{N-1} h_{xx_i}(n) u_x\left\{(n-i)\frac{T}{2}\right\} + \sum_{i=0}^{N-1} h_{xy_i}(n) u_y\left\{(n-i)\frac{T}{2}\right\}. \tag{4.12}$$

Filter-tap weights are updated every two samples, and the filter output is down-sampled by a factor of two to retain the symbol-spaced output. If we consider that only the odd sequence from the output is taken and used for updating filter-tap weights. Let the new symbol-spaced sample index be *m* such that $n = 2m+1$ (m=0, 1, 2, ⋯); and then, the down-sampled output from the *X* port can be written as

$$\begin{aligned} v_x(m) &= \sum_{i=0}^{N-1} h_{xx_i}(m) u_x\left\{(2m+1-i)\frac{T}{2}\right\} + \sum_{i=0}^{N-1} h_{xy_i}(m) u_y\left\{(2m+1-i)\frac{T}{2}\right\} \\ &= \sum_{i=0}^{N-1} h_{xx_i}(m) u_x\left\{\left(mT - i\frac{T}{2}\right) + \frac{T}{2}\right\} + \sum_{i=0}^{N-1} h_{xy_i}(m) u_y\left\{\left(mT - i\frac{T}{2}\right) + \frac{T}{2}\right\} \end{aligned}$$

$$= \sum_{i=0}^{N/2-1} h_{xx_{2i}}(m)u_x\left\{\left(mT-2i\frac{T}{2}\right)+\frac{T}{2}\right\}+\sum_{i=0}^{N/2-1} h_{xy_{2i}}(m)u_y\left\{\left(mT-2i\frac{T}{2}\right)+\frac{T}{2}\right\}$$

$$+\sum_{i=0}^{N/2-1} h_{xx_{2i+1}}(m)u_x\left\{\left(mT-(2i+1)\frac{T}{2}\right)+\frac{T}{2}\right\}+\sum_{i=0}^{N/2-1} h_{xy_{2i+1}}(m)u_y\left\{\left(mT-(2i+1)\frac{T}{2}\right)+\frac{T}{2}\right\}$$

$$= \sum_{i=0}^{N/2-1} h_{xx_{2i}}(m)u_x\left\{(m-i)T+\frac{T}{2}\right\}+\sum_{i=0}^{N/2-1} h_{xy_{2i}}(m)u_y\left\{(m-i)T+\frac{T}{2}\right\}$$

$$+\sum_{i=0}^{N/2-1} h_{xx_{2i+1}}(m)u_x\left\{(m-i)T+T\right\}+\sum_{i=0}^{N/2-1} h_{xy_{2i+1}}(m)u_y\left\{(m-i)T+T\right\}. \quad (4.13)$$

For the sake of derivational simplicity, we consider that N is even so that $L = N/2$ is an integer. Equation (4.13) shows that the down-sampled output is the sum of two symbol-spaced convolutions with a relative delay of $T/2$. Thus, Eq. (4.13) can be rewritten as

$$v_x(m) = \mathbf{h}_{xx}^e(m) * \mathbf{u}_x^e(m) + \mathbf{h}_{xy}^e(m) * \mathbf{u}_y^e(m) + \mathbf{h}_{xx}^o(m) * \mathbf{u}_x^o(m) + \mathbf{h}_{xy}^o(m) * \mathbf{u}_y^o(m), \quad (4.14)$$

and similarly, the output from the Y port can be written as

$$v_y(m) = \mathbf{h}_{yx}^e(m) * \mathbf{u}_x^e(m) + \mathbf{h}_{yy}^e(m) * \mathbf{u}_y^e(m) + \mathbf{h}_{yx}^o(m) * \mathbf{u}_x^o(m) + \mathbf{h}_{yy}^o(m) * \mathbf{u}_y^o(m), \quad (4.15)$$

where $\mathbf{u}_{x,y}^e(m)$ and $\mathbf{u}_{x,y}^o(m)$ are given as

$$\mathbf{u}_{x,y}^e(m) = [u_{x,y}(2m), u_{x,y}(2m-2), u_{x,y}(2m-4), \cdots, u_{x,y}(2m-2L)]^{\mathrm{T}}, \quad (4.16)$$

$$\mathbf{u}_{x,y}^o(m) = [u_{x,y}(2m+1), u_{x,y}(2m-1), u_{x,y}(2m-3), \cdots, u_{x,y}(2m-2L+1)]^{\mathrm{T}}. \quad (4.17)$$

On the other hand, filter-tap coefficient vectors $\mathbf{h}_{pq}^{e,o}(m)$ are given as

$$\mathbf{h}_p^e(m) = [h_{p_0}(m), h_{p_2}(m), \cdots h_{p_{2L-2}}(m)]^{\mathrm{T}}, \quad (4.18)$$

$$\mathbf{h}_p^o(m) = [h_{p_1}(m), h_{p_3}(m), \cdots h_{p_{2L-1}}(m)]^{\mathrm{T}}, \quad (4.19)$$

where p = *xx*, *xy*, *yx* or *yy*. Thus, the equalizer can be split into even and odd sub-equalizers with tap coefficients taken from even and odd filter-tap indices. Correspondingly, the input sequences for the sub-equalizers are taken from even and odd samples of twofold-oversampled sequences.

Eventually, instead of updating tap coefficients of conventional *T*/2-spaced FIR filters every two samples, we can use even and odd sub-equalizers, where tap updating is done every symbol without down-sampling output sequences.

With such sub-equalizer-based FDE, we can efficiently execute time-domain convolutions shown in Eqs. (4.14) and (4.15) in the frequency domain by using DFT and multiplications. Block-output vectors with *L* rows are given as

$$\mathbf{V}_x(k) = \mathbf{H}_{xx}^e(k) \otimes \mathbf{U}_x^e(k) + \mathbf{H}_{xx}^o(k) \otimes \mathbf{U}_x^o(k) + \mathbf{H}_{xy}^e(k) \otimes \mathbf{U}_y^e(k) + \mathbf{H}_{xy}^o(k) \otimes \mathbf{U}_y^o(k) \ , \quad (4.20)$$

$$\mathbf{V}_y(k) = \mathbf{H}_{yx}^e(k) \otimes \mathbf{U}_x^e(k) + \mathbf{H}_{yx}^o(k) \otimes \mathbf{U}_x^o(k) + \mathbf{H}_{yy}^e(k) \otimes \mathbf{U}_y^e(k) + \mathbf{H}_{yy}^o(k) \otimes \mathbf{U}_y^o(k), \quad (4.21)$$

Note that the convolutions in Eqs. (4.14) and (4.15) are linear convolutions, while inverse DFT (IDFT) of Eqs. (4.20) and (4.21) gives us circular convolutions. However, using the overlap-save method, we can extract linearly-convoluted terms from the circularly-convoluted terms obtained from IDFT of Eqs. (4.20) and (4.21) [15].

4.2.2 Configuration of Proposed Adaptive FDE

The schematic of the proposed adaptive FDE for polarization-multiplexed transmission systems is shown in Fig. 4.4, which is implemented by using Eqs. (4.20) and (4.21). Eight frequency-domain filters consist of even sub-equalizers and odd sub-equalizers. Four even sub-equalizers $\mathbf{H}_{xx}^e(k), \mathbf{H}_{xy}^e(k), \mathbf{H}_{yx}^e(k),$ and $\mathbf{H}_{yy}^e(k)$ are connected in a two-by-two butterfly configuration. In the same way, four odd sub-equalizers $\mathbf{H}_{xx}^o(k)$, $\mathbf{H}_{xy}^o(k)$, $\mathbf{H}_{yx}^o(k)$, and $\mathbf{H}_{yy}^o(k)$ are placed in another two-by-two butterfly configuration.

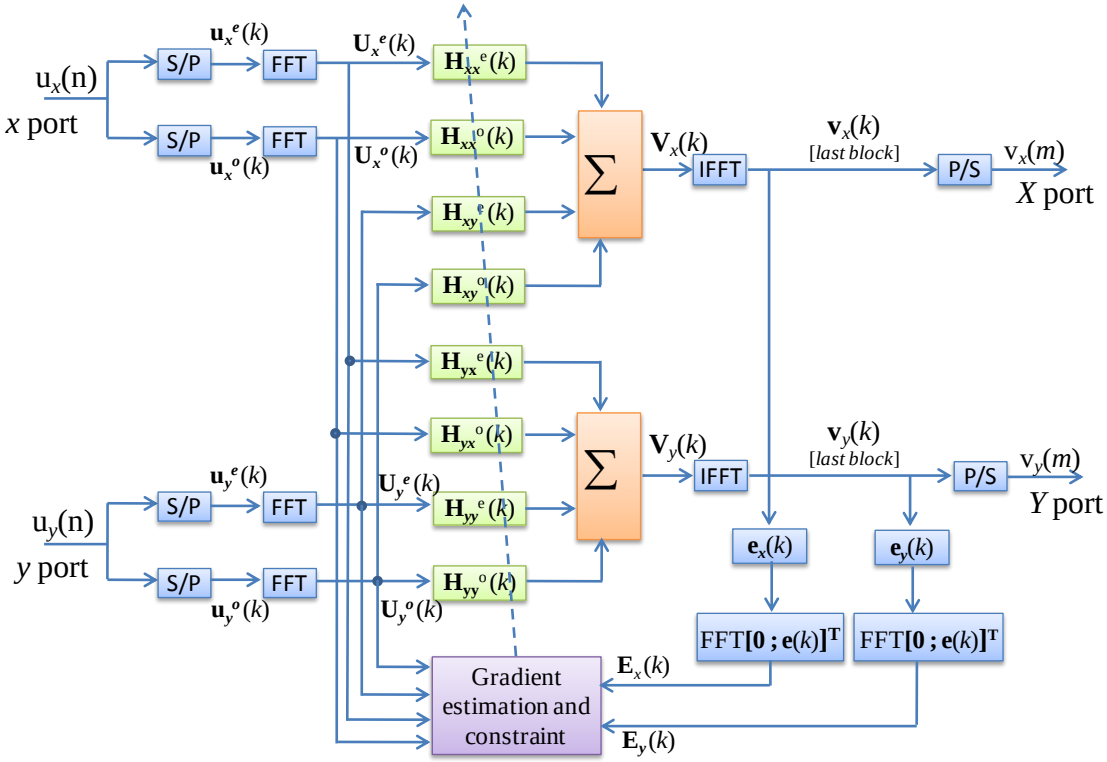

Fig.4.4: Schematic of the proposed adaptive FDE. S/P denotes a serial-to-parallel converter and P/S a parallel-to-serial converter.

First, the input sequences $u_{x,y}(n)$ are divided into even and odd sequences. In the FDE, a block of data is processed at a time instead of sample-by-sample processing in the time-domain. Let the length of even and odd sequences included in a block be L. Then, $\mathbf{u}_{x,y}^{e,o}(k)$ represents a column vector with the length of L for the k-th block.

We choose 50% overlap because the most efficient implementation can be achieved with such an overlapping factor [18]. By using the 50% overlapping factor, the frequency-domain input vector $\mathbf{U}_{x,y}^{e,o}(k)$ for sub-equalizers includes L samples from the current block and L samples from the previous block and can be written as

$$\mathbf{U}_{x,y}^{e,o}(k) = \mathrm{FFT}[u_{x,y}^{e,o}(kL-L), \cdots, u_{x,y}^{e,o}(kL+L-1)]^{\mathrm{T}}, \tag{4.22}$$

Then, L tap weights of the sub-equalizers are padded with the equal number of zeros and $2L$-point FFT is executed. Let $\mathbf{H}_p^{e,o}(k)$ be the FFT-coefficient vector of the zero-padded tap-weight vector $\mathbf{h}_p^{e,o}(k)$ as

$$\mathbf{H}_p^{e,o}(k) = \mathrm{FFT}[\mathbf{h}_p^{e,o}(k); \mathbf{O}_L]^{\mathrm{T}}. \quad (4.23)$$

where $p = xx$, xy, yx or yy. By carrying out IFFT, the output vector in the time domain with a column length of L is given as

$$\mathbf{v}_{x,y}(k) = \text{last } L \text{ elements of IFFT}\{\mathbf{V}_{x,y}(k)\}, \quad (4.24)$$

where $\mathbf{V}_x(k)$ and $\mathbf{V}_y(k)$ are given as Eqs. (4.20) and (4.21), and the first L elements of IFFT$\{\mathbf{V}_{x,y}(k)\}$ are discarded to implement the linear convolution. Then, the error vector in the CMA with a column length of L is calculated in the time domain as

$$\mathbf{e}_{x,y}(k) = [R_2^2 - \mathbf{v}_{x,y}(k) \otimes \mathrm{conj}\{\mathbf{v}_{x,y}(k)\}] \otimes \mathbf{v}_{x,y}(k), \quad (4.25)$$

After augmenting $\mathbf{e}_{x,y}(k)$ with L zeros, we convert it to the frequency-domain vector with the column length of $2L$ as

$$\mathbf{E}_{x,y}(k) = \mathrm{FFT}[\mathbf{O}_L; \mathbf{e}_{x,y}(k)]^{\mathrm{T}}. \quad (4.26)$$

Applying the overlap-save method, we calculate the gradient vector $\nabla_p^{e,o}(k)$ as

$$\nabla_{xx}^{e,o}(k) = \text{first } L \text{ terms of IFFT}[\mathbf{E}_x \otimes \mathrm{conj}\{\mathbf{U}_x^{e,o}(k)\}]^{\mathrm{T}}, \quad (4.27)$$

$$\nabla_{xy}^{e,o}(k) = \text{first } L \text{ terms of IFFT}[\mathbf{E}_x \otimes \mathrm{conj}\{\mathbf{U}_y^{e,o}(k)\}]^{\mathrm{T}}, \quad (4.28)$$

$$\nabla_{yx}^{e,o}(k) = \text{first } L \text{ terms of IFFT}[\mathbf{E}_y \otimes \mathrm{conj}\{\mathbf{U}_x^{e,o}(k)\}]^{\mathrm{T}}, \quad (4.29)$$

$$\nabla_{yy}^{e,o}(k) = \text{first } L \text{ terms of IFFT}[\mathbf{E}_y \otimes \mathrm{conj}\{\mathbf{U}_y^{e,o}(k)\}]^{\mathrm{T}}. \quad (4.30)$$

Finally, the tap weights are updated in the frequency domain by using the gradient decent algorithm as

$$\mathbf{H}_{xx}^{e,o}(k+1) = \mathbf{H}_{xx}^{e,o}(k) + \mu \mathrm{FFT}[\nabla_{xx}^{e,o}(k); \mathbf{O}_L]^{\mathrm{T}}, \tag{4.31}$$

$$\mathbf{H}_{xy}^{e,o}(k+1) = \mathbf{H}_{xy}^{e,o}(k) + \mu \mathrm{FFT}[\nabla_{xy}^{e,o}(k); \mathbf{O}_L]^{\mathrm{T}}, \tag{4.32}$$

$$\mathbf{H}_{yx}^{e,o}(k+1) = \mathbf{H}_{yx}^{e,o}(k) + \mu \mathrm{FFT}[\nabla_{yx}^{e,o}(k); \mathbf{O}_L]^{\mathrm{T}}, \tag{4.33}$$

$$\mathbf{H}_{yy}^{e,o}(k+1) = \mathbf{H}_{yy}^{e,o}(k) + \mu \mathrm{FFT}[\nabla_{yy}^{e,o}(k); \mathbf{O}_L]^{\mathrm{T}}. \tag{4.34}$$

4.3 Computational Complexity Analysis

When we consider power consumption and chip space for implementation of the digital signal processing (DSP) algorithm in ASIC or FPGA, the cost for a multiplier is much higher than that for an adder. Hence, in this section, computational complexity is evaluated in terms of the required number of complex multiplications per bit. In the following, the term 'multiplication' always refers to 'complex multiplication'.

First, we consider the TDE using the butterfly-structured FIR filters adapted by CMA. The delay spacing is *T/2* and the tap length is *N*. To obtain one output symbol from the *X* port and one output symbol from the *Y* port of the TDE, we need 8*N* multiplications for output calculations, 4*N* multiplications for tap updating by CMA, and additional 4 multiplications for error-value calculations. By putting these together, the computational complexity C_{TDE} of the adaptive TDE can be expressed as

$$C_{\mathrm{TDE}} = \frac{6N+2}{\log_2(M)}, \tag{4.35}$$

where *M* is the number of constellation points on the signal constellation.

On the other hand, to obtain *N*/2 output symbols from the *X* port and *N*/2 output symbols from the *Y* port through processing of one block in our proposed FDE, we need *4N* multiplications for output calculations of one block, *4N* multiplications for tap updating by CMA, *2N* multiplications for error-value calculations, and $12N\log_2(N)$ multiplications for 24 FFT/IFFT which include 4 FFT for inputs, 2 IFFT for outputs, 2 FFT for error- vector calculations, and 16

FFT/IFFT for employing gradient constraint of eight sub-equalizers. For FFT implementation, the classical radix-2 algorithm is used, which requires $N\log_2(N)/2$ multiplications to execute FFT of N complex numbers [21]. Thus, the computational complexity C_{FDE} of the proposed FDE can be expressed as

$$C_{\text{FDE}} = \frac{12\log_2(N)+10}{\log_2(M)}. \tag{4.36}$$

Figure 4.5 shows the comparison of computational complexity between FDE and TDE, where we assume the QPSK modulation format (M=4). It is found that the complexity of TDE increases sharply (linearly), while that of FDE increases slowly (logarithmically) with increase in the number of taps.

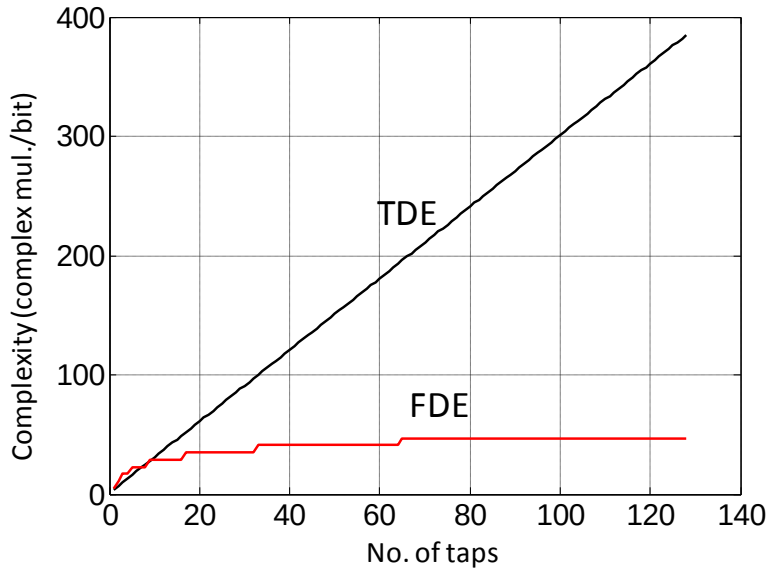

Fig. 4.5: Computational complexity for QPSK modulation format of proposed adaptive FDE and conventional adaptive TDE adapted by CMA

From Table 4.1, it is clear that the proposed adaptive FDE provides much lower complexity than the adaptive TDE when N is 16 or more. This benefit enhances significantly with the increased number of N.

Table 4.1: Computational Complexity of The Proposed FDE and The Conventional TDE Using FIR Filters Adapted by CMA When Use The Dual-Polarization QPSK Modulation Format

N	**4**	**8**	**16**	**32**	**64**	**128**
C_{TDE}	13	25	49	97	193	385
C_{FDE}	17	23	29	35	41	47

4.4 Multi-Impairment Monitoring from Proposed FDE

After the adaptive FDE converge, we perform IFFT to get the impulse response of eight sub-equalizer as in Fig. 4.5 as

$$\mathbf{h}_p^{e,o}(k) = IFFT\{\mathbf{H}_p^{e,o}(k)\}. \tag{4.37}$$

From these sub-equalizers impulse responses, we can construct four impulse responses vectors as

$$\mathbf{h}_p(k) = [h_{p,0}^e(k), h_{p,0}^o(k), h_{p,1}^e(k), h_{p,1}^o(k) \cdots h_{p,L-1}^e(k), h_{p,L-1}^o(k)]^T \tag{4.38}$$

From Eq. (4.38), the monitoring matrix is calculated which is essentially the same as in Eq. (3.25)

$$\mathbf{M}(\omega) = \left\{ DFT \begin{bmatrix} \mathbf{h}_{xx}(k) & \mathbf{h}_{xy}(k) \\ \mathbf{h}_{yx}(k) & \mathbf{h}_{yy}(k) \end{bmatrix} \right\}^{-1}. \tag{4.39}$$

Once the monitoring matrix is formed, multi-impairment monitoring can be performed following the proposed algorithm in Chapter 3.

4.5 Experimental Results and Discussions

To verify the equalization characteristics of the proposed algorithm and the monitoring performance from the adaptive FDE, we conduct the 40-Gbit/s dual polarization QPSK experiments with the same experimental set up shown in Fig 3.5 in Chapter 3. In the DSP circuit, sampling-phase adjustment, polarization demultiplexing, and signal equalization are done simultaneously either by the proposed FDE or by the conventional TDE, where CMA adapted filter-tap weights. In both cases, the singularity problem inherent in CMA is handled by introducing the training mode prior to the blind CMA mode described in Chapter 3. The delay-tap length for the TDE is N=32 and the block length of each sub-equalizer for the FDE is N/2=16.

The step-size parameter is 2^{-10}. After the convergence, filter tap coefficients are used for monitoring. Then, the carrier recovery is done by the 4-th power algorithm [22] and the symbols are decoded to estimate the BER.

4.5.1 Results Regarding Equalization

To evaluate the performance of the proposed algorithm, we set a mixed channel distortion of 1600-ps/nm CD, 20-ps DGD and 3-dB PDL and measure the BER characteristics.

As shown in Fig. 4.6, the BER performance is the same between the proposed adaptive FDE and conventional TDE; however, lower computational complexity can be achieved when the FDE is employed as illustrated in Sec.3

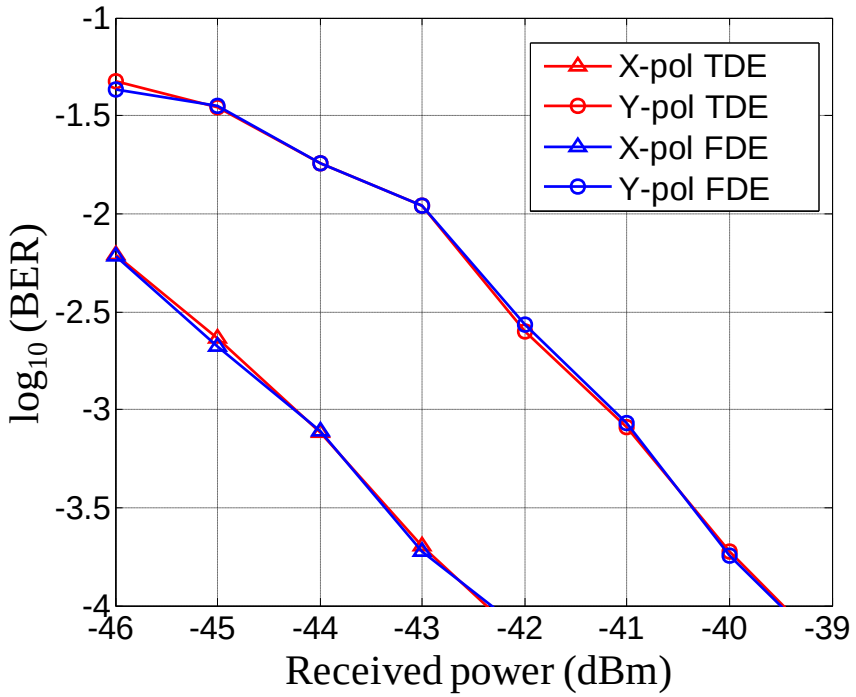

Fig.4.6: BER characteristics of the proposed adaptive FDE and the conventional TDE

Next, we test the sampling-phase adjustment capability of the proposed adaptive FDE. Receiver outputs are sampled at twice the symbol rate and interpolated to 10 samples per symbol. Such ten-fold oversampled sequences are down-sampled to 2 samples per symbol with different sampling phases and sent to the FDE. Figure 4.7 shows BER curves for 5 different sampling phases, which are swept with an increment of 10 % of the symbol interval. The BER curves are independent of the initial sampling phase, suggesting that the proposed adaptive FDE can adjust the sampling phase optimally in the similar manner to the TDE scheme based on *T*/2-spaced FIR

filters [19]. In our experiment, timing jitter may stem from modulation electronics and 100-km fiber transmission. In addition to the static adjustment of the initial sampling phase of ADCs, such relatively-fast timing jitter is also absorbed by the proposed FDE.

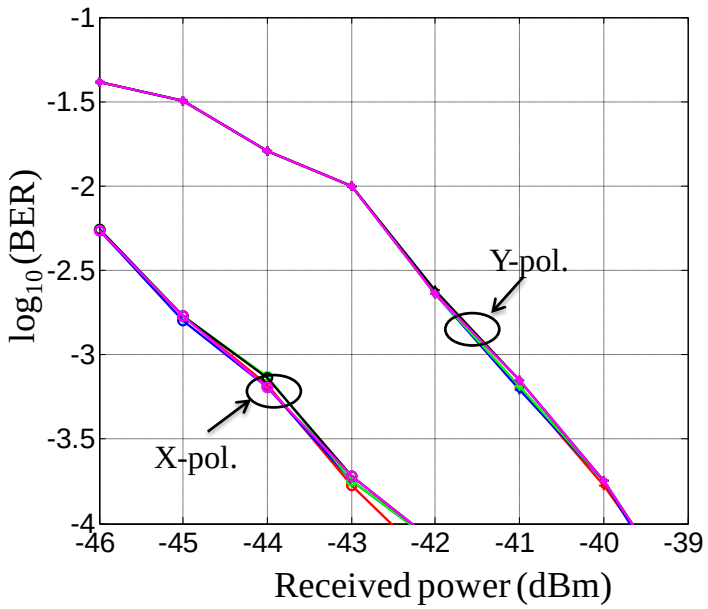

Fig.4.7: BER characteristics of the proposed FDE for different sampling phases. The sampling phases are swept with a resolution of 10 % of the symbol interval.

4.5.2 Results Regarding Monitoring

We estimate different impairments from the adaptive FDE and compare the result with that obtained from adaptive TDE. First, to test the algorithm for monitoring of CD, DGD and PDL, we conduct 40-Gbit/s dual-polarization unrepeated QPSK transmission experiments where only one DGD section of our PMDE is used to generate a fixed DGD value and also the amount of PDL is set to a constant value.

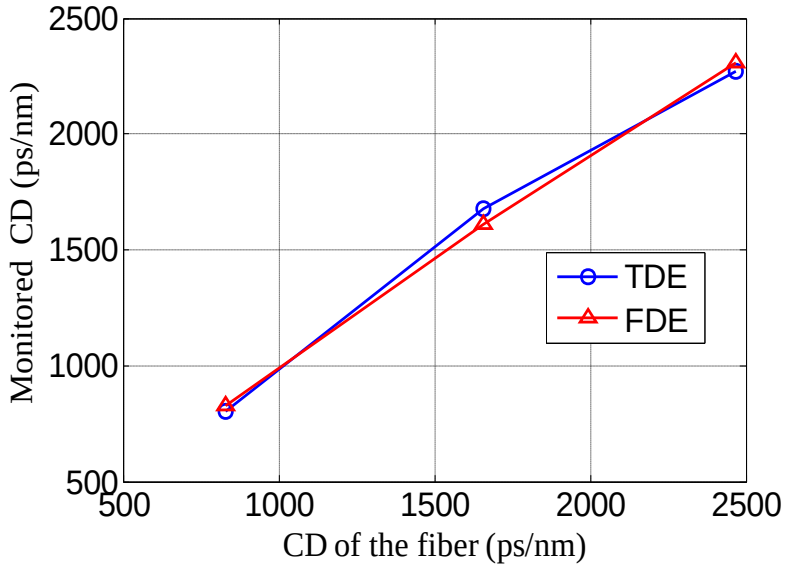

Fig. 4.8: Monitoring result of CD with 20-ps DGD and 3-dB PDL

Fig. 4.8 shows the monitoring results of CD value of 50-, 100- and 150-km of standard SMF in presence of 20-ps DGD and 3-dB PDL. The monitoring value agrees well with that of measured value by a standard CD measuring instrument.

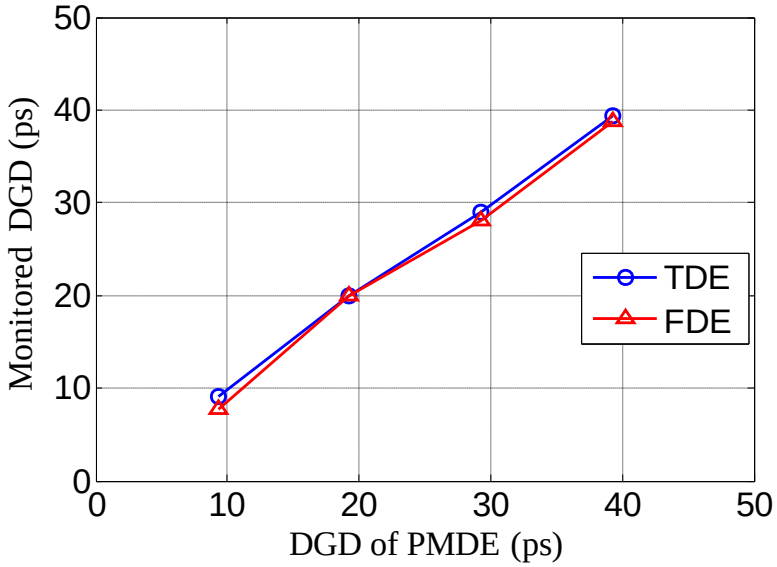

Fig. 4.9: Monitoring results of DGD for 1600 ps/nm CD and 3-dB PDL

DGD monitoring results are shown in Fig. 4.9 upto 40-ps in presence of 1600-ps/nm CD and 3-dB PDL. The monitored value is found very close to that of the PMDE. Fig. 4.10 shows the PDL estimation results in presence of 1600-ps/nm CD and 20-ps DGD. The measured value matches well with the set PDL value.

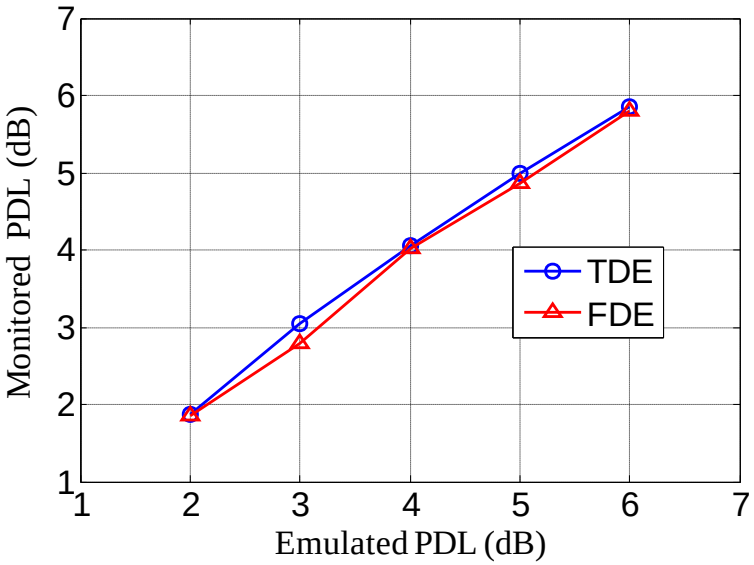

Fig. 4.10: Monitoring result of PDL with 1600-ps/nm and 20-ps DGD

It is important to note here that for all of the cases, there are no significant difference between monitoring results from the adaptive FDE and that from the conventional adaptive TDE.

To verify the second-order PMD monitoring algorithm, we estimate the statistical behavior of second-order PMD and compare it with the theoretical density listed in Table 3.1. In this experiment, we transmit a 100-Gbit/s dual-polarization QPSK signal through PMDE, which is set to generate a Maxwellian-distributed DGD with the mean value of 35 ps and a corresponding second-order PMD with a refresh rate of 10 ms, while CD and PDL were set to zero.

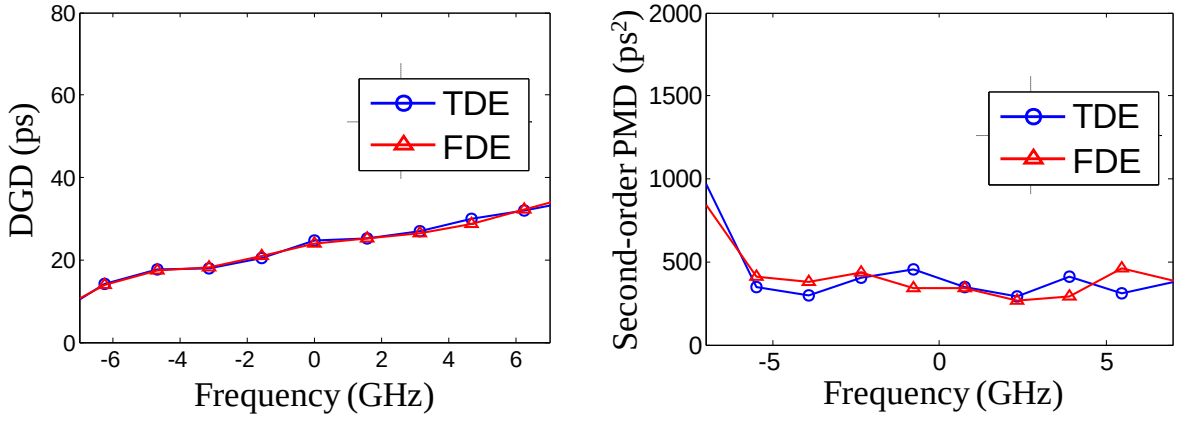

Fig. 4.11: Measured DGD and Second-order PMD spectrum from an arbitrary sample

Fig. 4.11 shows the estimated spectrum of DGD and second-order PMD. For both the cases, the estimated value from adaptive TDE and FDE are almost same. From such spectrum, we count the DGD and second-order PMD at centre frequency from 700 samples and calculate their

probability densities as shown in Fig.4.12. The measured probability densities for all the cases match well with the theory.

The mean DGD estimated from the TDE is 35.64 ps while that from FDE is 35.36 ps; both values are very close to the set value of 35 ps. As of second-order PMD, the mean value estimated from TDE is 627 ps^2 while that from FDE is 616 ps^2 which are about 20% less than the predicted mean value. The dissimilarity between the estimated second-order PMD and the theoretical prediction may stem from the inadequate number of statistical samples and using only three DGD sections in our PMDE which is insufficient to generate the second-order PMD similar to that of the real fiber.

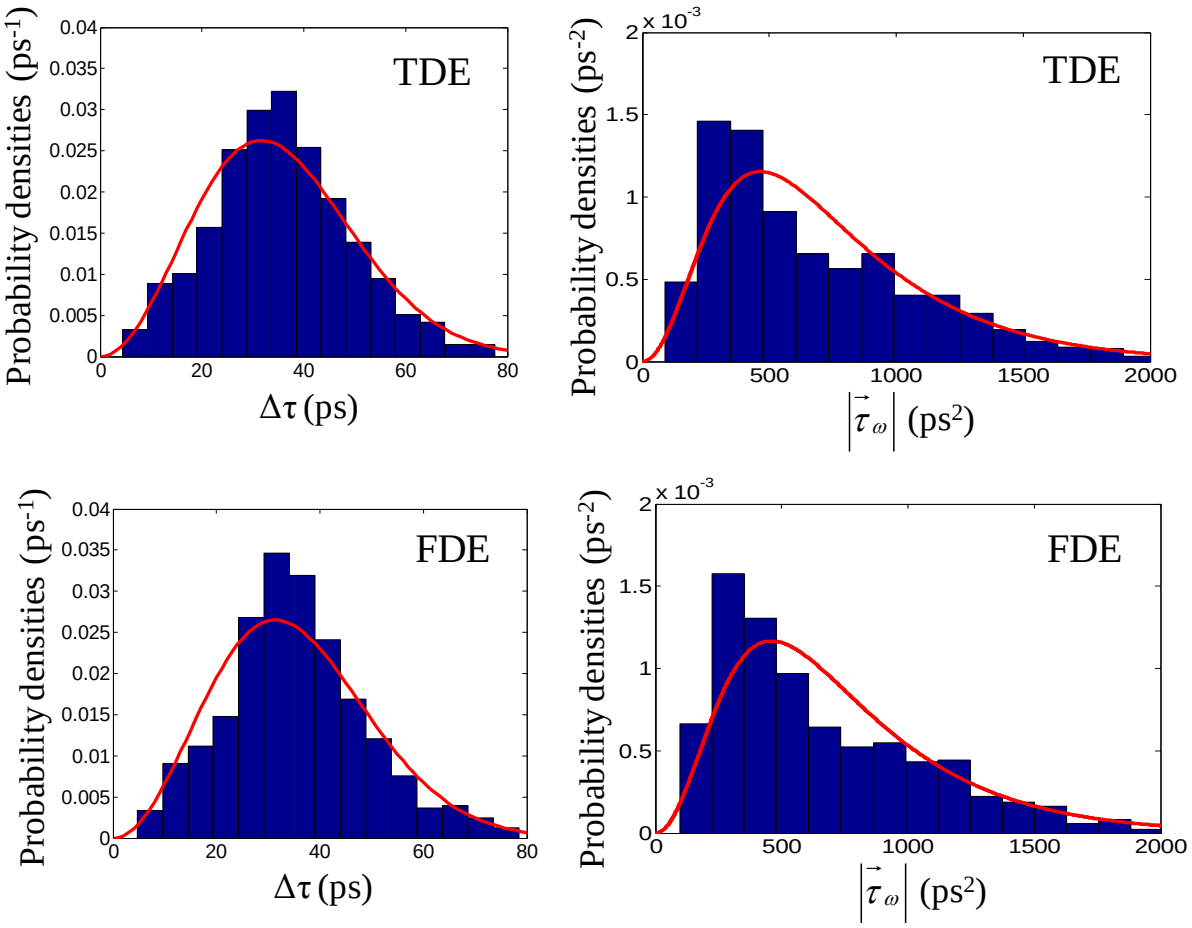

Fig.4.12: Probability densities of the first- and second-order PMD. Bars show those estimated from monitored values and solid curves are theoretical ones.

4.6 Chapter Summery

We have proposed a novel frequency-domain equalizer in digital coherent receivers, which operates on twofold-oversampled input sequences. Such an equalizer performs sampling-phase adjustment of ADCs, polarization demultiplexing, and signal equalization with computational complexity lower than the time-domain equalizer. The proposed equalizer is very efficient when long-tap filter implementation is necessary and therefore is a good choice for multi-impairment monitoring from the equalizer. The performance of the equalizer as well as multi-impairment monitoring from its tap coefficients are verified by 40-Gbits/s dual-polarization QPSK transmission experiments.

References

1. H. Sun, K.-T. Wu, and K. Roberts, "Real-time measurements of a 40 Gb/s coherent system," Opt. Express **16**, 873-879 (2008).
2. K. Roberts, M. O'Sullivan, K. Wu, H. Sun, A. Awadalla, D. J. Krause, and C. Laperle, "Performance of dual-polarization QPSK for optical transport system," J. Lightwave Technol. **27,** 3546-3559 (2009).
3. B. Spinnler, "Complexity of algorithms for digital coherent receivers," in *Proceedings of European Conference on Optical Communication* (2009), paper 7.3.6 (2009).
4. J. Leibrich and W. Rosenkranz "Frequency domain equalization with minimum complexity in coherent optical transmission systems," in *Optical Fiber Communication Conference*, OSA Technical Digest (Optical Society of America, 2010), paper OWV1.
5. B. Spinnler, "Equalizer design and complexity for digital coherent receivers," IEEE J. Sel. Topics Quantum Electron. **16**, 1180 - 1192 (2010).
6. P. Poggiolini, A. Carena, V. Curri, and F. Forghieri, "Evaluation of the computational effort for chromatic dispersion compensation in coherent optical PM-OFDM and PM-QAM systems," Opt. Express **17**, 1385-1403 (2009)
7. F. Pancaldi, G. Vitetta, R. Kalbasi, N. Al Dhahir, M. Uysal, and H. Mheidat, "Single-carrier frequency domain equalization," IEEE Signal Process. Mag. **25**, 37-56 (2008).
8. J. J. Shynk, "Frequency-domain and multirate adaptive filtering," IEEE Signal Process. Mag. **9**, 14-37(1992).

9. D. Falconer, S. L. Ariyavisitakul, A. Benyamin-Seeyar, and B. Eidson, "Frequency domain equalization for single-carrier broadband wireless systems", IEEE Commun. Mag. **40**, 58 - 66 (2002).
10. B. Farhang-Boroujeny, *Adaptive Filters-Theories and Applications*, (Johm Wiley and Sons, 1998).
11. K. Ishihara, R. Kudo, T. Kobayashi, A. Sano, Y. Takatori, T. Nakagawa, and Y. Miyamoto, "Frequency-Domain Equalization for Coherent Optical Transmission Systems," in *Optical Fiber Communication Conference*, OSA Technical Digest (CD) (Optical Society of America, 2011), paper OWW4.
12. R. Kudo, T. Kobayashi, K. Ishihara, Y. Takatori, A. Sano, and Y. Miyamoto, "Coherent optical single carrier transmission using overlap frequency domain equalization for long-haul optical systems," J. Lightwave Technol. **27**, 3721-3718 (2009).
13. J. C. Geyer, C. R. Fludger, T. Duthel, C. Schulien, and B. Schmauss, "Efficient Frequency Domain Chromatic Dispersion Compensation in a Coherent Polmux QPSK-Receiver," in *Optical Fiber Communication Conference*, OSA Technical Digest (CD) (Optical Society of America, 2010), paper OWV5.
14. R. Kudo, T. Kobayashi, K. Ishihara, Y. Takatori, A. Sano, E. Yamada, H. Masuda, and Y. Miyamoto "PMD compensation in optical coherent single carrier transmission using frequency-domain equalization," Electron. Lett. **45**, 124-125 (2009).
15. K. Ishihara, T. Kobayashi, R. Kudo, Y. Takatori, A. Sano, and Y. Miyamoto, "Frequency-domain equalization for coherent optical single-carrier transmission systems," IEICE Trans. Commun. **E92-B**, 3736-3743 (2009).
16. E. Lai, *Practical Digital Signal Processing for Engineers and Technicians***,** (Newnes, 2003).
17. D. Mansour and A. H. Gray "Unconstrained frequency-domain adaptive filter", *IEEE Trans. Acoust. Speech Signal Process.* **ASSP-30**, 726-734 (1982).
18. S. Haykin, *Adaptive Filter Theory* (Prentice Hall, 2001).
19. K. Kikuchi, "Clock recovering characteristics of adaptive finite-impulse-response filters in digital coherent optical receivers," Opt. Express **19**, 5611-5619 (2011).
20. G. Bosco, A. Carena, V. Curri, P. Poggiolini, and F. Forghieri, "Performance limits of nyquist-WDM and CO-OFDM in high-speed PM-QPSK systems," IEEE Photon. Technol. Lett. **22**, 1129–1131 (2010).

21. A. Oppenheim and R. W. Schafer, *Discrete-Time Signal Processing* (Prentice hall, 2009), Chap.9.
22. K. Kikuchi, "Phase-diversity homodyne detection of multilevel optical modulation with digital carrier phase estimation," IEEE J. Sel. Topics Quantum Electron. **12**, 563-570 (2006).

Chapter 5

Monitoring of Optical Signal-to-Noise Ratio

Optical signal-to-noise ratio (OSNR) monitoring is an important issue for optically amplified systems. Accurate OSNR monitoring in any digital signal processing (DSP) stage of coherent optical receiver is not yet available. In this work, we proposed and experimentally verified a novel method to monitor OSNR by measuring the higher-order statistical moments of the adaptive-equalizer output. The proposed scheme is simple and can monitor the in-band OSNR with good accuracy.

This chapter starts with background theory which includes definition of OSNR and its typical measurement technique and the definitions of higher-order statistical moments that will be required to understand the proposed OSNR monitoring algorithm. Section 2 describes our OSNR monitoring method and Sec. 3 provides its experimental verification. The final section summarizes the chapter.

5.1 Background Theory

5.1.1 Definition of OSNR

OSNR can be defined as the logarithmic ratio of the average optical signal power to the average optical noise power over a specific spectral bandwidth [1]. It can be expressed as

$$OSNR = 10\log\left(\frac{P_{sig.}}{P_{noise}}\right), \tag{5.1}$$

where

OSNR: optical signal-to-noise ratio bounded by bandwidth B_0, dB

$P_{sig.}$: signal power bound by B_0, mw

P_{noise}: noise power bound by B_0, mw

B_0: reference spectral bandwidth, nm.

Though there are different sources of noise in optical communication systems, in optically amplified systems, the noise source mainly stems from amplified spontaneous emission (ASE) [2]. Therefore, the OSNR in such system is defined as

$$OSNR = 10\log\left(\frac{P_{sig.}}{P_{ASE}}\right), \tag{5.2}$$

where P_{ASE} is the ASE noise bound by the reference bandwidth B_0, which is typically chosen as 0.1 nm (12.5 GHz).

5.1.2 Typical OSNR Measurement Technique

The optical spectrum analyzer (OSA) is the instrument typically used to measure OSNR. Most OSA units use the method defined by IEC 61280-2-9 standard [3]. Both signal and noise measurements are done over a specific spectral bandwidth B_r, known as the OSA's resolution bandwidth (RBW). The RBW filter acts as a band-pass filter allowing only a set amount of optical spectrum to strike the OSA's photo-detector. The photo-detector measures the average of all optical power in this spectral width.

As shown in Fig. 5.1, noise power at the signal wavelength cannot be measured directly because it is obscured by the signal itself. Hence, the noise measurement is performed at the wavelengths λ_1 and λ_2 which are located on both sides of the signal wavelength λ_0, by using the OSA's noise equivalent bandwidth (NEB) filter. Then the results are interpolated to calculate the noise power at the signal wavelength. Finally, the OSNR is calculated by the following equation:

$$OSNR = 10\log\left(\frac{P_{sig.}}{P_{noise}}\right) + 10\log\left(\frac{B_m}{B_r}\right), \tag{5.3}$$

where B_m is NEB and B_r is RBW and the interpolated noise is calculated as $P_{noise} = \{P_{noise}(\lambda_1) + P_{noise}(\lambda_1)\}/2.$

Equation (5.3) is similar to Eq. (5.1) with the exception of the last term. This term is a scaling factor used to adjust the measured noise power bound by the noise equivalent bandwidth, to the signal RBW bandwidth.

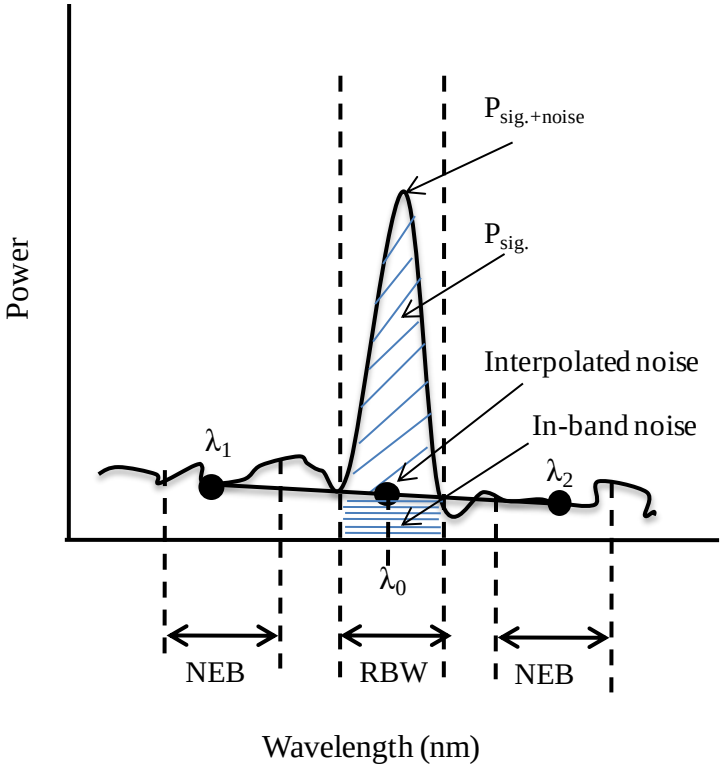

Fig. 5.1: OSA view of typical signals and OSNR parameters

For dense wavelength-division multiplexed (DWDM) system IEC 61280-2-9 defines the OSNR measuring method. Signal, noise power, and OSNR measurements and calculations are performed at each individual DWDM channel. For *i*-th channel the OSNR is calculated as

$$OSNR_i = 10\log\left(\frac{P_{sig.,i}}{P_{noise,i}}\right) + 10\log\left(\frac{B_m}{B_r}\right). \quad (5.4)$$

Noise measurements for interpolation are generally made at 1/2 ITU channel spacing (or less) on both sides of the signal wavelength such as $P_{noise,i} = \{P_{noise}(\lambda_{i-\Delta ITU/2}) + P_{noise}(\lambda_{i-\Delta ITU/2})\}/2.$ For tightly spaced DWDM channels, a tighter width is used.

Note that, special precaution is required if we measure the OSNR on the filtered end or demux side (drop side) of a DWDM, optical add-drop multiplexer (OADM), or reconfigurable optical add-drop multiplexer (ROADM) [4]. Due to DWDM, OADM, or ROADM filtering effects, a false noise floor may appear in an OSA. This can result in an incorrect automatic OSNR measurement. The correct measurement can be made by manually setting the OSA noise markers to the proper noise floor.

It should be noted here that the laser spectral width varies with the modulation rate; higher the rate wider the signal spectral width. Thus, RBW should be chosen according to the modulation rate. Table 5.1 shows the minimum recommendation for RBW that will cause a certain measurement error for various transmission rates and NRZ modulation [3].

Table 5.1: Minimum RBW for Different Signal Modulation Rate

Modulation Rate (Gbps)	Minimum RBW for less than 0.1 dB error (nm)	Minimum RBW for less than 1 dB error (nm)
40	1	--
10	≥ 0.2	≥ 0.1
2.5	≥ 0.09	≥ 0.03

5.1.3 Statistical Moments

The *n*-th moment of a distribution is the expected value of the *n*-th power of the deviations from a fixed value. The first moment of the distribution of the random variable *x* is the expectation operator, i.e., the population mean (if the first moment exists). Generally, in higher orders, either the central moments (moments about the mean) or the moments about zero are considered. The *k*-th central moment of a real-valued random variable *x* is given by

$$\mu_k = E\{(x-\mu)^k\}, \tag{5.5}$$

where, E is the mathematical expectation operator and μ is the expected value (mean) given as $\mu = E\{x\}$. The first central moment is thus 0. The second central moment is the variance, while third and fourth normalized central moments are called skewness and kurtosis, respectively.

Variance:

The variance of *x* is given by:

$$\mu_2 = E\{(x-\mu)^2\}. \tag{5.6}$$

The variance is used as a measure of how far a set of numbers are spread out from each other. The positive square root of variance is the standard deviation σ. The *normalized n*th central moment or standardized moment is the *n*th central moment divided by σ^n; the normalized *n*th central moment of $x = \mathrm{E}((x-\mu_1)^n)/\sigma^n$. These normalized central moments are dimensionless quantities, which represent the distribution independently of any linear change of scale.

For a complex random variable z, the variance can be expressed as

$$\mu_{2,c} = E\{(z-\mu)(z-\mu)^*\}$$

$$= E\{|z-\mu|^2\}. \tag{5.7}$$

With a zero mean value Eq. (5.7) reduces as

$$\mu_{2,c} = E\{|z|^2\}. \tag{5.8}$$

Skewness:

The skewness of a random variable x is the third standardized moment, denoted γ_1 and defined as

$$\gamma_1 = \frac{\mu_3}{\sigma^3} = E\left\{\frac{(x-\mu)^3}{\sigma^3}\right\}, \tag{5.9}$$

where μ_3 is the third moment about the mean.

Skewness is a measure of the asymmetry of the probability distribution of a real-valued random variable. The skewness value can be positive or negative, or even undefined. As shown in Fig. 5.2 a negative skew indicates that the *tail* on the left side of the probability density function is *longer* than the right side and the bulk of the values lie to the right of the mean. A positive skew indicates that the *tail* on the right side is *longer* than the left side and the bulk of the values lie to the left of the mean. A zero value indicates that the values are relatively evenly distributed on both sides of the mean, typically but not necessarily implying a symmetric distribution [5].

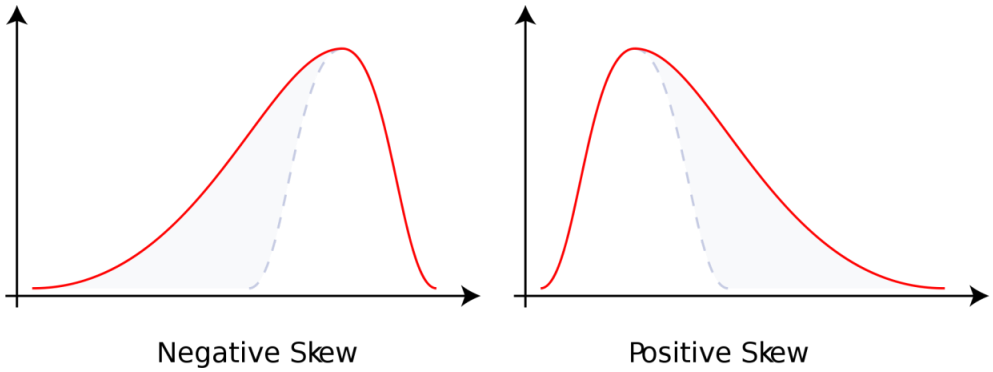

Fig. 5.2: Illustration of positive and negative skew

Kurtosis:

The fourth standardized moment can be defined as kurtosis as

$$\beta_2 = \frac{\mu_4}{\sigma^4} = E\left\{\frac{(x-\mu)^4}{\sigma^4}\right\}, \tag{5.10}$$

where μ_4 is the fourth moment about the mean.

Many authors define Kurtosis as a measure of the "peakedness" of the probability distribution (however, this is not strictly true [6]). Higher kurtosis means more of the variance is the result of infrequent extreme deviations, as opposed to frequent modestly sized deviations.

However, kurtosis is more commonly defined as the fourth-cumulant divided by the square of the second-cumulant, which is equal to the fourth moment around the mean divided by the square of the variance of the probability distribution minus 3,

$$\gamma_2 = \frac{\mu_4}{\sigma^4} - 3, \tag{5.11}$$

which is also known as **excess kurtosis**. The "minus 3" at the end of this formula is often explained as a correction to make the kurtosis of the normal distribution equal to zero.

There are three forms of kurtosis: Leptokurtic, Mesokurtic, Platykurtic. When kurtosis is zero, it is called mesokurtic and it is corresponds to normal distribution. The negative kurtosis is platykurtic and positive kurtosis is leptykurtic. When compared to a normal distribution, a platykurtic data set has a flatter peak around its mean, which causes thin tails within the distribution. The flatness results from the data being less concentrated around its mean. Leptokurtic distributions have higher peaks around the mean compared to normal distributions, which leads to thick tails on both sides. These peaks result from the data being highly concentrated around the mean, due to lower variations within observations.

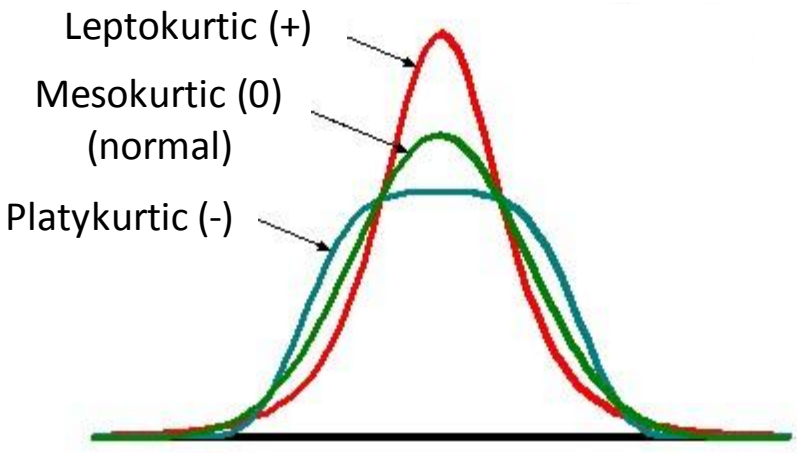

Fig. 5.3: Illustration of different types of kurtosis

Normalized 4-th order moment of complex random variable z around zero mean is given as

$$\beta_{2,c} = \frac{\mu_4}{\sigma^4} = \frac{E\left\{|z|^4\right\}}{\left[E\left\{|z|^2\right\}\right]^2}. \tag{5.12}$$

There are different ways for generalization of kurtosis for complex random variables. The most commonly used definition [7, 8, 9] is

$$\gamma_{2,c} = \beta_{2,c} - \frac{\left|E\left\{z^2\right\}\right|^2}{\left[E\left\{|z|^2\right\}\right]^2} - 2. \tag{5.13}$$

With such a definition, similar to the kurtosis of a real-valued Gaussian random variable, the value of $\gamma_{2,c}$ is zero for both circular and noncircular complex Gaussian random variables. Furthermore, in this measure, kurtosis value of a sub-Gaussian complex random variable is negative and that of a super-Gaussian complex random variable is positive, irrespective of the circularity/noncircularity of the random variable.

5.2 Proposed OSNR Monitoring Method

We monitor the OSNR from the statistical characteristics of adaptive-equalizer output. When the channel power is modest so as to operate the transmission system in the optically linear region or weakly nonlinear region and also the length of the adaptive FIR filter is sufficient enough to

compensate for all linear impairments, the output signal from the adaptive filter can be approximated as

$$v_n \approx \sqrt{C}a_n + \sqrt{N}w'_n * h_n \ , \tag{5.14}$$

where a_n is the M-ary PSK symbol amplitude, C is the carrier power scale factor, N is the noise power scale factor, w'_n is the amplified spontaneous emission (ASE) noise, * is the convolution operator, and h_n is the filter impulse response. The symbol amplitude a_n and the noise amplitude w'_n are stochastically-independent random variables, whose means are 0 and variances are 1. When we neglect the polarization dependent loss, the coherent optical channel has the 'all-pass' nature; and thus h_n has an impulse response of an all-pass filter [10, 11]. Under such a condition, we can write $w'_n * h_n = w_n$, where w'_n is statistically equivalent to w_n [12]. Thus, Eq. (5.14) can be rewritten as

$$v_n = \sqrt{C}a_n + \sqrt{N}w_n. \tag{5.15}$$

Assuming that the modulation format is QPSK and w_n has the Gaussian distribution, we can find the statistical prosperities of a_n and w_n as shown in Table 5.2.

Table 5.2: Statistical Properties of a_n and w_n

Parameter	a_n	w_n
Mean	0	0
Variance	1	1
Kurtosis	1	2

In the following, using the statistical properties in Table 5.2, we develop an OSNR monitoring algorithm by measuring the second- and fourth- order moments of v_n.

The second-order moment μ_2 of v_n can be expressed as

$$\mu_2 = E\{v_n v_n^*\}$$

$$= CE\{a_n a_n^*\} + \sqrt{CN}E\{a_n w_n^*\} + \sqrt{CN}E\{a_n^* w_n\} + NE\{w_n w_n^*\}$$

$$= CE\{|a_n|^2\} + \sqrt{CN}\,(E\{a_n w_n^*\} + E\{a_n^* w_n\}) + NE\{|w_n|^2\}, \tag{5.16}$$

where superscript $(\bullet)^*$ denotes complex conjugate.

Since signal and noise are mutually independent complex-valued random processes with zero mean, we can write

$$E\{a_n w_n^*\} = 0, \tag{5.17}$$

$$E\{a_n^* w_n\} = 0. \tag{5.18}$$

Also we have $E\{|a_n|^2\}$=1and $E\{|w_n|^2\}$=1. Putting these values in Eq. (5.16) yields

$$\mu_2 = C + N. \tag{5.19}$$

On the other hand, the fourth-order moment of v_n can be written as

$$\begin{aligned}\mu_4 &= E\{(v_n v_n^*)^2\} \\ &= S^2 E\{(a_n a_n^*)^2\} + 2S\sqrt{SN}\,(E\{a_n a_n^* a_n w_n *\} + E\{a_n a_n^* a_n * w_n\}) + SN(E\{(a_n w_n *)^2\} + \\ &\quad 4E\{a_n a_n^* w_n w_n^*\} + E\{(a_n * w_n)^2\}) + 2N\sqrt{SN}\,(E\{w_n w_n^* a_n w_n *\} + E\{w_n w_n^* a_n * w_n\}) + N^2 E\{(w_n w_n^*)^2\}.\end{aligned} \tag{5.20}$$

Since the carrier signal and noise are independent and both are zero mean processes, all terms in Eq. (5.20) with single appearance of a_n or w_n disappears. Thus,

$$E\{a_n a_n^* a_n w_n *\} = E\{a_n a_n^* a_n\} \cdot E\{w_n *\} = 0. \tag{5.21}$$

Similarly,

$$E\{a_n a_n^* a_n * w_n\} = 0, \tag{5.22}$$

$$E\{w_n w_n^* a_n w_n *\} = 0, \tag{5.23}$$

$$E\{w_n w_n^* a_n * w_n\} = 0. \tag{5.24}$$

Moreover, the real and imaginary components of carrier and noise can be considered as orthogonal; hence in such condition

$$E\{(a_n w_n^*)^2\} = E\{(a_n)^2\} \cdot E\{(w_n^*)^2\} = 0, \tag{5.25}$$

$$E\{(a_n^* w_n)^2\} = E\{(a_n^*)^2\} \cdot E\{(w_n)^2\} = 0. \tag{5.26}$$

Also, it is evident that, $E\{(a_n a_n^*)^2\} = E\{|a_n|^4\}$, $E\{(w_n w_n^*)^2\} = E\{|w_n|^4\}$ and $E\{a_n a_n^* w_n w_n^*\} = E\{|a_n|^2 |w_n|^2\}$.

Therefore, Eq. (5.20) can be rewritten as

$$\mu_4 = S^2 E\{|a_n|^4\} + 4CNE\{|a_n|^2 |w_n|^2\} + N^2 E\{|w_n|^4\}$$

$$= \gamma_{2,a} C^2 + 4CN + \gamma_{2,w} N^2, \tag{5.27}$$

where, $\gamma_{2,a}=E\{|a_n|^4\}/E\{|a_n|^2\}^2$ and $\gamma_{2,w}= E\{|w_n|^4\}/E\{|w_n|^2\}^2$ are kurtoses of the signal and the noise, respectively. Noting that $\gamma_{2,a}$ =1 for the *M*-ary PSK signal; on the other hand, ASE noise can be approximated as the Gaussian-noise [13] and thus $\gamma_{2,w}$ =2 [14]. Therefore, Eq. (5.27) can be written as

$$\mu_4 = C^2 + 4CN + 2N^2. \tag{5.28}$$

In a practical system, second- and fourth-order moments are calculated from a block of *L* symbols as in Eqs. (5.29) and (5.30):

$$\mu_2 \approx \frac{1}{L}\sum_{n=0}^{L-1} |v_n|^2 , \tag{5.29}$$

$$\mu_4 \approx \frac{1}{L}\sum_{n=0}^{L-1} |v_n|^4 . \tag{5.30}$$

Solving Eq. (5.19) and (5.28), we get

$$C = \sqrt{2\mu_2^2 - \mu_4}, \tag{5.31}$$

$$N = \mu_2 - \sqrt{2\mu_2^2 - \mu_4}. \tag{5.32}$$

When we determine μ_2 and μ_4, by using Eqs. (5.29) and (5.30), we can estimate the carrier-to-noise ratio (CNR) as

$$CNR = \frac{\sqrt{2\mu_2^2 - \mu_4}}{\mu_2 - \sqrt{2\mu_2^2 - \mu_4}} . \tag{5.33}$$

In this point we make two assumptions-

(1) The input launch power to the fiber is not high enough, so that the fiber nonlinearity is negligible. In such a case the measure noise as in Eq. (5.32) is the contribution of ASE noise.

(2) After the adaptive-equalizer, all linear fiber transmission impairments are perfectly compensated. This assumption is practical as the accumulated fiber dispersion after transmission of thousands of km can be compensated without any notable penalty using digital filters with sufficient number of taps in coherent optical receivers [15].

With the above conditions, OSNR in dB can be estimated from the CNR value given by Eq. (5.33) as

$$OSNR_{dB} = 10\log_{10}(CNR) + 10\log_{10}\left(R_s / B_r\right), \tag{5.34}$$

where R_s is the symbol rate and (R_s/B_r) is a scaling factor to adjust the measured noise power to some reference bandwidth B_r.

5.3 Experimental Verification

5.3.1 Experimental Setup

To demonstrate the effectiveness of the proposed algorithm, we carried out 10-Gsymbol/s QPSK transmission experiments shown in Fig. 5.4. The transmitter laser and the local oscillator (LO) were distributed-feedback lasers (DFB-LDs) having a center wavelength of 1552 nm and a 3-dB linewidth of 150 kHz. A 20-Gbit/s NRZ-QPSK optical signal was generated by using a $LiNbO_3$ optical IQ modulator (IQM), which was driven by two streams of a 2^9-1 pseudo-random binary sequence (PRBS) from an arbitrary waveform generator (AWG). The signal was then pass through a standard single mode fiber (SMF). ASE noise was separately generated by an erbium-doped fiber amplifier (EDFA) and coupled to the signal by an optical coupler. The combined signal and noise passed through a variable optical attenuator (VOA). Then, a coupler spit it into two paths: one was connected to an optical spectrum analyzer (OSA) to measure OSNR independently, and the other was incident on a phase diversity homodyne receiver. Outputs of the receiver were sampled and digitized at 20 Gsample/s with analog-to-digital converters (ADCs) and sent to offline DSP.

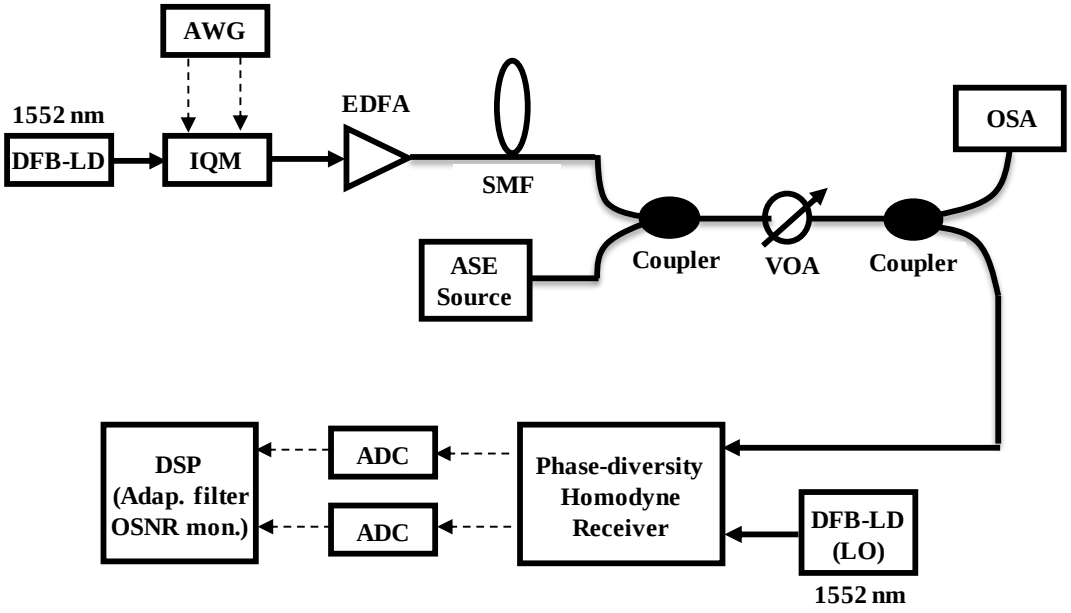

Fig. 5.4: Schematics of experimental setup to verify the proposed OSNR monitoring algorithm

In the DSP circuit, a 33-tap half-symbol-spaced adaptive FIR filter was used for sampling phase adjustment [16] and compensation for linear impairments. The constant-modulus algorithm (CMA) was used for FIR-filter adaptation. Then, the filter output was used directly to estimate OSNR without carrier recovery since the second- and fourth-order moments are independent of the carrier phase.

5.3.2 Results and Discussions

We monitor OSNR over a range from 6 dB to 13 dB with 0.1-nm ASE-noise bandwidth, which correspond to a bit-error rate (BER) of 4×10^{-2} and an error-free condition, respectively. As shown in Fig. 5.5, OSNR estimated by our proposed algorithm agrees well with OSNR measured by OSA for both channel dispersion of 0 and 1600 ps/nm.

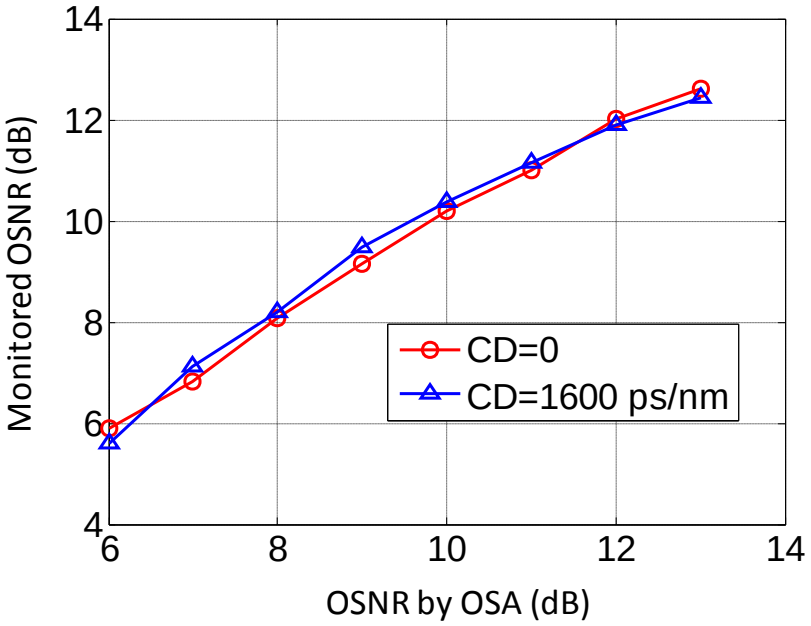

Fig. 5.5: OSNR Monitoring results as a function of OSNR measured by the OSA

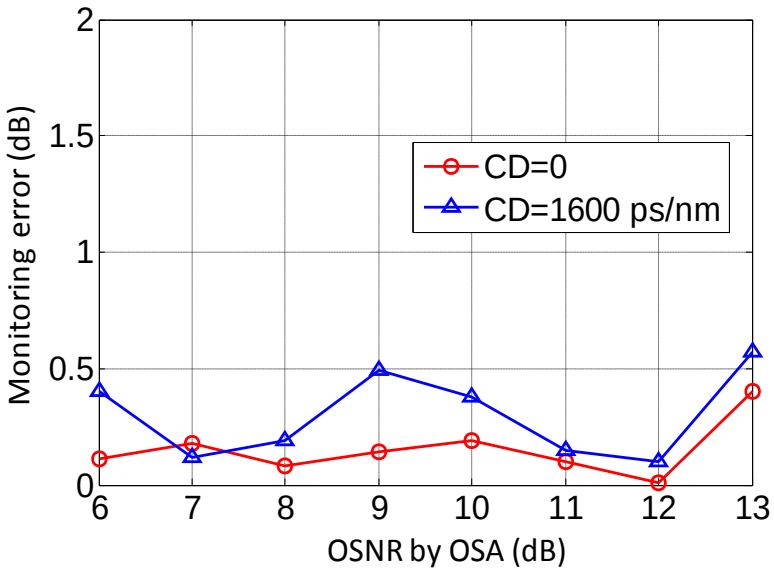

Fig. 5.6: Monitoring error as a function of OSNR measured by the OSA

The monitoring error is shown in Fig. 5.6 for the CD value of 0 ps/nm and 1600 ps/nm. For both the cases, the monitoring error always found below 1 dB. Thus, the fiber dispersion has no significant effect in the monitoring as it is compensated by the FIR filters.

5.4 Chapter Summary

We have proposed a new OSNR monitoring method in digital coherent receivers by measuring second- and fourth- order statistical moments of the adaptive-equalizer output. The effectiveness of such algorithm is verified by 20-Gbits/s QPSK transmission experiments.

References

1. B. Chomycz, *Planning Fiber Optics Networks*, (McGraw Hill, 2009), Chap.3.
2. P. V. Kumar, M. Z. Win, H.-F. Lu, and C. N. Georghiades, *Optical Fiber Telecommunication IV B* (Academic press, 2008), Chap. 17.
3. IEC61280-2-9, "Fibre optic communication subsystem test procedures, Part 2-9: Digital systems- optical signal-to-noise ratio measurement procedures for dense wavelength-division multiplexed systems," International Electrotechnical Commission (2002).
4. F. Audet, Commissioning ROADMS, Application note 169, EXFO Electro-Optical Engineering Inc., (2007).
5. P. T. von Hippel, "Mean, median, and skew: Correcting a textbook rule," Journal of Statistics Education **13** (2005).
6. R. B. Darlington, "Is kurtosis really "peakedness?"" *The American Statistician* **24**, 19-22 (1970).
7. S. C. Douglas, "Fixed-point algorithms for the blind separation of arbitrary complex-valued non-gaussian signal mixtures," *EURASIP J. Advances in Sig. Process.* **2007**, 83–83 (2007).
8. H. Li and T. Adali, "A class of complex ICA algorithms based on the kurtosis cost function," IEEE Trans. Neural Net. **19,** 408–420 (2008).
9. F. D Neeser and J. L. Massey, "Proper complex random processes with applications to information theory," IEEE Trans. Inform. Theory **39**, 1293–1302 (1993).
10. D. E. Crivelli, H. S. Carrer, and M. R. Hueda, "Adaptive digital equalization in the presence of chromatic dispersion, PMD, and phase noise in coherent fiber optic systems," in *Proceedings of Global Telecommunications Conference* (2004), pp. 2545–2551.
11. E. Ip and J. M. Kahn, "Digital equalization of chromatic dispersion and polarization mode dispersion," J. Lightwave Technol. **25**, 2033-2043 (2007).

12. G. Colavolpe, T. Foggi, E. Forestieri, and G. Prati, "Robust multilevel coherent optical systems with linear processing at the receiver," J. Lightwave Technol. **27**, 2357-2369 (2009).
13. W. S. Wong, H. A. Haus, L. A. Jiang, P. B. Hansen, and M. Margalit, "Photon statistics of amplified spontaneous emission noise in a 10-Gbit/s optically preamplified direct-detection receiver," Opt. Lett. **23**, 1832-1834 (1998).
14. R. Matzner, "An SNR estimation algorithm for complex baseband signals using higher order statistics," Facta Universitatis (Nis) **6**, 41–52 (1993).
15. Seb J. Savory, "Digital filters for coherent optical receivers," Opt. Express **16**, 804-817 (2008).
16. K. Kikuchi, "Clock recovering characteristics of adaptive finite-impulse-response filters in digital coherent optical receivers," Optics Express **19**, 5611-5619 (2011).

Chapter 6

Conclusions

6.1 Conclusions

The objective of enabling optical performance monitoring (OPM) in digital coherent receivers has been successfully completed. The considered parameters for monitoring are linear fiber transmission impairments, such as chromatic dispersion (CD), first- and second-order polarization mode dispersion (PMD), polarization dependent loss (PDL), and optical signal-to-noise ratio (OSNR). In this thesis, we have presented the new and novel concepts and results, both theoretically and experimentally, for OPM in digital coherent receivers.

The importance of the OPM for the next generation optical networks is outlined in chapter 1. Different methods for the OPM have been reviewed and motivations of thesis are clearly explained.

The background of digital coherent receivers is given in Chapter 2, which covered the principle of coherent detection and digital signal processing (DSP) based coherent receivers. Various functional blocks in a typical DSP core of such receiver have been discussed.

In Chapter 3 of this thesis, multi-impairment monitoring in digital coherent receiver is explored. The monitoring method is based on the analysis of transfer functions of four adaptive finite-impulse-response (FIR) filters that are used in the two-by-two butterfly configuration in digital coherent receivers for compensation for all linear transmission impairments. A novel algorithm to monitor the individual impairments from the single transfer matrix is reported. The measurable impairments include CD, differential group delay (DGD), PDL, second-order PMD including its components polarization dependent chromatic dispersion (PCD) and depolarization (DEP) of principle states of polarization (PSPs). For filter adaptation the constant-modulus algorithm (CMA) has been used. However, such algorithm may suffer from the singularity problem which means both output ports of the butterfly configuration converge to the same polarization tributary. Consequently, such problem is avoided by introducing the training mode before the blind CMA. Singularity free operation of CMA with the training mode as well as the

proposed multi-impairment monitoring from the FIR filters are verified by dual-polarization QPSK transmission experiments.

The important issue for multi-impairment monitoring from adaptive equalizer is that the filter length should be long enough to compensate for all fiber transmission impairments. However, it is difficult to implement long-tap FIR filters in an application-specific integrated circuit (ASIC) or field-programmable gate array (FPGA) as the computational complexity of such filters increases sharply with the number of taps. In Chapter 4 of this thesis, we propose a novel adaptive frequency-domain equalizer (FDE) for a digital coherent receiver which reduces the computational cost significantly compare to FIR based equalizer. The proposed algorithm is based on CMA and by introducing even and odd sub-equalizer concept, we enable the FDE to operate on the two-fold over-sampled input sequence even in the block processing mode. Thus, when it is used in butterfly structure, it performs equalization, polarization demultiplexing and clock recovery functionalities simultaneously. The equalization characteristics of such adaptive FDE and the performances of the multi-impairment monitoring from the tap coefficients of the proposed FDE are verified and compared with its counterpart of the conventional FIR-based equalizer by 40-Gbits/s dual-polarization QPSK transmission experiments.

In Chapter 5 of this thesis, we present a new method to monitor the OSNR in digital coherent receivers. The method is based on the measurement of higher-order statistical moment of adaptive-equalizer output. The symbol-spaced signal samples and noise samples at the adaptive-equalizer output have well-defined but dissimilar statistical properties. A formula is derived to express the carrier-to-signal ration (CNR) in terms of second- and fourth- order statistical moments of adaptive-equalizer output. Then, OSNR is estimated from the CNR value by scaling the noise bandwidth to the reference bandwidth. The proposed OSNR monitoring algorithm is verified by QPSK transmission experiments.

6.2 Future Works

A number of areas remain open to further investigations, these include the following points:

Fiber nonlinearity monitoring

Fiber nonlinearity monitoring is an important issue for reconfigurable WDM networks. The signal degradation from the fiber nonlinearity accumulates during propagation along the optical transmission line and can only be fully characterized at the final destination. Therefore,

nonlinearity monitoring in digital coherent receivers will be an important task. Moreover, such monitoring information can open the possibility to develop the fiber-nonlinearity tolerant OSNR monitoring scheme.

Equalization and monitoring for high-order QAM

Throughout this thesis the CMA is used for adaptive equalization. Though the high-order QAM modulation formats do not have constant modulus, the CMA can be applied to such formats. However, the convergence and equalization performance of CMA is not so good for higher-order QAM. Hence, further modification of CMA is required.

Moreover, though the OSNR monitoring algorithm presented in this thesis can be theoretically extended for high-order QAM modulation formats, a very long block of data is required to achieve a good statistical prediction of such signal. Hence, an alternative OSNR monitoring method should be introduced for such transmission system.

Further investigation on adaptive FDE

The proposed adaptive FDE can be implemented with much reduced complexity than the conventional time-domain adaptive equalizer. However, research should be carry out for further reduction of the computational cost of the equalizer. Especially, the requirements of gradient constraint should be examined for coherent optical communication systems, because it can be omitted if the filter input signal satisfies particular conditions. Moreover, in the proposed FDE, we calculate the cost function in the time domain. Further research is required for gradient estimation entirely in the frequency domain.

Publications Related to this work

Journals:

1. **Md. S. Faruk**, Y. Mori, C. Zhang, K. Igarashi, and K. Kikuchi, "Multi-impairment monitoring from adaptive finite-impulse-response filters in a digital coherent receiver," Opt. Express **18**, 26929-26936 (2010).
2. **Md. S. Faruk** and K. Kikuchi, "Adaptive frequency-domain equalization in digital coherent receivers," Opt. Express **19**, 12789-12798 (2011).
3. **Md. S. Faruk** and K. Kikuchi, "Monitoring of linear fiber transmission impairments from adaptive frequency-domain equalizer in digital coherent receivers," in preparation, Photon. Technol. Lett. (2011).

International Conferences:

1. **Md. S. Faruk**, Y. Mori, C. Zhang, and K. Kikuchi, "Proper polarization demultiplexing in coherent optical receiver using constant modulus algorithm with training mode, " in *Proceedings of Optoelectronics and Communications Conference (2010)*, Paper 9B3-3.
2. **Md. S. Faruk**, Y. Mori, C. Zhang, and K. Kikuchi, "Multi-impairments monitoring from the equalizer in a digital coherent optical receiver," in *Proceedings of European Conference on Optical Communication* (2010), Paper Th.10.A.1.
3. **Md. S. Faruk**, Y. Mori, C. Zhang, K. Igarashi, and K. Kikuchi, "Second-order PMD monitoring from adaptive FIR-filter tap coefficients in a digital coherent receiver," in *Optical Fiber Communication Conference*, OSA Technical Digest (CD) (Optical Society of America, 2011), paper OWN3.
4. **Md. S. Faruk** and K. Kikuchi, "Frequency-domain adaptive equalization in digital coherent receivers," in *CLEO:2011 - Laser Applications to Photonic Applications*, OSA Technical Digest (CD) (Optical Society of America, 2011), paper CThH7.
5. **Md. S. Faruk** and K. Kikuchi, "Monitoring of optical signal-to-noise ratio using statistical moments of adaptive-equalizer output in digital coherent receivers," in *Proceedings of Optoelectronics and Communications Conference* (2011), Paper 6B4_3.

Domestic Conferences:

1. **Md. S. Faruk** and K. Kikuchi, "Frequency-domain adaptive equalization for coherent optical transmission system," in *Proceedings of Institute of Electronics, Information and Communication Engineers (IEICE) Society Conference* (2010), Paper B-10-71.
2. **Md. S. Faruk** and K. Kikuchi, "Monitoring of fiber transmission impairments using digital coherent optical receivers," in *Proceedings of the Conference of Solid-state Electronics and Opto-electronics* (2011), Paper 1-25.
3. **Md. S. Faruk**, Y. Mori, C. Zhang, and K. Kikuchi, "Frequency-domain adaptive equalization for polarization-multiplexed coherent optical transmission system," in *Proceedings of Institute of Electronics, Information and Communication Engineers (IEICE) general conference* (2011), Paper B-10-49.

Workshop:

1. **Md. S. Faruk** and K. Kikuchi, "Optical performance monitoring in digital coherent receivers," *Italy-Japan Joint Workshop on Advanced Photonic Technologies for Communication and Sensing*, Pisa (Italy), Feb. 23-25 (2011).

Technical Report:

1. **Md. S. Faruk** and K. Kikuchi, "Multi-impairment monitoring from adaptive frequency-domain equalizer in digital coherent optical receivers," to be presented, *Technical Committee on Optical Communication Systems (OCS) 2011, the Institute of Electronics, Information and Communication Engineers (IEICE)*, Hokkaido (Japan), Aug. 25-26, 2011.

Appendix

A1.Update equation for the LMS

According to gradient decent algorithm the tap coefficients update is done as

$$\mathbf{h}(n+1) = \mathbf{h}(n) + \mu'[-\nabla \mathbf{J}(n)]. \tag{1}$$

where $\nabla \mathbf{J}(n)$ is gradient vector which is the derivative of mean square error $J(n)$, μ' is the step size parameter. In case of LMS algorithm, the error value can be consider as

$$\begin{aligned} e(n) &= d(n) - v(n) \\ &= d(n) - \mathbf{u}(n)\mathbf{h}(n) \end{aligned} \tag{2}$$

where $d(n)$ is the desired symbol and $v(n)$ is the filter output. In case of complex input, $J(n)$ can be written as

$$J(n) = \left|e(n)\right|^2 = e(n)e^*(n) \tag{3}$$

Thus, the gradient vector can be written as

$$\begin{aligned} \nabla \mathbf{J}(n) &= \frac{\partial}{\partial \mathbf{h}(n)}\left\{e(n)e^*(n)\right\} \\ &= e(n)\frac{\partial}{\partial \mathbf{h}(n)}\left\{e^*(n)\right\} + e^*(n)\frac{\partial}{\partial \mathbf{h}(n)}\left\{e(n)\right\} \\ &= e(n)\frac{\partial}{\partial \mathbf{h}(n)}\left\{d^*(n) - \mathbf{u}^*(n)\mathbf{h}^*(n)\right\} + e^*(n)\frac{\partial}{\partial \mathbf{h}(n)}\left\{d(n) - \mathbf{u}(n)\mathbf{h}(n)\right\} \\ &= -e(n)\mathbf{x}^*(n)\frac{\partial \mathbf{h}^*(n)}{\partial h(n)} - e^*(n)\mathbf{x}(n)\frac{\partial \mathbf{h}(n)}{\partial h(n)} \end{aligned} \tag{4}$$

For complex value of $\mathbf{h}(n)$, we can write $\mathbf{h}(n) = \mathbf{h}_r(n) + j\mathbf{h}_i(n)$. Therefore, we get

$$\frac{\partial \mathbf{h}(n)}{\partial \mathbf{h}(n)} = \frac{\partial \mathbf{h}(n)}{\partial \mathbf{h}_r(n)} + j\frac{\partial \mathbf{h}(n)}{\partial \mathbf{h}_i(n)} = 1 + j.j = 1 - 1 = 0 \tag{5}$$

$$\frac{\partial \mathbf{h}^*(n)}{\partial \mathbf{h}(n)} = \frac{\partial \mathbf{h}^*(n)}{\partial \mathbf{h}_r(n)} + j\frac{\partial \mathbf{h}^*(n)}{\partial \mathbf{h}_i(n)} = 1 - j.j = 1 + 1 = 2 \tag{6}$$

Eqs. (5) and (6) in Eq. (4) yield

$$\nabla \mathbf{J}(n) = -2e(n)\mathbf{u}^*(n) \tag{7}$$

Putting this gradient vector in Eq. (1), we get the LMS update equation as

$$\mathbf{h}(n+1) = \mathbf{h}(n) + 2\mu' e(n)\mathbf{u}^*(n) \tag{8}$$

Introducing a constant *2* into a new step size parameter μ yield the update equation of LMS as

$$\mathbf{h}(n+1) = \mathbf{h}(n) + \mu e(n)\mathbf{u}^*(n) \tag{9}$$

A2. Update equation for the CMA

The error value for the CMA can be written as

$$e(n) = R_2^2 - |v(n)|^2 \tag{10}$$

According to this definition, $e(n)$ is real, thus $e(n)=e^*(n)$

Therefore, the gradient vector is

$$\begin{aligned}
\nabla \mathbf{J}(n) &= e(n)\frac{\partial}{\partial \mathbf{h}(n)}\{e^*(n)\} + e^*(n)\frac{\partial}{\partial \mathbf{h}(n)}\{e(n)\} \\
&= 2e(n)\frac{\partial}{\partial \mathbf{h}(n)}\{e(n)\} \\
&= 2e(n)\frac{\partial}{\partial \mathbf{h}(n)}\{R_2^2 - v(n)v^*(n)\} \\
&= -2e(n)\left[v(n)\frac{\partial}{\partial \mathbf{h}(n)}\{v^*(n)\} + v^*(n)\frac{\partial}{\partial \mathbf{h}(n)}\{v(n)\} \right] \\
&= -2e(n)\left[v(n)\frac{\partial}{\partial \mathbf{h}(n)}\{\mathbf{h}^*(n)\mathbf{u}^*(n)\} + v^*(n)\frac{\partial}{\partial \mathbf{h}(n)}\{\mathbf{h}(n)\mathbf{u}(n)\} \right] \\
&= -2e(n)\left[v(n)\mathbf{u}^*(n)\frac{\partial \mathbf{h}^*(n)}{\partial \mathbf{h}(n)} + v^*(n)\mathbf{u}(n)\frac{\partial \mathbf{h}(n)}{\partial \mathbf{h}(n)} \right] \\
&= -4e(n)v(n)\mathbf{u}^*(n)
\end{aligned} \tag{11}$$

Hence, the update equation of CMA can be written as

$$\mathbf{h}(n+1) = \mathbf{h}(n) + 4\mu' e(n) v(n) \mathbf{u}^*(n) \tag{12}$$

Introducing a constant *4* into a new step size parameter μ yield the update equation of CMA as

$$\mathbf{h}(n+1) = \mathbf{h}(n) + \mu e(n) v(n) \mathbf{u}^*(n) \tag{14}$$